Spectral photoluminescence for the characterization of excitation states in semiconductors and fluorescence solar collectors with manipulation of the in and out coupling of radiation

Spektrale Photolumineszenz zur Charakterisierung von Anregungszuständen in Halbleitern und Fluoreszenzsolarkollektoren mit Manipulation der Strahlungsein- und auskopplung

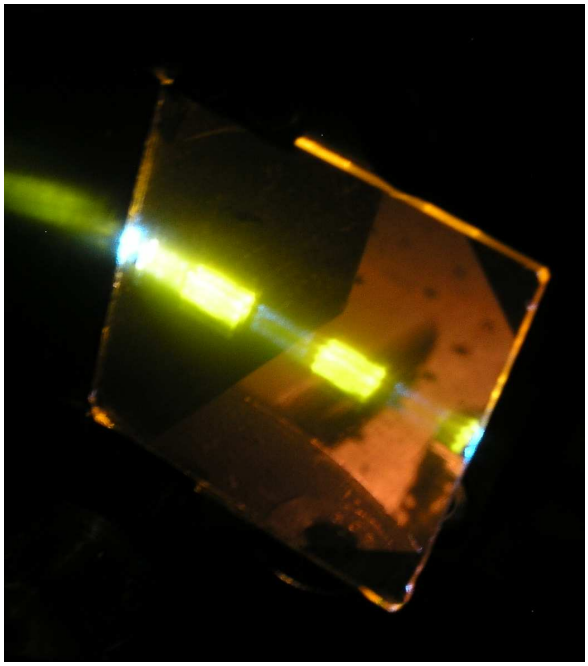

Von der Fakultät für Mathematik und Naturwissenschaften

der Carl von Ossietzky Universität Oldenburg

zur Erlangung des Grades und Titels eines

Doktors der Naturwissenschaften (Dr. rer. nat.)

angenommene Dissertation

von

Sebastian Knabe

geboren am 06.06.1983 in Oldenburg (Oldenburg)

Gutachter: Prof. Dr. G.H. Bauer

Zweitgutachter: Prof. Dr. T. Markvart

Tag der Disputation: 20.05.2011

Contents

1. Motivation and Introduction **1**

1.1. Efficiency limits of solar cells . . . 2
1.2. Light trapping . . . 2
1.3. Fluorescence solar collector . . . 5

2. Theoretical background **7**

2.1. The source of radiation . . . 7
2.1.1. Information from PL spectra . . . 8
2.1.1.1. Temperature T . . . 8
2.1.1.2. Splitting of quasi-Fermi levels μ . . . 9
2.1.1.3. Absorption $A(E_{Ph})$ . . . 10
2.2. Propagation of electro-magnetic radiation . . . 10
2.2.1. Propagation through a sample . . . 11
2.2.1.1. Transmission . . . 11
2.2.1.2. Reflection . . . 12
2.2.1.3. Results . . . 13
2.2.2. From inside a sample to the top or bottom surface . . . 14
2.2.2.1. Comparison with propagation through a sample . . . 16
2.2.2.2. Angular dependent emission from top . . . 19
2.2.3. From inside a sample to the edge . . . 20
2.2.3.1. Fluco with dye on top . . . 21
2.2.3.2. Fluco with homogeneous dye concentration . . . 25
2.3. Excess carrier density . . . 27
2.3.1. Analytical solution of the continuity equation . . . 28
2.3.1.1. Results of the PL for the analytical solution . . . 28
2.3.2. Numerical solution of the continuity equation for $\tau(x)$ . . . 29
2.3.2.1. Results of the PL with $\tau(x)$ in the excess carrier concentration . . . 31
2.3.3. Numerical solution of the continuity equation with $\tau(x)$ and $\alpha(x, E_{Ph})$ . . . 32
2.3.3.1. Results of the PL for $\tau(x)$ and $\alpha(x, E)$ . . . 34

3. Experimental setups and samples **39**

3.1. Angular dependent PL . . . 39
3.1.1. Calibration . . . 41
3.2. Scattering . . . 41

3.3. Fluco edge emission . . . 41
3.4. Additional Setups . . . 42
3.4.1. Reflection and Transmission . . . 42
3.4.2. AFM . . . 42
3.4.3. Laterally resolved PL . . . 43
3.4.3.1. Makro-PL . . . 43
3.4.3.2. Micro-PL . . . 43
3.4.3.3. SNOM . . . 43
3.5. Samples . . . 44
3.5.1. Crystalline silicon . . . 44
3.5.2. Fluorescence solar collector . . . 44
3.5.3. Photonic structures . . . 44
3.5.3.1. Bragg-mirror . . . 45
3.5.3.2. Opal . . . 46
3.6. Refractive Index matching . . . 49

4. Experimental results and their interpretation 55
4.1. Characterization of the opal . . . 55
4.1.1. Transmission . . . 55
4.1.2. Reflection . . . 56
4.1.3. Absorption . . . 58
4.1.4. Scattering . . . 59
4.1.4.1. Simulation of Mie scattering . . . 60
4.1.5. Homogeneity . . . 60
4.1.5.1. On a µm-scale . . . 60
4.1.5.2. On a mm-scale . . . 64
4.2. Characterization of crystalline silicon . . . 65
4.2.1. Absorption . . . 65
4.2.2. Angular dependent excitation . . . 67
4.2.3. Angular dependent emission from top . . . 68
4.2.3.1. Calibrated PL from the top of the absorber . . . 71
4.2.4. Homogeneity . . . 72
4.2.5. Edge emission . . . 74
4.3. Characterization of the fluco . . . 75
4.3.1. Absorption . . . 75
4.3.2. Emission . . . 76
4.3.3. Angular dependent edge emission . . . 77
4.3.4. Angular dependent emission from top . . . 79
4.3.5. Angular dependent excitation . . . 82
4.3.6. Homogeneity . . . 82

4.4. Light trapping . . . 83
4.4.1. In c-Si . . . 85
4.4.1.1. Absorption enhancement . . . 87
4.4.1.2. Effect of an opal on emission from the top . . . 88
4.4.1.3. Effect on the excitation . . . 90
4.4.2. In a fluco . . . 91
4.4.2.1. Effect on emission from the top . . . 91
4.4.2.2. Effect on the edge emission . . . 93
4.4.2.3. Effect on excitation . . . 93

5. Summary, conclusion and outlook **95**

6. Zusammenfassung **99**

7. References **100**

A. Symbols **111**

B. Calibration of the experimental setups **113**

C. Estimation of the excess carrier concentration from the PL yield **115**
C.1. Idea . . . 115
C.2. Uniqueness of the different parameters . . . 117
C.3. Application to simulated spectra . . . 119
C.4. Application to measured spectra . . . 120
C.4.1. Different cost functions . . . 123
C.4.2. Possible problems of the estimation of n from the PL yield . . . 123
C.5. Summary and conclusion . . . 126

D. A detailed presentation of the edge emission of a fluco **129**

E. Filter and fluco edge emission - angular dependences **133**

F. Effect of a photonic structure on the edge emission of a fluco **137**

G. Acknowledgements **143**

H. Curriculum vitae **145**

I. Erklärung **147**

List of Figures

1.1. AM1 solar radiation for normal incidence from [7] with illustration of the photon energies below the band-gap of a c-Si absorber and photon energies, for which the photons are absorbed by the glass or near the surface of the absorber as well as an illustration of frequency up and down conversion of photons. 3
1.2. Reduction of the reemission with a photonic structure on top of the absorber and a back reflector below. The emitted light with an angle of incidence above the critical angle of the photonic structure is trapped inside the absorber. 4
1.3. Transmission through an idealized photonic structure for light trapping. The transmission for a small angle of incidence is perfect (100%) and zero for other angles. 4
1.4. Concept for the application of an angular selective filter on top of absorber materials. The part of the incident light which hits the back of the absorber is scattered back by a Lambertian scatterer. The radiation hitting the front of the solar cell is either reflected back or leaves it or all radiation with an angle of incidence above the critical angle of the angular selective filter is reflected back. 5
1.5. 2d sketch of a fluorescence solar collector (fluco) with excitation, emission, escape cone and a reflector on one edge of the fluco and a solar cell on the other. 6

2.1. PL spectrum for the emission from excited c-Si with demonstration of the influence of absorption and splitting of quasi-Fermi levels (Phonon bands in 0.9 eV - 1.1 eV in absorption coefficient). This spectrum was simulated with the model from chapter 2.2.2. 8
2.2. Model for the simulations with three layers (substrate, absorber, air) of different refractive indices n_i. The detector is assumed to be within the air. 11
2.3. Different cases for the propagation of radiation. Through an absorber, from inside an absorber to its top and from inside an absorber to its edge. 11
2.4. Transmission through and reflection on a sample in the three layer simulation with light source S and propagation of radiation. 13
2.5. Comparison of absorption $A = 1 - T - R$, reflection R and transmission T for $d = 20$ µm thick c-Si. 14
2.6. Model for the calculation of the emission from inside an absorber to the top or bottom surface. 16

2.7. Comparison of the simulation for the PL emission through the top or bottom of the absorber with the analytical result from Würfel [39] for a $d = 20$ µm thick c-Si absorber. 17

2.8. Comparison of the transmission from a source inside a sample and the transmission through a sample for the full absorber and transmission only from one emission position. 18

2.9. Emission from inside an absorber to one surface for different positions of the emission source inside the absorber vs. the transmission through the whole absorber, depth dependence of the transmission maximum around $E_{Ph} = 0.87$ eV and results of the comparison of maxima vs. absorber position ($d = 20$ µm thick c-Si wafer). 18

2.10. Definition of α and β. 20

2.11. Simulated angular dependence of the emission on the top or bottom of an excited $d = 10$ µm thin c-Si absorber and spectral difference between various emission angles for both polarizations. 21

2.12. Angle of incidence (α) vs. angle of the diffracted radiation (β) given by Snell's law for the refraction of radiation on a phase border between a refractive index of $n_1 = 1.5$ and $n_2 = 1$. 23

2.13. Sketch for the numerical calculation of the edge emission for a fluco with the dye on top. Model for the simulation with excitation at a distance x from the edge of the fluco, emission angle α, emission from the edge at a distance h from the top of the fluco under the angle β. Emission with one reflection on the back surface with an emission angle of $-\beta$ and $-\beta'$ and emission with one reflection on the back surface and one reflection on the top surface of the fluco and with emission angle β at the edge of the fluco. 23

2.14. Simulated angularly resolved emission of the fluorescence at the edge of a fluco for different excitation positions (distance to the edge x) on the fluco and angular dependent emission at the edge for an excitation at x=10 mm from the edge. . . 24

2.15. Illustration of the case-by-case analysis for the emission at the edge of a fluco with homogeneous dye concentration. 26

2.16. Simulated angular dependent edge emission for different excitation positions on the top of the fluco and edge emission for homogeneous excitation for a fluco with homogeneous dye concentration and homogeneous emission in the depth. 26

2.17. Simulated angular dependent edge emission for different excitation positions on the top of the fluco and edge emission for homogeneous excitation for a fluco with homogeneous dye concentration and exponentially reduced emission in the depth. 27

2.18. Different excess carrier concentrations for different recombination velocities on the top of the absorber and the resulting PL-yields. 30

2.19. Comparison of the splitting of quasi-Fermi levels calculated from the maximum excess carrier concentration and from the excess carrier concentration on the top of the absorber compared to the splitting of quasi-Fermi levels estimated from the PL yield for high photon energies. 30
2.20. Change of the excess carrier lifetime by defects in the top of the absorber with reduction of the lifetime τ_f, defect diffusion depth x_0 and decay area for the reduction of the lifetime from t_0 to $\tau_0 - \tau_f$. 31
2.21. Various excess carrier lifetimes for different reduced lifetimes at the top of the absorber τ_f, resulting excess carrier concentrations and resulting normalized PL yields. 32
2.22. Comparison of the numerically generated and integrated PL yield and the PL yield at $E_{Ph} = 1.4$ eV vs. the splitting of quasi-Fermi levels calculated from the excess carrier density at the top of the absorber. 33
2.23. Idealized effect of a variation in the band-gap (ΔE_G) on the absorption coefficient and linear variation of the band-gap over the absorber depth characterized in this work. 34
2.24. PL photon flux for a constant excess carrier concentration ($n(x) = 1 \cdot 10^{12}$ /cm^3) with the different absorptions given by the band-gap variation in Fig. 2.23 and illustration of the PL yield at $E_{Ph} = 1.05$ eV over the band-gap variation at $x = 0.75d$. 36
2.25. Excess carrier concentration for the absorption coefficients given by the band-gaps in Fig. 2.23 and the resulting PL yields. 37
2.26. Influence of the integrated PL yield and the PL yield for $E_{Ph} = 1.4$ eV on the quasi-Fermi level splitting calculated from the excess carrier concentration. No quasi-linear behavior can be observed anymore. 37

3.1. Sketch of the experimental setup for PL measurements with angular dependent detection (lower rotation stage) and/or angular dependent excitation (upper rotation stage) for different absorber materials like c-Si or flucos. This setup also provides a rotation stage for the rotation of the sample around the axis of excitation. The excitation is done with a 488 nm laser and filtered by a bandpass filter and polarization filter. The emitted radiation from the absorber is collected by a collimator and coupled into an optical multichannel analyzer by a glass fiber. . . 40
3.2. Illustration of how the axis of rotation should always be on the top of the absorber/emitter, sketch of the sample holder for the detection of the edge emission with mount and shield to depress the top emission and sample holder for the detection of the top/bottom emission. 40
3.3. Experimental setup to measure the scattering from a sample mounted in S in reflection or transmission with sample holder S, neutral density filter NDF, photo diode PD, frequency controller F and chopper CP, lock-in-amplifier L, motor M and a computer PC. 41

3.4. Sketch of the setup to measure the edge emission of a fluco with a photo diode. . 42
3.5. Different realizations of flucos. Glass substrate with fluorescence dye in PMMA on top, a full PMMA fluco with homogeneous dye concentration and a cuvette with a solution containing a fluorescence dye. 44
3.6. Sketch of a 1d, 2d and 3d photonic crystal. 45
3.7. Sketch of a Bragg-mirror with a stack of materials with refractive indices n_1 and n_2 and thicknesses d_1 and d_2 as well as simulation of the reflection on such a Bragg-mirror. 46
3.8. Photonic band structure (calculated with mpb [68]) of an opal for different crystal orientations and an illustration of these crystal orientations of the first Brillouin zone. Provided by Andreas Billawny at MLU Halle. 49
3.9. Surface of an idealized opal in $\Gamma - \mathrm{L}$ direction. 50
3.10. Refractive index for the simulation of the transmission from crystalline silicon into air with and without additional photonic crystal layer on top of the silicon. . . . 50
3.11. Transmission from silicon to air for s- and p-polarized electro-magnetic radiation without additional layer on top of the silicon. 50
3.12. Transmission from silicon to air for s- and p-polarized electro-magnetic radiation with additional layer of refractive index $n = 1.37$ and $d = 3.7$ µm thickness on top of the silicon. 51
3.13. Transmission from air to c-Si in comparison to the transmission from air through a $d = 3.7$ µm thick layer with refractive index $n = 1.37$ for s-polarized radiation. 51
3.14. Simulated transmission through an opal with different numbers of layers of $D =$ 540 nm PMMA spheres. 51
3.15. Reflexion on and transmission through an opal with ten layers of $D = 540$ nm PMMA spheres for different tilting angles. 52
3.16. Reflexion on and transmission through an opal with ten layers of $D = 540$ nm PMMA spheres for a tilting angle of 30° and a rotation of the sample around the axis of excitation. 52
3.17. Transmission in $\Gamma - \mathrm{L}$ direction through a ten layer opal of $D = 540$ nm PMMA nanospheres calculated with a FDTD algorithm. 52
3.18. Angularly resolved transmission in $\Gamma - \mathrm{X}$ direction through a ten layer opal of $D = 540$ nm PMMA nanospheres. Provided by J. Üpping from MLU Halle. . . . 53
3.19. Sketch of the measurements of the transmission through an refractive index matching medium between two glass substrates. 54
3.20. Experimental results of the transmission through two glass substrates with different index matching media between them as sketched in Fig. 3.19. 54

4.1. Angular dependent and spectrally resolved transmission through an opal layer on a glass substrate with $\lambda_{\mathrm{stop}} = 580$ nm and $\lambda_{\mathrm{stop}} = 1200$ nm stopgap. 56

4.2. Comparison of the transmission through the opals with $\lambda_{stop} = 580$ nm and $\lambda_{stop} = 1200$ nm stopgap with the transmission through the substrate. The reduction of the transmission due to scattering is reduced with increasing wavelength (Mie scattering). 57
4.3. Angular dependent and spectrally resolved reflection at an opal with $\lambda_{stop} = 580$ nm stopgap on a glass substrate and wavelength of the reflection peaks vs. reflection angle in comparison with the theory. 58
4.4. Definition of the reflection angles for Bragg's law (θ) and the angle of incidence φ in the experimental setup. 58
4.5. Absorption of an opal with a stopgap at $\lambda_{stop} = 1200$ nm on a glass substrate. The absorption is calculated from the transmission and reflection, and the absorption of the bare substrate has been subtracted. 59
4.6. Photon flux scattered by the opal on glass in comparison with the scattering on pure glass for 1112 nm and 632.8 nm, and transmission T from Fig. 4.1 (right) in logarithmic representation. 60
4.7. Simulated differential scattering by a sphere with $n = 1.5$ for different sphere diameters , wavelengths and angles. 61
4.8. Latterly resolved direct reflection on a 1200 nm stopgap opal on glass substrate with spectrally integrated reflection for wavelengths in the stopgap (a), outside the stopgap (b), all wavelengths (c) and (d) the ratio of (a) to (b). 62
4.9. Latterly resolved direct transmission on a 1200 nm stopgap opal on glass substrate with spectrally integrated reflection for wavelengths in the stopgap (a), outside the stopgap (b), all wavelengths (c) and (d) the ratio of (a) to (b). 63
4.10. AFM image of the 1200 nm stopgap opal. One can clearly see homogeneous parts of the opal divided by drying disruptions of the wet opal after the coting. 64
4.11. Laterally resolved and spectrally integrated reflection of a white light source on an opal with $\lambda_{stop} = 1200$ nm stopgap on a glass substrate. Integration of the wavelengths inside and outside the stopgap. 66
4.12. Microscope image of an opal with $\lambda_{stop} = 1200$ nm stopgap, 20x magnified, illustration of the patches and histogram of the patch size of homogeneous opal regimes. 66
4.13. Artificial surface of an opal with $D = 540$ nm spheres with a diameter of 40 µm and 2d Fourier transform of the surface for the rectangular sample and a round sample with a radius of $r = 5$ µm and $r = 20$ µm. 67
4.14. Absorption coefficient $\alpha(E_{Ph})$ of c-Si from [82] with an indirect band-gap at $E_{Ph} = 1.12eV$ at $T = 300$ K. 68
4.15. Angular dependent and spectrally resolved emitted PL yield from c-Si for different excitation angles and comparison of the angular dependency with a theoretical model. 69
4.16. Sketch of the increased excited absorber area when the excitation angle is varied from $\gamma = 0°$ to $\gamma = 45°$ for a laser beam with diameter d. 69

4.17. Illustration of the measurement of the angular dependent PL emission of excited c-Si with excitation on one side and detection on the opposite side. 71
4.18. Angular dependent and spectrally resolved PL yield from an excited c-Si wafer and comparison of the angular dependence with the simulation. 71
4.19. Sketch of a better way to mount the sample, so that the surface of the emission side of the sample is directly on the axis of rotation. 72
4.20. Absolute PL yield from an excited c-Si wafer. 72
4.21. Image of the laterally resolved and spectrally integrated PL yield from an excited c-Si wafer. 73
4.22. Illustration of the experimental setup for the comparison of the PL emission from a c-Si wafer with glass substrate and a c-Si wafer with photonic crystal on a glass substrate. 74
4.23. Lateral excess carrier concentration for the simulation of the edge emission, measured PL from top and edge and simulated PL for a c-Si wafer. 75
4.24. Direct reflection and transmission results for flucos with Cumarin 540A and Rhodamin 6 G. 76
4.25. Absorption calculated from the reflection and transmission in Fig. 4.24. 77
4.26. PL emission from and absorption of an excited fluco with Rhodamin 6 G in PMMA on the surface of a glass substrate and a fluco with Lumogen F rot 305 in PMMA. 78
4.27. Spectrally integrated angular dependent edge emission of a fluco doped with Rhodamin 6 G in PMMA on glass in dependence of the distance between edge and excitation spot in comparison with the simulation results from chapter 2.2.3 and sketch of the experiment. 79
4.28. Angular dependent and spectrally integrated PL yield for various distances of the excitation from the emission edge for the Lumogen F rot 305 fluco with a dye concentration of 0.8 g/l and 0.3 g/l. 80
4.29. Angular dependence of the spectrally integrated PL yield for a spot excitation of the Lumogen F rot fluco with 0.8 g/l and 0.3 g/l dye concentration. 80
4.30. Angular dependent and spectrally integrated top emission of an excited Lumogen F rot 305 fluco, the angular dependence in comparison to the angular dependence of c-Si, the simulation for c-Si as well as a simple simulation for the fluco. 81
4.31. Normalized angular dependence of the spectrally integrated PL yield for different excitation angles and detection under normal incidence for a fluco with Rhodamin 6 G and c-Si. A fluco can absorb diffuse radiation better than e. g. c-Si. 82
4.32. Image of the laterally resolved (mm-scale) and spectrally integrated PL yield of a fluco with Rhodamin 6 G and histogram of the spectrally integrated photon flux. 84
4.33. AFM image and SNOM in transmission for the fluco with Rhodamin 6 G in PMMA on glass. 84
4.34. AFM image and SNOM in emission mode for a small area of the fluco in Fig. 4.33 for a fluco with Rhodamin 6 G in PMMA on glass. 85

4.35. Spectral transmission through a Bragg-mirror and illustration of the application of a Bragg-mirror to reduce the PL emission. 86

4.36. Emission from the top of an excited c-Si wafer with and without Bragg-mirror on top. Comparison of experiment and simulation. 87

4.37. Enhancement of the absorption in crystalline silicon with an opal on glass substrate with a stopgap at $\lambda_{\mathrm{stop}} = 1200$ nm and calculated EQE for a c-Si solar cell with the absorption coefficient from the left. 88

4.38. Sketch of the measurement for the characterization of the influence of an opal on the top emission. 89

4.39. Angular and spectrally resolved top emission from c-Si with glass on top and from c-Si with glass and $\lambda_{\mathrm{stop}} = 1200$ nm stopgap opal on top. 89

4.40. Ratio $\chi(\alpha, \lambda)$ of emission with glass substrate and opal to PL emission with only a glass substrate from experiment and theory. 90

4.41. Sketch of the measurement of the angular dependent excitation and ratio of the PL emission from c-Si with opal in the excitation through the one without opal between excitation source and sample. 91

4.42. Angular and spectrally dependent top emission from a fluco (Rhodamin 6 G) with glass and from the fluco with glass and $\lambda_{\mathrm{stop}} = 580$ nm stopgap opal on top. . . . 92

4.43. Ratio of the PL emission with photonic structure to that without photonic structure for the opal and a Bragg-mirror with 550 nm edge. 93

4.44. Effect of the photonic structure on the excitation of a fluco for a 580 nm stopgap opal and for a 550 nm low-pass filter. 94

5.1. Schematic design of a multi-spectral fluco system with opals. Flucos with dyes for different absorption wavelengths are stacked with opals with a stopgap according to the fluco between them. In this way the radiation scattered by a fluco is still inside another fluco. The flucos guide the trapped radiation to an attached solar cell with corresponding band-gap. 97

6.1. Mögliches Design eines multispektralen Fluoreszenzkollektorsystems mit Opalen. Fluoreszenzkollektoren mit Farbstoffen für verschiedene Absorptionswellenlängen werden mit passenden Opalen dazwischen übereinander gestapelt. Auf diese Weise wird die Strahlung, die von dem Opal gestreut wird, von einem Fluoreszenzkollektor absorbiert. Die Fluoreszenzkollektoren leiten die eingesperrte Strahlung zu einer Solarzelle an der Kante, welche eine passende Bandlücke besitzt. 101

C.1. Idea for the calculation of the excess carrier concentration from the PL yield: Comparison of the emitted PL for the excitation from side of the detector (left) named excitation from right or in reflection and for the excitation from the other side of the absorber (right) named excitation from left or in transmission. 116

C.2. Excess carrier concentration for the excitation of an absorber from the left side and the right side (left) as well as the emitted PL yield for the PL emission on the side of the detector (right). 117

C.3. Idea for the algorithm, which calculates the excess carrier concentration from the PL. 118

C.4. Deviations $dev_{1,2}$ for the variation of S_0 (left) and D (right) while the other parameters are fixed. 119

C.5. Simulated as well as reconstructed excess carrier concentration (left) and simulated as well as reconstructed PL yield (right). 121

C.6. Experimental results of the emitted PL from an excited c-Si for the excitation and detection from one side and from different sides (left) and result of the estimation of the excess carrier concentration (right) with the Nelder Mead Algorithm. . . . 122

C.7. PL spectra for the emission of excited c-Si for measurements in reflection and transmission each. 124

C.8. Results of PL measurements in transmission and reflection. The error bars result from the averaging of the measurements on the same spot of the sample and the same excitation. 126

D.1. Spectral edge emission for an emission angle of 40° for different distances between excitation and emission edge for the fluco with 0.3 g/l (left) and 0.8 g/l (right) Lumogen F rot 305. 130

D.2. Spectral emission at the edge for different emission angles for excitation ca. 1 mm from the emission edge (left), in the center of the fluco (center) and ca. 24 mm from the emission edge (right). 130

D.3. Wavelength at which the PL yield reaches 50% of the maximum PL yield ($0.5\Gamma_{max}$) vs. the distance between between excitation and emission edge for the fluco with 0.3 g/l (left) and 0.8 g/l (right) Lumogen F rot 305. 131

E.1. Ratio of the angular and spectrally resolved edge emission with back reflector and without back reflector for a fluco with 0.8 g/l Lumogen F rot. 134

E.2. Ratio of the angular and spectrally resolved edge emission with spacer between fluco and filter and without them with back reflector (left) and without (right) for a fluco with 0.8 g/l Lumogen F rot. 134

E.3. Ratio of the angular and spectrally resolved edge emission with filter and without filter with back reflector and the filter on top of the fluco (left) and with the filter on spacer on top of the fluco (right) for a fluco with 0.8 g/l Lumogen F rot. . . . 135

F.1. Position of the filter for the different setups: Emission of the fluco without filter, with a filter on top of the fluco and with the filter on the fluco with spacers in between. 139

F.2. Influence of a back reflector and a filter on top of the fluco or on top of spacers on the edge emission for a fluco with Rhodamin 6 G on top of a glass substrate and Lumogen F rot 305 in PMMA. 140
F.3. Transmission through the 550 nm low-pass filter. 140
F.4. Diffuse reflection of the back reflector based on bleached cellulose and angular dependent scattering of a 632.8 nm laser on the back reflector in comparison to the reflection on a mirror. 141
F.5. Simulation of the influence of a filter and mirrors on the edge emission of a fluco. Simulation model with fluco, low-pass filter on top and mirrors on three sides of the fluco and on its back, impact on the edge emission for low and high dye concentration. 141
F.6. Influence of the 550 nm low-pass filter on the angular dependent edge emission for homogeneous excitation of the fluco with Rhodamin 6 G in PMMA on glass. . . . 142

List of Tables

2.1. Photon energies for the maxima in Fig. 2.9 (right). 19
2.2. Case-by-case analysis for the parameter h and the respective sign of the emission angle at the fluco edge for a fluco with dye on top of a substrate and homogeneous dye concentration. 24

3.1. Properties of the c-Si wafer. 44
3.2. Parameter for the simulation of the Bragg-mirror. 46

4.1. Results of the analysis of the c-Si PL yield in Fig. 4.20 (left). 73

A.1. Symbols used in this work - I. 111
A.2. Symbols used in this work - II. 112

C.1. Parameters of the excess carrier concentration used in the simulations. 119
C.2. Overview over the influence of a too low or high parameter of the excess carrier concentration on $dev_{1,2}$ with sign (s($dev_{1,2}$)), which deviation is higher ($b(dev_i)$) and some additional informations. Here E_{in} donates the photon energy of the excitation. 120
C.3. Parameter of the excess carrier concentration: Simulated, reconstructed Nelder Mead and reconstructed generic algorithm. 120
C.4. Results of the excess carrier concentration in excited c-Si from Nelder Mead algorithm and generic algorithm. 122
C.5. Results of the excess carrier concentration in excited c-Si from the Generic algorithm for different cost functions. 124

1. Motivation and Introduction

One of the goals in research and development of solar cells is the reduction of the price per Wp (watt-peak) by reducing the production costs or by increasing the solar cell efficiency with different approaches. Some of the approaches to enhance the efficiency involve methods which influence the absorption, emission and propagation of electro-magnetic radiation inside the solar cell, e. g. enhancing the absorption with nanoparticles [1][1], by light trapping with photonic structures [3] or by scattering inside the absorber [4], energy up conversion to utilize the photons with photon energy below the band-gap of the absorber [5] or enhancing the efficiency for high photon energies by energy down conversion [6].

The aim of this thesis is to investigate different experimental methods to characterize the optical properties of different materials which influence the absorption, emission and propagation in semiconductor absorbers as well as to characterize the impact of these materials on the propagation of radiation inside the absorber. The characterized materials will be limited to photonic structures which provide the possibility to trap the electro-magnetic radiation inside an absorber and to fluorescence solar collectors[2] (flucos) as an exemplary approach to reduce the production costs of solar cells. Flucos are also a very interesting means to study the propagation of radiation inside an absorber.

In a first step the propagation of photoluminescence (PL) radiation inside an absorber will be introduced: For that reason the source of PL radiation is presented and the propagation of electro-magnetic radiation through a sample and from the inside of an absorber to its top surface and edge are explained. Since PL radiation inside a semiconductor absorber is strongly governed by the excess carrier concentration, the influence of the excess carrier concentration on the spectral shape of the emitted PL radiation will be discussed.

In a second step the experimental setups and samples used in this work will be introduced. This includes the discussion of the theory of the photonic structures used in this work as well as an introduction on absorbers and photonic structures in general. The samples are: Crystalline silicon (c-Si), one of the most used absorber material in solar cells, different types of flucos and two types of photonic structures, a one dimensional (Bragg-mirror) photonic structure and a three dimensional (opal) one.

Finally, results for the experiments with the photonic structure of the opal (the Bragg-mirror is rather uninteresting), the c-Si absorber, the fluco and especially the effect of photonic structures on the emission from a c-Si absorber and a fluco will be presented.

[1] This reference as well as the following references are from project partners of the project Nanovolt [2] but there is literature from others available.

[2] Also named fluorescence (solar) concentrator.

In this work the focus will be on the possible characterization procedure, the interpretation of the results and on the design of theoretical models. This work will not provide different efficiencies of the methods described above. The materials used in these thesis are not optimized for high efficiencies but for simplicity, thus a complete possible design of a next generation solar cell will not be given.

1.1. Efficiency limits of solar cells

First of all, the following question will be discussed: "Why is the efficiency of a solar cell limited and what are the limits?".
Solar radiation (e. g. the AM1[3] solar spectrum from [7] in Fig. 1.1) can be divided into three parts concerning the usability of the photons in a single junction solar cell with one band-gap: If the photon energy is below the band-gap, the photons of the solar radiation just propagate through the absorber of the solar cell and are not absorbed and thus not utilized. For a photon energy above the band-gap, it is assumed that all photons inside the semiconductor are absorbed, but the energy of the photons above the band-gap of the absorber is mainly lost due to thermalization and thus also lost. For photons with very high photon energy, the absorption in a semiconductor is so high, that the photons are either absorbed near the surface of the absorber or even in the glass substrate.
Beside these losses, all absorbers are also emitters [8], thus some energy is lost from the solar cell due to emission of radiation. An additional effect of loss is the reflection at the incident side of the radiation, due to the rather high refractive index of the absorber (e. g. $n = 3.5$ for c-Si [9] means a reflection of ca. 30% of the incident radiation) and reflection on the glass at the top of the solar cell, a part of the incident light is just reflected back and also not utilized by the solar cell.
Depending on the model for the processes involved in the solar cell, there are different calculations of the theoretical limits of a single junction solar cell like 31% from Shockley and Queisser[4] [10] or 28% from Kerr [11].
These limits can be broken by either stacking solar cells with different band-gaps (tandem cells or triple junction cells [12]) or by light trapping which will be described in the next section.

1.2. Light trapping

As mentioned before, the emphasis of this work lies on the characterization of different materials and not on a design study of a solar cell, thus only an idea why light trapping is a possible method to increase the solar cell efficiency will be given and not a full overview of the theoretical background of light trapping in solar cells, as there is much literature available, e. g. [3, 13–19].
A model for light trapping can be seen in Fig. 1.2. The acceptance angle for a tracked solar

[3] Airmass 1: Solar radiation after the transmission through the earth's atmosphere.
[4] Without reflection losses.

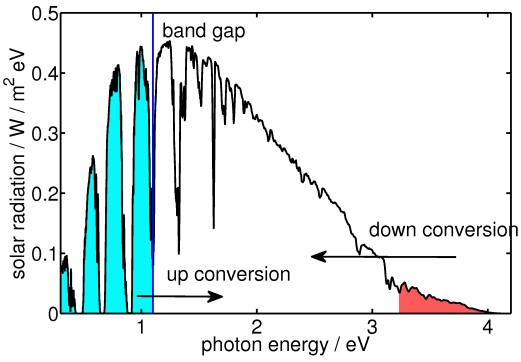

Figure 1.1.: AM1 solar radiation for normal incidence from [7] with illustration of the photon energies below the band-gap (blue) of a c-Si absorber and photon energies, for which the photons are absorbed by the glass or near the surface of the absorber (red) as well as an illustration of frequency up and down conversion of photons.

cell is given by the distance from earth to sun ($d = 1.50 \cdot 10^{13}$ cm) and the radius of the sun ($r = 6.96 \cdot 10^{10}$ cm) (both values are from [20]) and is approximately $\alpha_{\text{sun}} = 0.27°$. So the incident solar radiation arrives at a very small solid angle. Without a photonic structure this radiation (apart from absorption) hits the back of the absorber and is there scattered back e. g. by texturising the back of the solar cell [21–23] and applying a back reflector[5]. That scattered radiation propagates back through the absorber to its top, where the radiation can leave the absorber (depending on angle of incidence).

Reducing the acceptance angle of the solar cell to around 0.5° with an angular selective filter like a filter with the transmission plotted in Fig. 1.3 which reflects all light with an angle of incidence above 0.5°, does not influence the incident solar radiation if the solar cell tracks[6] the sun, but traps the scattered radiation inside the absorber (apart from the radiation with an angle of incidence below 0.5°). This is illustrated in Fig. 1.4 (right). This light trapping enhances the propagation length of radiation inside an absorber, thus the absorption of light, especially for photons which have a low probability to be absorbed (e. g. with photon energy below the band-gap), is increased.

Such an angular selective filter is not only able to enhance the absorption but also to reduce the reemission as illustrated in Fig. 1.2. The absorbed light leads to PL emission inside the absorber which is emitted isotropically. A reduction of the emission angle by an angular selective filter prevents the emitted radiation from escaping the absorber and thus this radiation can be reabsorbed and is not lost.

[5]Such a design yields a solar cell with an efficiency above that of a solar cell with flat surfaces.
[6]A fixed solar cell requires an alternative filter design.

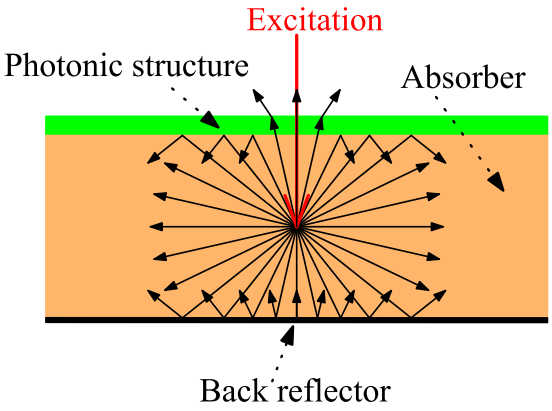

Figure 1.2.: Reduction of the reemission with a photonic structure on top of the absorber and a back reflector below. The emitted light with an angle of incidence above the critical angle of the photonic structure is trapped inside the absorber.

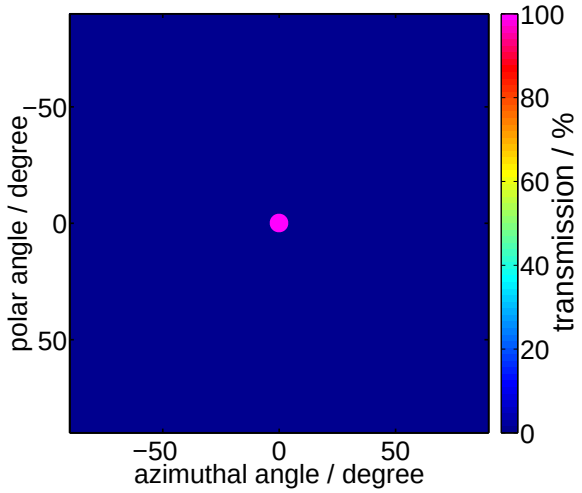

Figure 1.3.: Transmission through an idealized photonic structure for light trapping. The transmission for a small angle of incidence is perfect (100%) and zero for other angles.

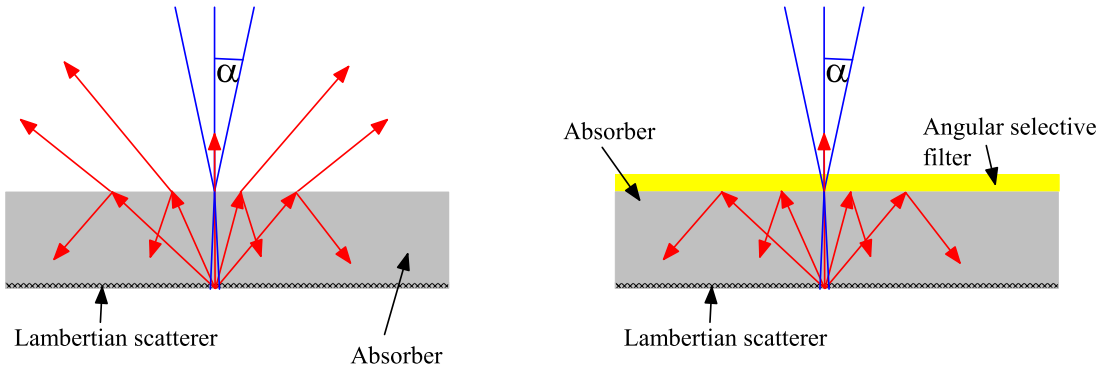

(a) Without angular selective filter.

(b) With angular selective filter.

Figure 1.4.: Concept for the application of an angular selective filter on top of absorber materials. The part of the incident light (blue) which hits the back of the absorber is scattered back (red) by a Lambertian scatterer. The radiation hitting the front of the solar cell is either reflected back or leaves it (a) or all radiation with an angle of incidence above the critical angle of the angular selective filter is reflected back (b).

1.3. Fluorescence solar collector

For the fluorescence solar collector (flucos) only the fundamental idea will be given, because the detailed theory of the fluco is not needed in this work and it can be found in the literature (e. g. in [24–26]).

A sketch of a fluco is plotted in Fig. 1.5: The incident light is absorbed (with an absorption efficiency η_{abs}) by a dye in or on a substrate like glass or PMMA with a refractive index of about $n_{\text{sub}} \approx 1.5$. This dye (fluorescence dye) reemitts the radiation with a lower photon energy (Stokes shift) directed isotropically into the substrate (with quantum efficiency of the dye η_{dye}) where some radiation is trapped due to total internal reflection, depending on the emission angle.

The radiation which can escape the fluco is inside the so called escape cone, given by the angle of total reflection

$$\theta_{\text{total}} = \arcsin\left(\frac{n_{\text{air}}}{n_{\text{sub}}}\right) = \arcsin\left(\frac{1}{1.5}\right) \approx 41.8^\circ \tag{1.1}$$

with the refractive index of air n_{air}.

This radiation is either reabsorbed on the way to the top of the fluco, emitted of the top or propagates to the edge. The radiation outside the escape cone travels to the edge of the fluco (including reabsorption) where the radiation either leaves the fluco to an attached solar cell or is reflected back by a mirror.

The idea of this design is to collect the solar radiation with a cheap fluco, guide the radiation to the edges where a small solar cell (small compared to the size of the fluco) is attached and thus to reduce the size of the expensive solar cells needed.

The fundamental principle of a fluco is quite simple, but due to the many processes involved, the efficiency of the fluco including the solar cell is so far rather small. Main loss processes are

reemission into the escape cone and reabsorption, which prohibit a commercial application of flucos.

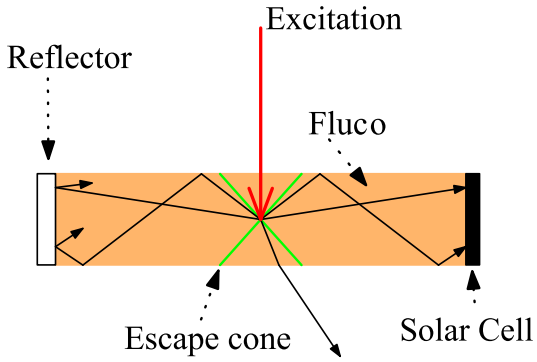

Figure 1.5.: 2d sketch of a fluorescence solar collector (fluco) with excitation (red), emission (black), escape cone (green) and a reflector on one edge of the fluco and a solar cell on the other.

2. Theoretical background

This chapter introduces the theoretical background that is needed to understand and interpret the experimental results in chapter 4. A detailed introduction of the theory of photonic crystals, flucos and solar cells will not be given here, because there is a lot of excellent literature available as mentioned before.
In the first part of the chapter, the radiation[1] emitted from excited absorber materials, the propagation of radiation for different cases and the calculation of the excess carrier density which governs the emission of photoluminescence (PL) photons in semiconductors will be given. The theoretical results for the propagation of radiation and the influence of different parameters of the excess carrier concentration on the emitted PL yield will also be presented.

2.1. The source of radiation

The photon energy (E_{Ph}) dependent radiation $\Gamma(E_{Ph})$ emitted from an excited absorber is given by Planck's generalized law [27]

$$\Gamma(E_{Ph}) = C\tilde{E}(E_{Ph})E_{Ph}^2 \left[\exp(\frac{E_{Ph}-\mu}{k_B T}) - 1\right]^{-1}, \tag{2.1}$$

with the constant

$$C = \frac{2\Omega}{h^3 c^2}, \tag{2.2}$$

the spectral emissivity $\tilde{E}(E_{Ph})$, chemical potential of the photon field μ, Boltzmann constant k_B, absorber temperature T, solid angle Ω, Planck constant $h = 2\pi\hbar$ and the speed of light c.
In the case of a semiconductor, where the excited electrons and holes show short momentum and energy relaxation compared to the recombination lifetime, and in the case of open circuit conditions, the chemical potential of radiation equals the splitting of quasi-Fermi levels

$$\mu = E_{F_n} - E_{F_p}, \tag{2.3}$$

with the quasi-Fermi levels for electrons E_{F_n} and holes E_{F_p} [27–29].
For flucos, the chemical potential of the photon field equals the chemical potential of the edge fluorescent photon flux and the chemical potential of the photoexcited dye [30].

[1] Radiation: Electro-magnetic radiation with wavelengths in the near infrared and visible spectrum. This radiation will sometimes just be named light.

2.1.1. Information from PL spectra

Equation (2.1) provides experimental access to parameters like the absorber temperature T, the splitting of quasi-Fermi levels μ and the emissivity $\tilde{E}(E_{Ph})$ which equals the absorption

$$A(E_{Ph}) = 1 - \exp(-\alpha d) = \tilde{E}(E_{Ph}) \tag{2.4}$$

with absorption coefficient $\alpha(E_{Ph})$ and absorber thickness d according to Kirchhoff's law of thermal radiation [8].
In the following sections, it will be demonstrated, as illustrated in Fig. 2.1, how to estimate the parameters mentioned above from the PL yield $\Gamma(E_{Ph})$.

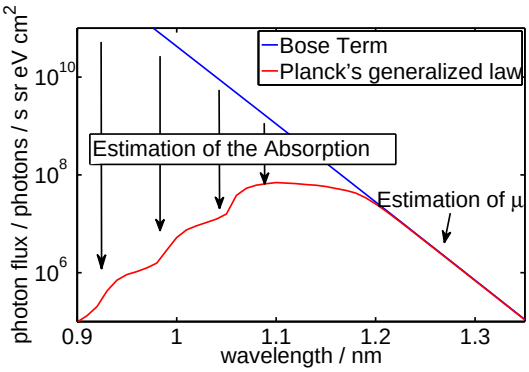

Figure 2.1.: PL spectrum for the emission from excited c-Si with demonstration of the influence of absorption and splitting of quasi-Fermi levels (Phonon bands in 0.9 eV - 1.1 eV in absorption coefficient). This spectrum was simulated with the model from chapter 2.2.2.

2.1.1.1. Temperature T

For photon energies above the band-gap ($E_{Ph} > E_g$) the absorption equals unity ($A(E_{Ph}) \approx 1$) [31, 32] and for $E_{Ph} - \mu \geq k_B T$ the exponential function is large compared to unity so that the Boltzmann approximation can be applied:

$$\Gamma(E_{Ph}) \approx C E_{Ph}^2 \left[\exp\left(\frac{E_{Ph} - \mu}{k_B T}\right)\right]^{-1}. \tag{2.5}$$

This equation can be transformed to

$$\log\left(\frac{\Gamma(E_{Ph})}{C E_{Ph}^2}\right) \approx -\frac{E_{Ph} - \mu}{k_B T} \tag{2.6}$$

by simple algebraic manipulations so that it shows a relation between the logarithmic decrease of the PL yield and the temperature T of the absorber. Here the constant C is not needed, because $\log(\frac{\Gamma(E_{Ph})}{E_{Ph}^2}) \propto -\frac{E_{ph}}{k_b T}$.
This way to measure the absorber temperature would be to complicated, but the temperature T is needed in the following estimations of μ and $A(E_{Ph})$, so it is estimated here.

2.1.1.2. Splitting of quasi-Fermi levels μ

A relation to calculate μ can be directly derived from eq. (2.6):

$$\mu \approx k_B T \log\left(\frac{\Gamma(E_{Ph})}{C E_{Ph}^2}\right) + E_{Ph} \tag{2.7}$$

where the approximation is very good, which means the error due to the Boltzmann approximation is negligible.
If the constant C is not known, because the setup is not calibrated, one can only calculate the difference in the splitting of quasi-Fermi levels between two measurements as demonstrated e. g. in [33].

The splitting of quasi-Fermi levels is very useful, because it gives an estimation of the maximal achievable open circuit voltage V_{OC} of a completely processed solar cell, even from PL measurements on the bare absorber.
This connection between the splitting of quasi-Fermi levels and the open circuit voltage can be confirmed with a simple derivation:
From the 1d stationary diffusion equation for excess carrier density n (eq. (2.51)), which will be introduced later, one can calculate the current density $j = -envv$ with elementary charge e and effective speed of electrons v:

$$\frac{dj}{dx} = g - r \quad \Rightarrow \quad j = -e\left(\frac{r}{g} - 1\right) gd \tag{2.8}$$

with the semiconductor thickness d. Here the generation rate r and recombination rate g are given by the Boltzmann approximation

$$g_{oc} = f_1 n_0 p_0 \exp\left(\frac{\mu_{\mathrm{OC}}}{k_B T}\right) \tag{2.9}$$

$$r_{oc} = f_2 n_0 p_0 \exp\left(\frac{eV_{\mathrm{OC}}}{k_B T}\right) \tag{2.10}$$

for open circuit conditions with the splitting of quasi-Fermi levels μ_{OC}, some constant f_1 and f_2, thermal steady state electron and hole concentration n_0 and p_0 and open circuit voltage V_{OC}. Thus the current density which is zero for open circuit conditions is given by

$$0 = j = -egd\left[\exp\left(\frac{eV - \mu_{\mathrm{OC}}}{k_B T}\right) - 1\right], \tag{2.11}$$

so this equation can only be fulfilled if $eV = \mu_{\mathrm{OC}}$.
For a real solar cell, the internal voltage of the pn-junction is reduced by serial resistances, so that the external open circuit voltage is limited by the splitting of quasi-Fermi levels:

$$V_{\mathrm{OC}} \leq \frac{\mu}{k_B T}. \tag{2.12}$$

An experimental confirmation of this result can be found e. g. for crystalline silicon in [34].

2.1.1.3. Absorption $A(E_{Ph})$

The photon energy dependent absorption is directly given by eq. (2.1):

$$A(E_{Ph}) = \frac{\Gamma(E_{Ph})}{E_{Ph}^2 C}\left[\exp\left(\frac{E_{Ph}-\mu}{k_B T}\right)-1\right]. \tag{2.13}$$

This estimation has the advantage of being extremely sensitive to small absorptions is in the case of photon energies far below the band-gap. But for high absorptions where A is close to one, the absorption coefficient can not be calculated from the absorption by the Lambert-Beer law anymore.

2.2. Propagation of electro-magnetic radiation

In the following the three important ways for the propagation of radiation in the model plotted in Fig. 2.2 will be discussed. This model contains three different layers, namely the absorber itself ($i = 1$), the substrate on which the absorber is deposited ($i = 0$) and the surrounding air ($i = 2$) with different refractive indices n_i, $i = 0, 1, 2$. For thick absorbers like crystalline silicon the substrate can also be air.
Parameters for the propagation of radiation like the wave vector $\vec{k}$ and the reflection and transmission coefficients for the amplitude r_{ij} and t_{ij}, $i, j \in [1, 2, 3]$ are calculated from these refractive indices. The reflection and transmission are given for a radiation propagating from the layer with refractive index n_i to the one with n_j. The absorption coefficient of the absorber $\alpha = \alpha(E_{Ph})$ is also needed to calculate the propagation described below.
Here one has to take into account, that the absorption coefficient α describes the extinction of light for the photon flux or the intensity[2] I, but the propagation of radiation should be calculated with the amplitude P to obtain access to interference effects as well. Thus the absorption coefficient $\tilde{\alpha}$ for the amplitude is also needed, because

$$|A(d)|^2 = |A_0 \exp(-\tilde{\alpha} d)| = I_0 \exp(-2\tilde{\alpha} d) = I_0 \exp(-2\tilde{\alpha} d) = I(d) \tag{2.14}$$

$$\tilde{\alpha} = \frac{1}{2}\alpha, \tag{2.15}$$

so from now on α will be used for the absorption of the photon flux and $\tilde{\alpha}$ for the attenuation of the amplitude.

The three different ways of propagation mentioned above are illustrated in Fig. 2.3: transmission through an absorber with absorption and reflection a), emission from inside an absorber to its top or bottom surface b) and emission from inside an absorber to its edge c). Problems a) and b) can be reduced to a one dimensional problem for a plane wave and a homogeneous emitter and problem c) to a two dimensional one.

[2] The intensity always means the absolute value of the Poynting vector $\vec{S} = \vec{E} \times \vec{H}$, where $\vec{E}$ is the electric field and $\vec{H}$ the auxiliary magnetic field.

For the solution of all problems only the fundamental optics which can be found e. g. in [35, 36] as well as the reflection and transmission coefficients given by

$$r_{ij} = \frac{n_i - n_j}{n_i + n_j} \tag{2.16}$$

$$t_{i,j} = \frac{2n_i}{n_i + n_j} \tag{2.17}$$

will be used.

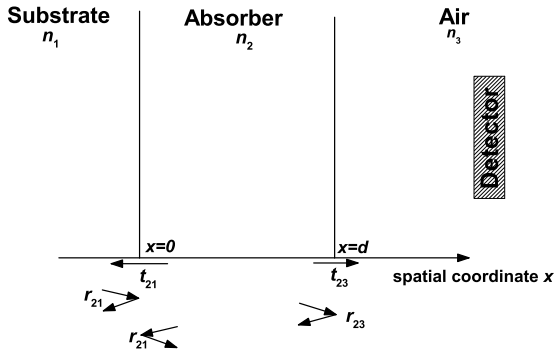

Figure 2.2.: Model for the simulations with three layers (substrate, absorber, air) of different refractive indices n_i. The detector is assumed to be within the air.

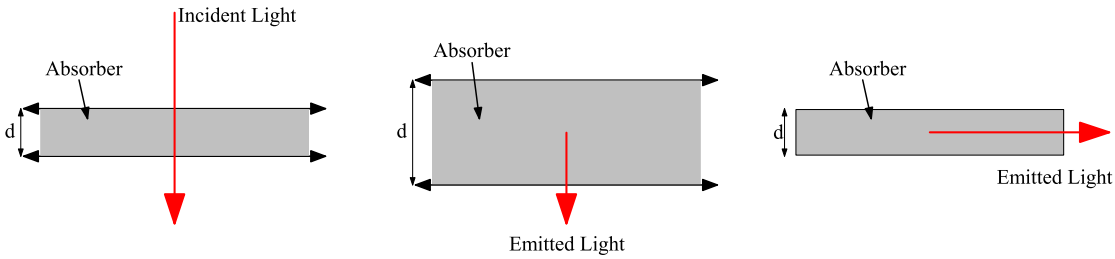

(a) (b) (c)

Figure 2.3.: Different cases for the propagation of radiation. a) through an absorber, b) from inside an absorber to its top and c) from inside an absorber to its edge.

2.2.1. Propagation through a sample

When electro-magnetic radiation hits an absorber, one part of the radiation is transmitted, one part is reflected back and the rest of the radiation is absorbed. Thus it is sufficient to calculate the transmission and reflection.

2.2.1.1. Transmission

An illustration for the reflection on and the transmission of radiation through the absorber is depicted in Fig. 2.4. For the transmission of the amplitude, the incident radiation is given by

the sum over all rays leaving the absorber on the rear end at $x = d$:
The first ray is given by the transmission from air (n_0) to the absorber (n_1) t_{01}, the attenuation by the absorption $\exp(-\tilde{\alpha}d)$, the phase factor $\exp(ikd)$ for the propagation through the absorber and the transmission from the absorber (n_1) to air (n_2) t_{12}. All other rays are given by the same scheme but for larger propagation length $2(m+1)d$ for m additional propagations forth and back through the absorber and multiplied by the appropriate number of reflections on both absorber surfaces r_{12}^m and r_{20}^m:

$$\begin{aligned} t = \quad & t_{01}t_{12}\exp(-\tilde{\alpha}d)\exp(ikd) \\ + \quad & t_{01}t_{12}r_{12}r_{20}\exp(-3\tilde{\alpha}d)\exp(3ikd) \\ + \quad & \dots \\ + \quad & t_{01}t_{12}r_{12}^m r_{20}^m \exp(-(2m+1)\tilde{\alpha}d)\exp((2m+1)ikd) \\ + \quad & \dots \ . \end{aligned} \tag{2.18}$$

As mentioned before, the total transmission of the amplitude is given by the sum over all rays leaving the absorber with a different number m of full propagations through the absorber forth and back, so a reduction to a generalized summation is possible. This sum can be simplified by using $\sum_{m=0}^{\infty}\exp(-mx) = \frac{1}{1-\exp(-x)}$:

$$t = \sum_{m=0}^{\infty} t_{01}t_{12}r_{12}^m r_{20}^m \exp(-(2m+1)\tilde{\alpha}d)\exp((2m+1)ikd) \tag{2.19}$$

$$= \frac{t_{01}t_{12}\exp(-\tilde{\alpha}d)\exp(ikd)}{1 - r_{12}t_{10}\exp(-2\tilde{\alpha}d)\exp(2ikd)}. \tag{2.20}$$

To obtain the transmission of the intensity, one has to calculate the square of the absolute value and multiply with the ratio of the refractive indices of the absorber, in order to account for the specific propagation speeds, and the surrounding material[3]

$$T = |t|^2 \frac{n_2}{n_1}. \tag{2.21}$$

2.2.1.2. Reflection

A similar calculation can be performed for the reflection of the amplitude of the incident radiation on the absorber:
In this case one part r_{01} is directly reflected by the absorber surface, the additional rays in Fig. 2.4 are given by the transmission t_{01} into the absorber, attenuation by the absorption $\exp(-2\tilde{\alpha}d)$ according to the propagation length $2md$ for the number m of full propagations forth and back through the absorber, a respective phase factor $\exp(2mikd)$ and the factors for reflection on the surfaces on the side of incidence r_{10}^{m-1} and on the other side r_{12}^m:

$$r = \quad r_{01}$$

[3] See e. g. [35].

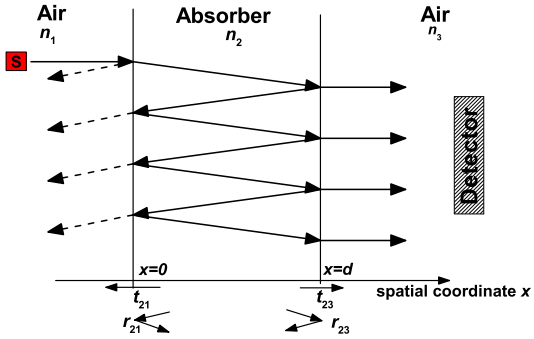

Figure 2.4.: Transmission through and reflection on a sample in the three layer simulation with light source S and propagation of radiation.

$$
\begin{aligned}
&+ \quad t_{01}t_{12}r_{12}\exp(-2\tilde{\alpha}d)\exp(2ikd) \\
&+ \quad t_{01}t_{12}r_{10}r_{12}^2\exp(-2\tilde{\alpha}d)\exp(2ikd) \qquad (2.22) \\
&+ \quad \dots \\
&+ \quad t_{01}t_{12}r_{10}^{m-1}r_{12}^m\exp(-2m\tilde{\alpha}d)\exp(2mikd) \qquad (2.23) \\
&+ \quad \dots \ .
\end{aligned}
$$

Again, the summation over all rays can be reduced to a generalized sum and thus simplified:

$$r = r_{01} + \frac{t_{01}t_{12}r_{12}\exp(-2\tilde{\alpha}d)\exp(2ikd)}{1 - r_{10}r_{12}\exp(-2\tilde{\alpha}d)\exp(2ikd)}. \qquad (2.24)$$

The reflection of the intensity R can be obtained by calculating the square of the absolute value of the reflection of the amplitude:

$$R = |r|^2 . \qquad (2.25)$$

2.2.1.3. Results

The results for transmission T (eq. (2.20) and (2.21)) and reflection R (eq. (2.24) and (2.25)) for the intensity as well as the absorption A given by

$$A = 1 - T - R \qquad (2.26)$$

are discussed using the example of a $d = 20$ µm thick crystalline silicon (c-Si) absorber with the absorption coefficient from Green which will be introduced in chapter 3.5.1 and a refractive index $n_1 = 3.5$ for c-Si and $n_0 = n_2 = 1$ for air. In this case, the c-Si is so thin that it shows interference effects.
Results of the transmission, reflection and absorption are plotted in Fig. 2.5. One can observe two photon energy regimes with different optical behaviour. For $E_{Ph} \leq 1.05$ eV the transmission is positive ($T > 0$), whereas the transmission is zero ($T = 0$) for $E_{Ph} > 1.05$ eV.
If the transmission is not zero, the reflection, transmission and absorption show interference

effects which result from the superposition of the different rays computed above. Here the maxima of transmission are located at photon energies where absorption and reflection have minima and vice versa.
In the case of negligible transmission, no radiation reaches the back surface of the absorber, so either the radiation is reflected at the surface or absorbed, and there are no interference effects observable.

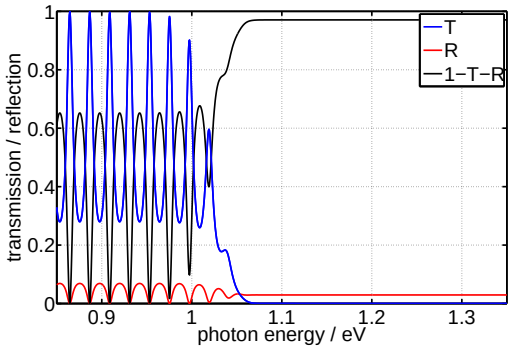

Figure 2.5.: Comparison of absorption $A = 1 - T - R$, reflection R and transmission T for $d = 20$ µm thick c-Si.

2.2.2. From inside a sample to the top or bottom surface

Problem b) mentioned in chapter 2.2, the source of radiation is located inside the absorber and the aim is to calculate the part of the emitted radiation leaving the top or bottom surface. Here the calculation is similar to the one for the propagation through the absorber but the rays illustrated in the model in Fig. 2.6 have to be added up.
In this case, the radiation of the infinitesimal small source S with amplitude P is divided into two parts with amplitude $P/2$: one for the propagation in the positive x-direction and one for the propagation in the negative x-direction.

Propagation in the positive x-direction (right direction):
All ways from source S to the detector with propagation in positive x-direction are given by the absorption $\exp(-\tilde{\alpha}(d-x))$ on the path from x to d, the respective phase factor $\exp(ik(d-x))$ and the transmission t_{12} through the surface multiplied with absorption $\exp(-\tilde{\alpha}2d)$, phase factor $\exp(ik2d)$ and reflections r_{12} and r_{10} on both surfaces for each additional full propagation forth and back through the absorber:

$$\begin{aligned}\frac{P}{2} \quad \times \quad & [t_{12}\exp(-\tilde{\alpha}(d-x))\exp(ik(d-x)) \\ + \quad & t_{12}\exp(-\tilde{\alpha}(d-x))\exp(ik(d-x))r_{10}r_{12}\exp(-\tilde{\alpha}2d)\exp(ik2d) \\ + \quad & \dots \\ + \quad & t_{12}\exp(-\tilde{\alpha}(d-x))\exp(ik(d-x))r_{10}^{m}r_{12}^{m}\exp(-\tilde{\alpha}2md)\exp(ik2md) \\ + \quad & \dots] \,. \end{aligned} \tag{2.27}$$

As before, this summation can be generalized with a counter m for the number of full (forth and back) propagations through the sample

$$\frac{P}{2} \quad [t_{12}\exp(-\tilde{\alpha}(d-x))\exp(ik(d-x)) \times \sum_{m=0}^{\infty} r_{10}^m r_{12}^m \exp(2mikd)\exp(-2m\tilde{\alpha}d). \tag{2.28}$$

Propagation in the negative x-direction (left direction):
For the propagation in the opposite direction only the first part from source S to the surface is different, because the electro-magnetic wave has to propagate to the surface at $x = 0$, is reflected back with a factor r_{10} and propagates to the surface at $x = d$. The appropriate generalization is given by:

$$\frac{P}{2} \quad [r_{10}t_{12}\exp(-\tilde{\alpha}(d+x))\exp(ik(d+x)) \times \sum_{j=0}^{\infty} r_{10}^j r_{12}^j \exp(2jikd)\exp(-2ja\tilde{\alpha}d). \tag{2.29}$$

The amplitude reaching the detector from source S in position x is given by the sum of eq. (2.28) and eq. (2.29):

$$\frac{P}{2} t_{12} \mathrm{e}^{-2\tilde{\alpha}(d-x)} \mathrm{e}^{2ik(d-x)} \frac{1 + r_{10}\mathrm{e}^{-2\tilde{\alpha}x}\mathrm{e}^{2ikx}}{1 - r_{10}r_{12}\mathrm{e}^{-2\tilde{\alpha}d}\mathrm{e}^{2ikd}}. \tag{2.30}$$

Thus the photon flux reaching the detector from absorber position x is given by the square of the absolute value of eq. (2.30)

$$\Gamma(\omega, x) = \Gamma(\omega)\frac{t_{12}^2}{4}\mathrm{e}^{-2\alpha(d-x)} \left| \frac{1 + r_{10}\mathrm{e}^{-2\alpha x}\mathrm{e}^{2ikx}}{1 - r_{10}r_{12}\mathrm{e}^{-2\alpha d}\mathrm{e}^{2ikd}} \right|^2, \tag{2.31}$$

with the photon flux emitted by the source S given by Planck's generalized law (eq. (2.1)). To get the overall photon flux reaching the detector from the absorber, one has to integrate the spatially dependent flux (eq. 2.31) over all absorber positions x:

$$\Gamma_{\mathrm{total}}(\omega) = \int_0^d \Gamma(\omega, x)dx. \tag{2.32}$$

This integral was solved numerically with MatLab [37].
The radiation emitted on the other side of the absorber can be calculated in the same way.

This simulation is not perfect, because emission of the reabsorbed radiation is neglected. For an indirect semiconductor, this approximation is fine, because only 1% ([38]) of the recombination of electrons and holes is caused by radiative recombination, so the influence of the PL photon flux on the excess carrier concentration is negligible, but for an absorber with higher radiative recombination the error of this calculation is inceased, so that the effect of the reemission is not

negligible anymore.
A comparison of the simulation with the analytical solution from Würfel [39]

$$R_{int} = r_{12}^2 \tag{2.33}$$

$$\breve{A}(E_{Ph}) = \frac{(1-R_{int})(\exp(-\alpha d))}{1-R_{int}\exp(-\alpha d)} \tag{2.34}$$

$$\Gamma_W(\omega) = \breve{A}(E_{Ph})\frac{E_{Ph}^2}{4\pi\hbar^3 c^2}\frac{1}{\exp(\frac{E_{Ph}-\mu}{k_B T})-1} \tag{2.35}$$

together with eq. (2.1) is plotted in Fig. 2.7. The simulation is done for a thin c-Si absorber with $d = 20$ µm, refractive indices $n_1 = 1$, $n_2 = 3.5$ and $n_3 = 1$ and absorption given by the one in Fig. 2.23. The results are identical for high photon energies and for low photon energies. The simulation described above yields the interference effects which are not given by the solution of Würfel.

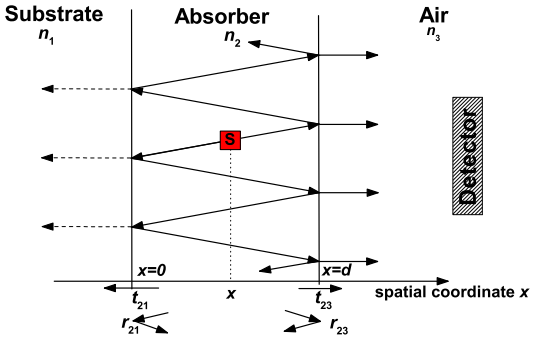

Figure 2.6.: Model for the calculation of the emission from inside an absorber to the top or bottom surface.

2.2.2.1. Comparison with propagation through a sample

Both the calculations and the results for the transmission through a sample and from inside the sample to its top or bottom of the sample are nearly identical, so it is worthwhile to look more closely at the similarities and the differences.
Fig. 2.8 (left) shows the transmission through a sample with the absorption coefficient from Fig. 2.23 and an absorber thickness of $d = 20$ µm and the emission from an absorber with homogeneous emission in the depth[4] within the absorber for the transmission to one side of the absorber. There are two differences between these transmissions:
First, the maximum transmission for photon energies below the band-gap at $E_g = 1.1$ eV is only around 0.5 for the transmission from inside the absorber whereas the transmission through the absorber is up to one. The reason for this difference is that every source in the absorber emits

[4]Note: The source is assumed to be in every position within the absorber and the emission from every position is integrated to receive the total emission.

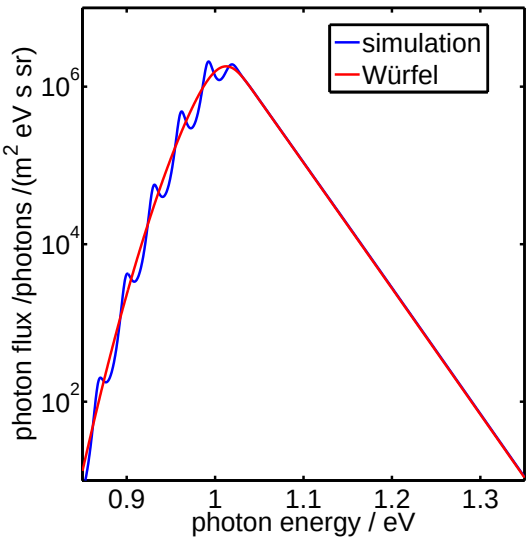

Figure 2.7.: Comparison of the simulation for the PL emission through the top or bottom of the absorber with the analytical result from Würfel [39] for a $d = 20$ µm thick c-Si absorber.

only 50% of the radiation in one direction, so that at most 50% of the radiation of the source can leave the absorber on one side ($n_1 = n_3$).
The second difference is the higher transmission from inside an absorber than through an absorber for photon energies above the band-gap at $E_g = 1.1$ eV. This kind of photons have a shorter propagation length inside the absorber when emitted by a source within compared to complete transmission. Thus the photon flux for higher photon energies is higher for the transmission from inside an absorber than for the transmission through it.
The same behaviour can also be observed for the emission from only one source with an emitter position[5] in the absorber compared to the transmission through the whole absorber in Fig. 2.8 (right). Here the transmissions are normalized. Apart from the two effects described above one can see that the transmission for different source positions inside the absorber does not reproduce each maximum of the transmission through the whole absorber, and the maxima are not always at the same photon energy but are slightly shifted. The reason for this energy shift is obscure, since it is above the numerical inaccuracy and such a shift is not expected.
For one maximum the photon energy is plotted vs. the source position inside the absorber in Fig. 2.9 (left) in comparison to the photon energy of the maximum of the complete transmission. When the photon energy of the maximum is below $E_{Ph} < 0.85$ eV, this absorber position generates no maximum in the transmission with the specified photon energy.
In the case of the emission inside the absorber not being equal for all absorber positions but being given by Planck's generalized law (eq. (2.1)) the transmission from different absorber positions is plotted in Fig. 2.9 (center). Here also some maxima and minima are "missing" in the transmitted

[5]Note: This is only the emission from one absorber position.

radiation.

A comparison of the positions where maxima of both transmissions are present and where the maximum for the transmission from inside the absorber is not existent is plotted in Fig. 2.9 (right). The scale indicates the transition from no maximum (0) to both maxima present (2). The photon energies for the five maxima are listed in Tab. 2.1.

This result is interesting, because the positions, where the transmission from inside the absorber show no maximum at a photon energy at which the transmission through the whole absorber does show a maximum, are distributed non symmetrically throughout the absorber and the distance between these positions is given by $\lambda/2$ with the wavelength λ.

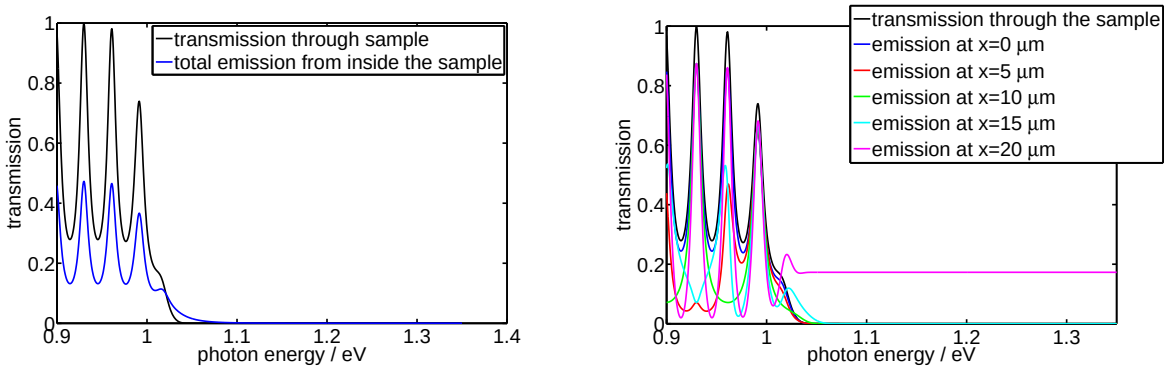

Figure 2.8.: Comparison of the transmission from a source inside a sample and the transmission through a sample for the full absorber (left) and transmission only from one emission position (right).

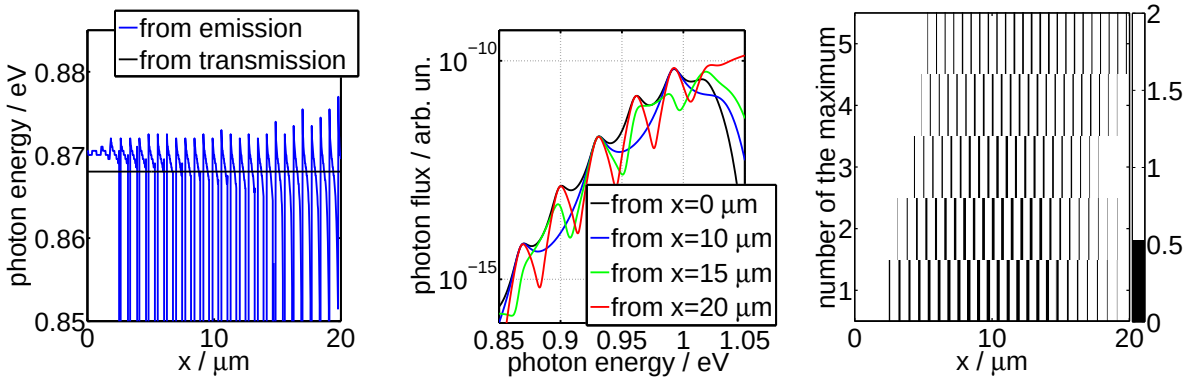

Figure 2.9.: Emission from inside an absorber to one surface for different positions of the emission source inside the absorber vs. the transmission through the whole absorber (left), depth dependence of the transmission maximum around $E_{Ph} = 0.87$ eV (center) and results of the comparison of maxima vs. absorber position (right) ($d = 20$ µm thick c-Si wafer).

Table 2.1.: Photon energies for the maxima in Fig. 2.9 (right).

Maximum	Photon energy / eV
1	0.868 ± 0.001
2	0.899 ± 0.001
3	0.930 ± 0.001
4	0.961 ± 0.001
5	0.991 ± 0.001

2.2.2.2. Angular dependent emission from top

One aim of this thesis is to characterize the effect of a photonic crystal on top of an absorber on the emitted PL yield through such a photonic crystal. Therefore the angular dependent emission of a flat absorber is calculated first in order to understand this emission.
The previous calculation has to be modified: The reflection and transmission coefficients r_{ij} and t_{ij} for different emission angles α are given by the Fresnel equations for p- and s-polarized radiation

$$\begin{aligned} t_{12,s} &= \frac{2n_1\cos(\alpha)}{n_1\cos(\alpha)+n_2\cos(\beta)} \\ r_{12,s} &= \frac{n_1\cos(\alpha)-n_2\cos(\beta)}{n_1\cos(\alpha)+n_2\cos(\beta)} \\ t_{12,p} &= \frac{2n_1\cos(\alpha)}{n_2\cos(\alpha)+n_1\cos(\beta)} \\ r_{12,p} &= \frac{n_2\cos(\alpha)-n_1\cos(\beta)}{n_2\cos(\alpha)+n_1\cos(\beta)} \end{aligned} \tag{2.36}$$

and the propagation length inside the absorber for absorption and transmission has to be changed from l to $l/\cos(\beta)$ where β is given by

$$\beta = \arcsin\left(\frac{n_2}{n_1}\sin(\alpha)\right) \tag{2.37}$$

from the angle of detection α by Snell's law

$$\frac{\sin(\alpha)}{\sin(\beta)} = \frac{n_1}{n_2}. \tag{2.38}$$

The simulation is based on the idea, that the emitted radiation from an absorber position x travels under the angle β inside the absorber in both directions, and, when hitting the surfaces, one part is transmitted and the other part is reflected back. The reflected radiation behaves in the same way. All radiation transmitted out of the absorber into the positive x-direction (right direction) is assumed to reach the detector, so that the rays still can interfere.
In addition, there is an angular enlargement due to Snell's law, which will be discussed in chapter 2.2.3.1 in detail, and which reduces the photon flux for larger angles. Results for the angular dependent emission of a $d = 10$ µm thick c-Si absorber with refractive index $n = 3.5$ are plotted in Fig. 2.11: The angular dependence of the PL yield at $E_{Ph} = 1.1$ eV for s- and p-polarized

light and also for a mixture of both polarizations are plotted in Fig. 2.11 (left) and the spectral dependent emission for a few emission angles and s- and p-polarized emission in Fig. 2.11 (right). In an experiment the emission should be unpolarized which corresponds to 50% s- and 50% p-polarized contributions.
Due to the perfect transmission for p-polarized light at Brewster's angle the emission for p-polarized light decreases more weakly than the emission of s-polarized light with increasing emission angle. The the maximum of the angular dependent emission for p-polarized light is at an angle of zero degrees like for s-polarized light, because the angular enlargement reduces the photon flux more strongly than the perfect transmission increases the photon flux.
One direct impact of the higher transmission for p-polarized light than for s-polarized light is a reduction of the interference effects for p-polarized emission whereas the interference effects for s-polarized light are increased with the emission angle. These interferences occur also at different photon energies, because the absorber seems to be thicker under larger emission angles.
Unfortunately no absorber with an adequate and homogeneous thickness to measure the interferences was available to compare these results with experimental data, but a comparison with a $d = 250$ µm thick crystalline silicon wafer will be given in chapter 4.2.3, where no interferences are observed.

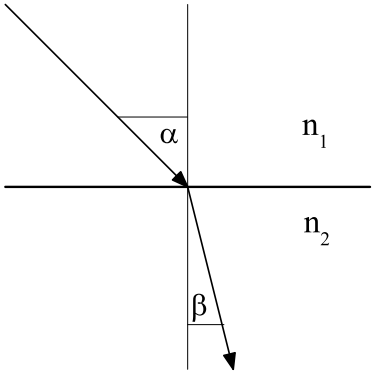

Figure 2.10.: Definition of α and β.

2.2.3. From inside a sample to the edge

For the propagation of radiation to the edge of a thin absorber there are two important cases. Either the absorber/emitter is positioned only on top of a substrate and the radiation mainly propagates through the substrate or the absorber/emitter is distributed throughout the full material without a transparent substrate. In the case of flucos, the dye in a matrix material is either on top of a glass substrate or homogeneously distributed through the matrix material without a glass substrate. Both cases will be discussed below.

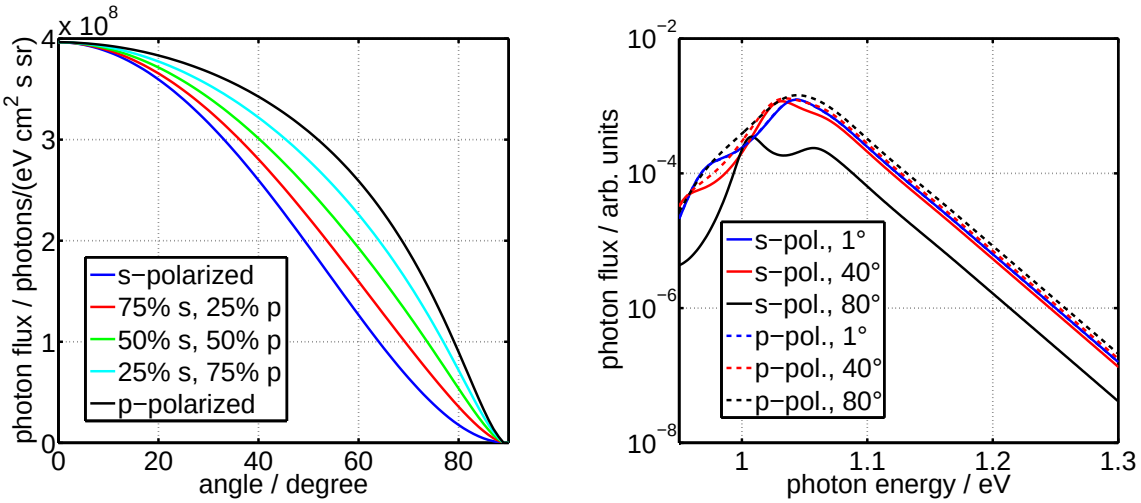

Figure 2.11.: Simulated angular dependence of the emission on the top or bottom of an excited $d = 10$ µm thin c-Si absorber (left) and spectral difference between various emission angles for both polarizations (right). Note: The spectrum for s-polarized radiation with an emission angle of 1° equals that for p-polarized radiation with a 1° angle.

2.2.3.1. Fluco with dye on top

Fig. 2.13 (left) shows a sketch of the idea: The excitation laser (the diameter of the laser is assumed to be infinitesimally small) hits the fluco on the top with a distance x to the edge of the fluco for which the emission is calculated, the thickness is $d = 1$ mm and the emission of the dye is isotropic within an angle $\alpha \in [0°, 90°]$; other emission angles are of no interest, because this radiation leaves the fluco either through the top or through the other edge. Each ray of the emitted light hits the surface of the edge with a certrain distance h to the top of the fluco.
The angles of the emitted light outside the fluco are given by Snell's law (see Fig. 2.12)

$$\beta = \arcsin\left(\frac{n_{\text{fluco}}}{n_{\text{air}}}\sin(\alpha)\right) = \arcsin(1.5\sin(\alpha)) \tag{2.39}$$

with a refractive index $n_{\text{fluco}} = 1.5$ for the fluco and $n_{\text{air}} = 1$ for air and the distance to the top of the absorber

$$h = x \cdot \arctan(\alpha). \tag{2.40}$$

This distance is a virtual distance to the top of the absorber, because a distance $h > d$ and $h < 2 \cdot d$ means that the ray emitted under the associated angle hits the edge after being reflected at the back of the fluco and is emitted from the edge under the angle of $-\beta$ as illustrated in Fig. 2.13 (center). For even larger distances h the emission angle is given by the case-by-case analysis in Tab. 2.2. The emission for $h > 2 \cdot d$ and $h < 3 \cdot d$ is also illustrated in Fig. 2.13 (right). The photon flux of the radiation leaving the edge of the fluco is given by the emitted photon flux of the emission source on top of the fluco, by the transmission coefficient at the edge of the fluco from Fresnel's equations (eq. 2.37) and finally by the increase of the angle increment $d\beta$ according to Snell's law (eq. (2.38)). Note that the reflection coefficient on back and top surfaces

of the fluco is one due to total internal reflection, at least for a perfectly flat fluco surface and for the emission angles which occur.

Source of radiation:
In the literature a discussion can be found about the angular dependence of the dye emission: Goldschmidt [41] assumes an anisotropic emission given by a term from Zastrow [42] for the likelihood $P(\vartheta)$ for emission at an angle ϑ

$$P(\vartheta) = 1 + \gamma \cdot \cos(\vartheta)^2, \tag{2.41}$$

with an anisotropy coefficient γ, whereas a random orientation of the dye molecules in the fluco suggests an isotropic emission.
In the following treatment a isotropic emission (i. e. $\gamma = 0$) is assumed and only a qualitative explanation is given of what would change if the emission would be not isotropic.

Transmission coefficient:
In the case of a fluorescence dye, the emitted radiation is assumed to be unpolarized, so the transmission coefficient for the photon flux of the transmitted radiation is given by

$$T = 0.5 \cdot T_p + 0.5 \cdot T_s \tag{2.42}$$

with the transmission coefficients for the photon flux of p- and s-polarized radiation which are given by

$$T_i = \frac{n_2 \cos(\beta)}{n_1 \cos(\alpha)} \cdot t_i^2, \tag{2.43}$$

for both polarizations ($i = s, p$), with t_i given by Fresnel's equations (eq. (2.37)) for $n_1 = 1.5$ and $n_2 = 1$.

Increase of the angle increment $d\beta$:
Due to the nonlinearity of Snell's law (plotted in Fig. 2.12) the radiation of a source in the top region of the fluco in the angular range between α and $\alpha + d\alpha$ is emitted at the edge of the fluco into the angular range between β and $\beta + d\beta$ with β given by Snell's law (eq. (2.38)) and $d\beta$ given by

$$d\beta = \frac{1}{\sqrt{1 - \frac{n_2}{n_1}\sin(\alpha)}} \frac{n_2}{n_1} \cos(\alpha) d\alpha. \tag{2.44}$$

The radiation transmitted through the edge of the fluco ($\Gamma(\beta)$) is collected and transported to the detector system, as will be described in chapter 3.1, with an angular resolution $\Delta\theta$, here $\Delta\theta = 1.5°$. So the photon flux of the radiation collected at an angle β is given by

$$\Gamma_{\text{detector}}(\beta) = \int_{-0.75°}^{+0.75°} \Gamma(\beta + \theta) d\theta. \tag{2.45}$$

In Fig. 2.14 (left) shows the angularly resolved result of the calculated and integrated edge emission from a fluco with a size of $A = 25 \times 25$ mm^2 and a thickness of $d = 1$ mm, with

the dye on top of the absorber but without reabsorption, for different excitation positions on top of the fluco defined by the distance x to the edge. The result is interesting, because the angularly dependent "detection" at the edge either does or does not show emission, depending on the excitation position. The respective angles are given by the case-by-case analysis discussed in above. The envelope of the emission is reduced with increasing absolute value of the emission angle due to Fresnel's equations and the increase of the angle increment.
A more detailed discussion of the fluco edge emission for a fluco with dye on top with wavelength dependent emission sources and reabsorption can be found in [40, 43].
In chapter 4.3.3 these results will be compared with the experimentally measured edge emission for a fluco with dye on a glass substrate.

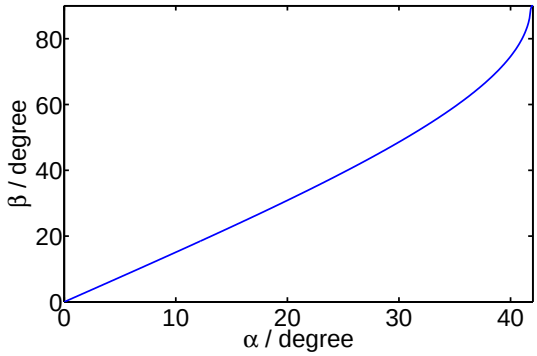

Figure 2.12.: Angle of incidence (α) vs. angle of the diffracted radiation (β) given by Snell's law for the refraction of radiation on a phase border between a refractive index of $n_1 = 1.5$ and $n_2 = 1$.

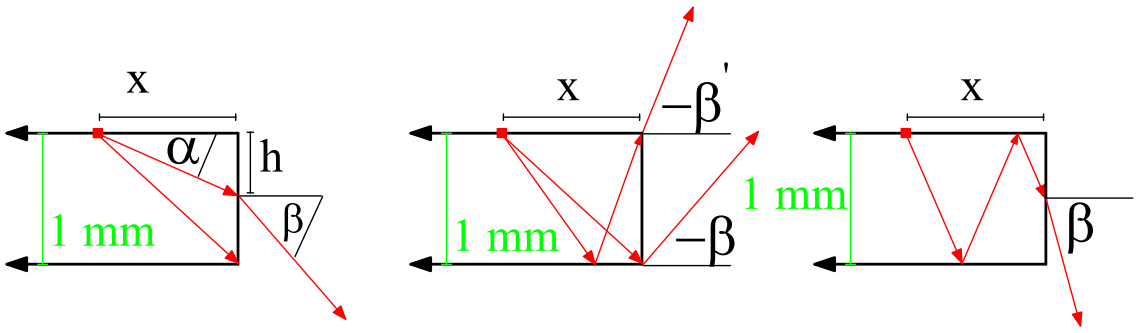

Figure 2.13.: Sketch for the numerical calculation of the edge emission for a fluco with the dye on top. Left: model for the simulation with excitation at a distance x from the edge of the fluco, emission angle α, emission from the edge at a distance h from the top of the fluco under the angle β; center: emission with one reflection on the back surface with an emission angle of $-\beta$ and $-\beta'$; right: emission with one reflection on the back surface and one reflection on the top surface of the fluco and with emission angle β at the edge of the fluco.

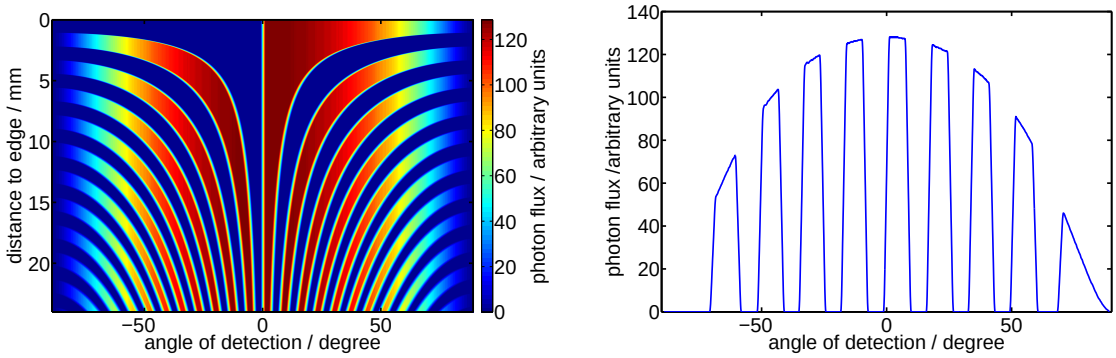

Figure 2.14.: Simulated angularly resolved emission of the fluorescence at the edge of a fluco for different excitation positions (distance to the edge x) on the fluco (left) and angular dependent emission at the edge for an excitation at x=10 mm from the edge (right).

Table 2.2.: Case-by-case analysis for the parameter h and the respective sign of the emission angle at the fluco edge for a fluco with dye on top of a substrate and homogeneous dye concentration.

h	sign(β): Dye on top	sign(β): Homogeneous dye concentration
$\vdots$	$\vdots$	$\vdots$
$-3d..-2d$		+
$-2d..-d$		-
$-d..0$		+
$0..y$	+	-
$y..d$	+	+
$d..2d$	-	-
$2d..3d$	+	+
$3d..4d$	-	-
$4d..5d$	+	+
$\vdots$	$\vdots$	$\vdots$

2.2.3.2. Fluco with homogeneous dye concentration

In the case of the dye being homogeneously distributed throughout the fluco, the situation is a little different from the one described above, because the source of emission is not only on top of the fluco but in each depth position. By consequence, in order to calculate the emission from the edge of such a fluco, the emitted radiation additional to the one from the top of the fluco has to be added.
First, the radiation for an emitter position inside the fluco ($y \in]0, d[$) reaching the edge of the absorber is emitted under an angle in the range of $-90° \leq \alpha \leq 90°$, because the radiation emitted into the upper right quarter is also emitted inside the fluco. Because of the distance from the top to the emitter, the virtual distance between the top of the fluco and the position where the radiation reaches the edge is given by

$$h = x \cdot \arctan(\alpha) + y \tag{2.46}$$

instead of eq. (2.40) for the fluco with dye on top. And the case-by-base analysis has to be modified as illustrated in Fig. 2.15, where the relation between the position on the edge (h) and the sign of the emission angle β is given. The resulting sign of β is also given in Tab. 2.2.

Fig. 2.16 shows the result of the simulation for a constant emission for different depth positions whereas Fig. 2.17 shows the result for a depth dependent emission $P(y)$ given by the relation

$$P(y) = \exp(-100/\text{cm} \cdot y), \tag{2.47}$$

with particular geometric magnitudes, which should be more realistic, because the photon flux of the incident light is reduced due to absorption. Both figures show the angular dependent edge emission for different excitation positions on the top as well as the edge emission for a homogeneous excitation (excitation on all fluco positions x) on the top of the fluco.
The results for homogeneous depth emission are symmetrical regarding positive and negative emission angles β because the upper half of the fluco emits the same amount of radiation under negative angles as the lower half under positive ones and vice versa, so the sum of the emission of both fluco halves (upper and lower halves) are identical.
This symmetry is broken however, when the emission profile equals e. g. an exponential decay from the top of the fluco to the bottom, because then the emission of the upper half is stronger than the emission of the lower half.
One important result is the non-symmetric emission around $\beta = 0°$, which is a result of the exponential decay of the emission from top to bottom and not a result of an anisotropic emission as suggested in [41].
Anisotropic emission as mentioned above leads to a broader or narrower angular dependent edge emission (but just slightly different from the results discussed above) and not to an asymmetric edge emission.
The results here indicate that the dye emission is fairly isotropic.

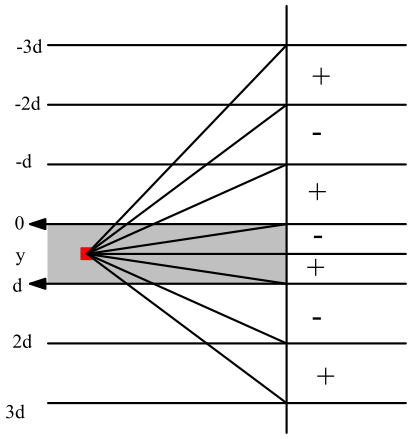

Figure 2.15.: Illustration of the case-by-case analysis for the emission at the edge of a fluco with homogeneous dye concentration.

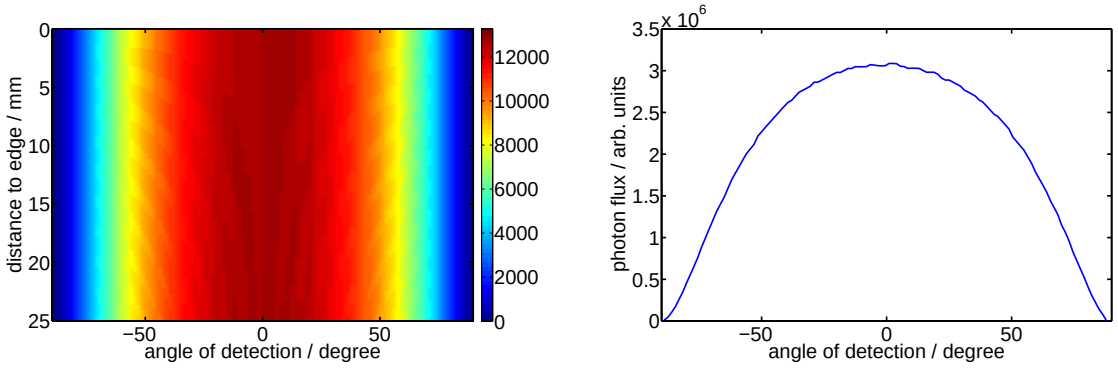

Figure 2.16.: Simulated angular dependent edge emission for different excitation positions on the top of the fluco (left) and edge emission for homogeneous excitation (right) for a fluco with homogeneous dye concentration and homogeneous emission in the depth.

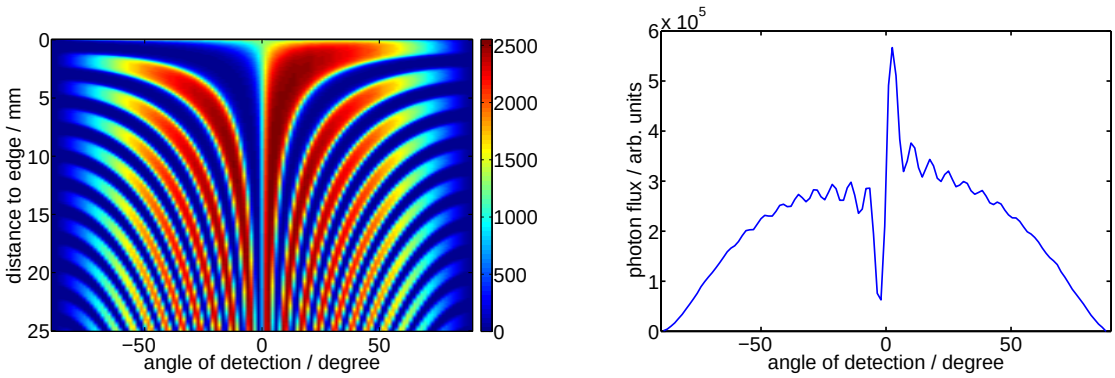

Figure 2.17.: Simulated angular dependent edge emission for different excitation positions on the top of the fluco (left) and edge emission for homogeneous excitation (right) for a fluco with homogeneous dye concentration and exponentially reduced emission in the depth.

2.3. Excess carrier density

The PL emission of a semiconductor is the result of the emission of photons induced by the recombination of electrons and holes, so that the photon flux of the PL emission is strongly influenced by the spatial concentration of the excess carriers. In the case of excited electrons and holes showing short momentum and energy relaxation times compared to the recombination lifetime, the connection between the photon flux of the emission (eq. 2.1) and the excess carrier concentration is given by the equality of the chemical potential of radiation and the splitting of quasi-Fermi levels [27–29]

$$\mu = E_{F_n} - E_{F_p} \tag{2.48}$$

with the quasi-Fermi levels for electrons E_{F_n} and holes E_{F_p}, respectively. This quasi-Fermi level splitting is directly given by the excess carrier concentration $n(x)$ (Boltzmann approximation)

$$E_{F_n} - E_{F_p} = k_b T \ln\left(\frac{n(x)p}{n_i^2}\right) = \mu(x), \tag{2.49}$$

where p denotes the constant hole concentration (for p doped samples and sufficient low excitation) and n_i the intrinsic carrier concentration.
The excess carrier concentration $n(x)$ is defined by the stationary continuity equation for diffusion

$$\mathrm{div}(n\vec{v}) = g - r \tag{2.50}$$

with the effective velocity of the electrons $\vec{v}$, generation rate g and recombination rate r. Here the generation is given by the absorption, e. g. of an excitation laser $g = G_0 \exp(-\alpha x)$ with the photon flux of the laser G_0 and the absorption coefficient of the absorber for the photon energy of the laser α, and the recombination is given by $\frac{n(x)}{\tau_0}$ with the effective excess carrier lifetime τ_0 for all recombination processes involved, i. e. both radiative and non-radiative recombination.
For a one-dimensional treatment, eq. (2.49) can be reduced to

$$-D_c \frac{d^2 n(x)}{dx^2} + \frac{n(x)}{\tau_0} = G_0 \exp\left(-\alpha(x-d)\right), \tag{2.51}$$

for excitation of a semiconductor with thickness d from the side $x = d$. D_c denotes the diffusion coefficient which is connected to the excess carrier lifetime by the diffusion length L via

$$L = \sqrt{\tau_0 * D_c}. \tag{2.52}$$

The boundary conditions are given by the surface recombination on both absorber surfaces ($S_{0,d}$ for the surface recombination velocities on the surfaces at $x = 0$ and $x = d$, respectively):

$$\mp \left.\frac{dn}{dx}\right|_{x=0,d} D_c = n(x = 0, d) S_{0,d}. \tag{2.53}$$

2.3.1. Analytical solution of the continuity equation

The solution of the 1d continuity equation (eq. (2.51)) is given by three exponential functions, two for the solution of the homogeneous equation and one for the inhomogeneous part:

$$n(x) = A \exp(x/L) + B \exp(-x/L) + G \exp(-\alpha x). \tag{2.54}$$

This leads to the following equations for A, B and G

$$A = \frac{G}{\frac{S_0}{D_c} - \frac{1}{L}} \cdot \left[\beta \cdot (\frac{S_0}{D_c} + \frac{1}{L}) - (\frac{S_0}{D_c} - \alpha)\right] \tag{2.55}$$

$$B = -G \cdot \beta \tag{2.56}$$

$$G = \frac{g_0 \tau_0}{1 - (\alpha L)^2} \tag{2.57}$$

$$\beta = \frac{\left(\frac{S_0}{D_c} - \frac{1}{L}\right) \cdot \left(\frac{S_d}{D_c} - \alpha\right) \mathrm{e}^{-(\alpha + \frac{1}{L})d} - \left(\frac{S_0}{D_c} + \alpha\right) \left(\frac{S_d}{D_c} + \frac{1}{L}\right)}{\left(\frac{S_0}{D_c} - \frac{1}{L}\right) \left(\frac{S_d}{D_c} - \frac{1}{L}\right) \mathrm{e}^{-\frac{2}{L} D_c} - \left(\frac{S_0}{D_c} + \frac{1}{L}\right) \left(\frac{S_d}{D_c} + \frac{1}{L}\right)}. \tag{2.58}$$

Strictly speaking, these solutions are only valid for $\alpha L \neq 1$. In the case that $\alpha L = 1$, one would have to use a different "Störungsansatz" with

$$n(x) = x \cdot G \exp(-\alpha x) \tag{2.59}$$

to obtain a valid solution, which however would lead to the same result.

2.3.1.1. Results of the PL for the analytical solution

The result of the calculation of the PL emitted from an excited absorber is influenced by many parameters (especially by parameters for the excess carrier concentration) as described above. The aim of this work is to demonstrate methods to characterize new materials mentioned in chapter 1 which influence the propagation of radiation, so a detailed characterization of the relation of the parameters and the emitted PL yield need not be given here. Only the most important results concerning the estimation of the splitting of quasi-Fermi levels will be given; a more detailed discussion can be found in [44].
The influence of different surface recombination velocities S_d on the side of the excitation or detection ($x = d$) and a constant excess carrier concentration on the other side ($x = 0$) of the

absorber on the excess carrier concentrations is demonstrated in Fig. 2.18 (left) for a $d = 20$ µm thick absorber with the absorption coefficient of c-Si from [82] and with a refractive index of $n = 3.5$ on a glass substrate with $n = 1.5$. The resulting PL spectra plotted in Fig. 2.18 (right) show nearly the same PL yields for low photon energies but a different PL yield for high photon energies. A reason for this behavior is the shape of the absorption coefficient of the semiconductor: The absorption coefficient grows with the photon energy of the PL photons so that the origin of a photon with high photon energy reaching the detector can only be near the surface of the semiconductor whereas photons with low photon energy can reach the detector from every absorber position.
As a result of this behavior, a change in the excess carrier concentration near the emission surface of the semiconductor has a stronger influence on the PL yield for high photon energies than on that for low photon energies. This feature is used in Appendix C to discuss a possibility to estimate the excess carrier concentration with the parameters of the surface recombination velocities and the excess carrier lifetime from PL yields.
One important result of these excess carrier densities and PL yields is the linearity between the splitting of quasi-Fermi levels calculated from the PL yield for high photon energies (estimation described in chapter 2.1.1.2) and that one calculated from the excess carrier concentration on the top of the absorber (red squares in Fig. 2.19) by eq. (2.49). In contrast to this, the splitting of quasi-Fermi levels calculated from the maximum excess carrier concentration has no linear relation to that calculated from the PL yield at high photon energies (blue triangles in Fig. 2.19) for higher photon energies but the linearity is observable for reasonably low surface recombination velocities which would be needed for a production of solar cells.

2.3.2. Numerical solution of the continuity equation for $\tau(x)$

Until now, the model used to calculate the excess carrier density depth profile is rather simple so that the differential equation for the excess carrier density $n(x)$ can be solved analytically. The calculation is more complicated when the excess carriers have a depth dependent lifetime $\tau(x)$, which can result from defects diffused through the top of the absorber (at $x = d$ in the model from above) into the upper part of the absorber. Then a hypothetic excess carrier lifetime may be given by

$$\frac{\tau(x)}{\tau_0} = \tau_0 - \tau_f \frac{1}{\exp(\frac{x_0 - x}{\gamma} + 1)} \tag{2.60}$$

with a reduction of the lifetime from τ_0 to $\tau_0 - \tau_f$, the mean defect diffusion depth x_0 and a parameter for the standard deviation of the defect diffusion length γ. Such a lifetime profile is plotted in Fig. 2.20 with illustration of the three parameters defining the excess carrier lifetime depth profile (ECLDP).
As a result, the differential equation for the excess carrier concentration (eq. (2.51)) is modified slightly to read

$$-D_c \frac{d^2 n(x)}{dx^2} + \frac{n(x)}{\tau(x)} = G_0 \exp\left(-\alpha(x - d)\right), \tag{2.61}$$

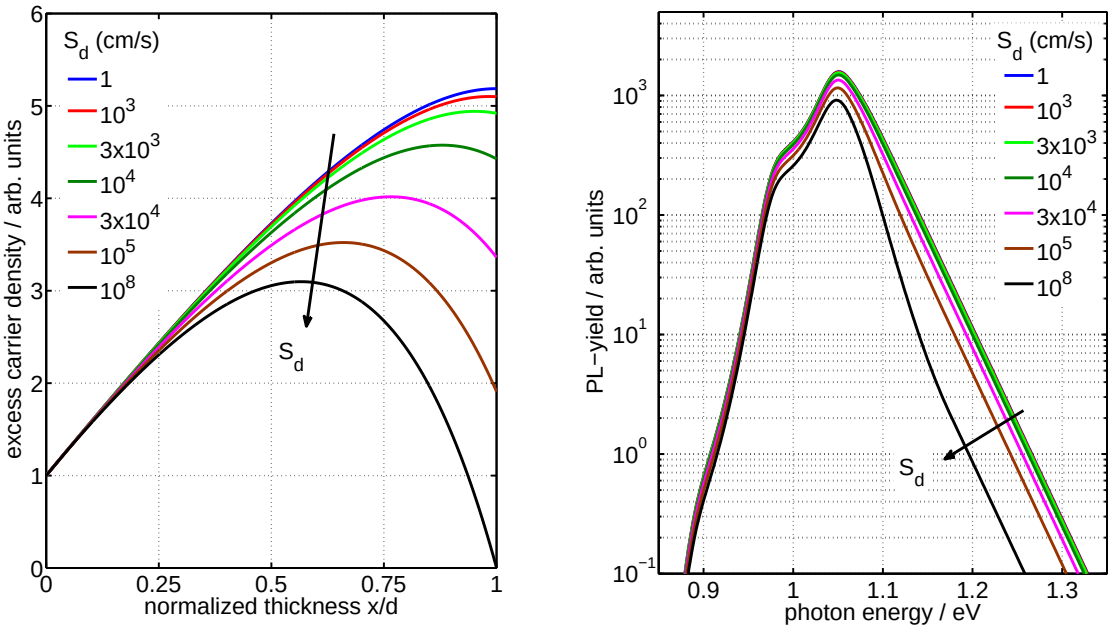

Figure 2.18.: Different excess carrier concentrations for different recombination velocities on the top of the absorber (left) and the resulting PL-yields (right).

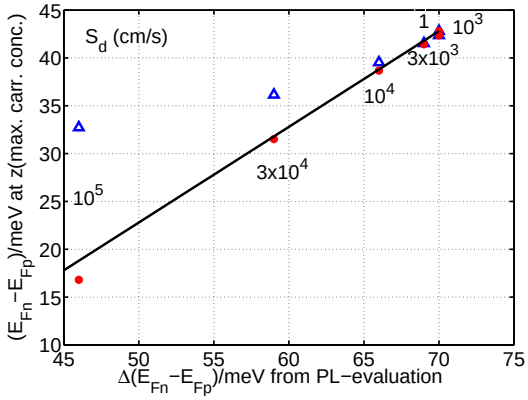

Figure 2.19.: Comparison of the splitting of quasi-Fermi levels calculated from the maximum excess carrier concentration and from the excess carrier concentration on the top of the absorber compared to the splitting of quasi-Fermi levels estimated from the PL yield for high photon energies.

but this equation can only be solved numerically, at least in general form. An analytic solution is possible for special ECLDPs $\tau(x)$.
The results in the following section are calculated using a **B**oundary **V**alue **P**roblem **S**olver (BVP6c) for Matlab [45].

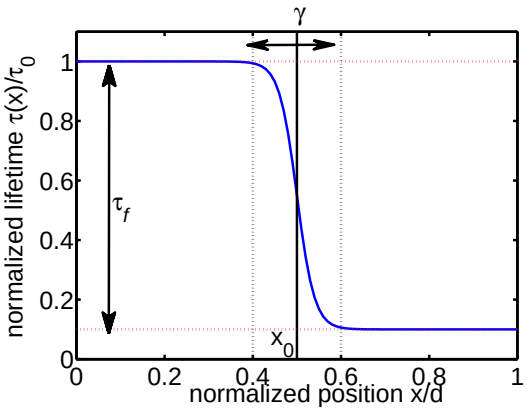

Figure 2.20.: Change of the excess carrier lifetime by defects in the top of the absorber with reduction of the lifetime τ_f, defect diffusion depth x_0 and decay area for the reduction of the lifetime from t_0 to $\tau_0 - \tau_f$.

2.3.2.1. Results of the PL with $\tau(x)$ in the excess carrier concentration

For the aim of this thesis it is not important to show a specified influence of the ECLDP on the emitted PL yield, but one of the main goals of the experimental part is to interpret and understand PL spectra. Thus a short survey of the influence of an ECLDP on the excess carrier concentration as well as on the emitted PL yield will be given. A more detailed discussion of results can be found in [46, 47].
The results of the simulation of different excess carrier lifetimes on the top of the absorber ($d = 2$ µm, $n_1 = 1.5$, $n_2 = 3.5$, $n_3 = 1$, $\tau_0 = 17$ ns, $D_c = 2.6$ cm^2/s, $S_0 = 10^5$ cm/s and $S_d = 100$ cm/s) are plotted in Fig. 2.21: different ECLDPs (left), resulting excess carrier concentrations (center) and resulting PL spectra for such excess carrier concentrations (right).
A direct impact of the reduction of the carrier lifetime is a lower excess carrier concentration due to stronger recombination, but additionally the shape of the excess carrier concentration is also varied. For high excess carrier lifetimes at the top of the absorber the carrier concentration decreases throughout the depth but for a low excess carrier lifetime at the top of the absorber the excess carrier concentration in the depth ($x \leq 0.5d$) is nearly constant.
The depiction of the PL spectra (Fig. 2.21 (right)) is normalized to show differences in the shape of the PL and not the impact of a reduced excess carrier concentration which results in a lower absolute PL yield. Here normalization means that the PL yield $\Gamma(E_{Ph})$ is divided by the integral of the PL yield for all photon energies between E_0 and E_1 with $E_0 < E_1$:

$$\Gamma_{\mathrm{norm}}(E_{Ph}) = \frac{\Gamma_{\mathrm{total}}(E_{Ph})}{E_1 - E_0} \frac{1}{\int_{E_0}^{E_1} \Gamma_{\mathrm{total}}(E_{Ph}) dE}. \tag{2.62}$$

These normalized PL yields are shifted to a higher photon energy with reduced lifetime τ_f but the maximum photon flux is always at a photon energy of $E_{Ph} = 1.04$ eV whereas the PL yields around a photon energy of $E_{Ph} = 1.5$ eV are influenced more strongly.
Thus the PL yields for photon energies above the photon energy of the maximum PL yield are reduced by an excess carrier depth profile. The other parameters of the ECLDP show a comparable influence on the emitted PL as discussed in [46, 47].
Due to the fact that the PL yield is nearly spectrally independent from the excess carrier lifetime, the integrated PL yield and the PL yield at $E_{Ph} = 1.4$ eV have nearly the same dependence on the splitting of quasi-Fermi levels calculated from the excess carrier concentration on the top of the absorber (compare Fig. 2.22).
So in this case there is not much difference in calculating the splitting of quasi-Fermi levels from the PL yield at high photon energies as described in chapter 2.1.1.2 or from the integrated PL. But the relation between the logarithm of the maximum PL and the splitting of quasi-Fermi levels from the excess carrier concentration is linear whereas the logarithm of the integrated PL cannot be described by a linear relation to the splitting of quasi-Fermi levels. So it is strongly recommended to calculate the splitting of quasi-Fermi levels from the spectrally resolved PL to minimize possible errors.

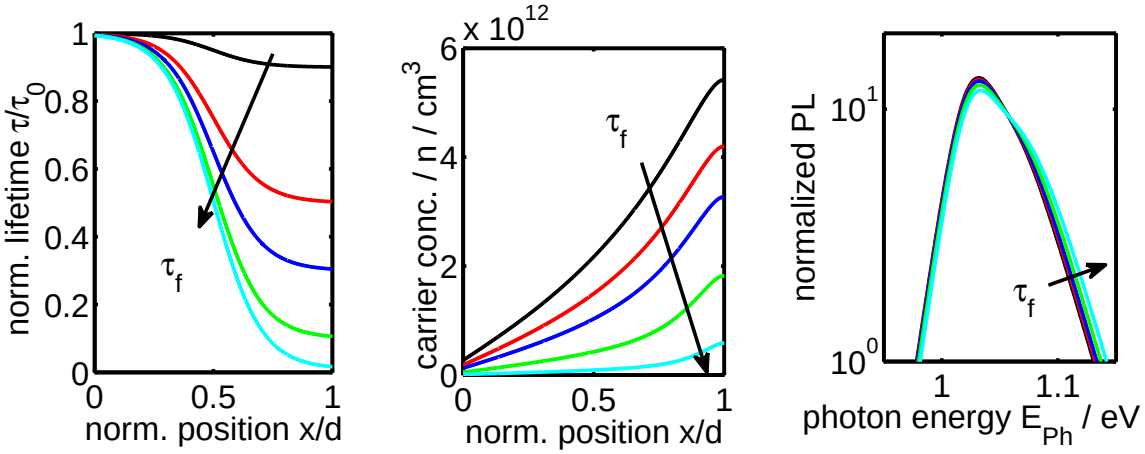

Figure 2.21.: Various excess carrier lifetimes for different reduced lifetimes at the top of the absorber τ_f (left), resulting excess carrier concentrations (center) and resulting normalized PL yields (right). The absolute PL yield is not plotted, because the absolute spectra differ in the same orders of magnitude as the excess carrier concentration and thus the small spectral differences are not observable.

2.3.3. Numerical solution of the continuity equation with $\tau(x)$ and $\alpha(x, E_{Ph})$

Not all absorber materials are as homogeneous as crystalline silicon, e. g. chalcopyrite absorbers like $Cu(In_{1-x}, Ga_x)(S, Se)_2$ show a depth dependent band-gap according to In and Ga concentrations [48, 49]. These materials are rather promising for thin film solar cells [50–52], because they offer low production costs but show adequate efficiencies. The properties of these materials

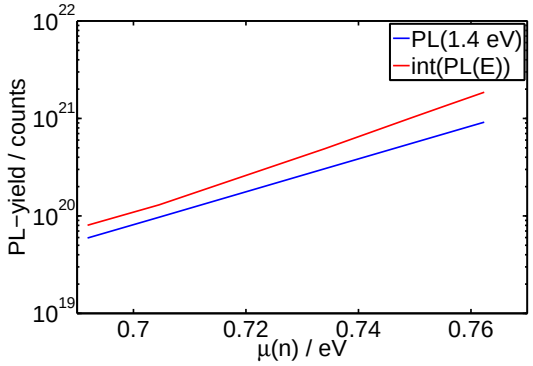

Figure 2.22.: Comparison of the numerically generated and integrated PL yield and the PL yield at $E_{Ph} = 1.4$ eV vs. the splitting of quasi-Fermi levels calculated from the excess carrier density at the top of the absorber.

are characterized with PL measurements [39, 53–55], so in order to understand PL results from such absorber materials, one needs to know the effect of a band-gap and absorption depth profile $\alpha(x, E_{Ph})$ on the emitted PL photon flux.
In what follows, a model to calculate the photon flux emitted from an excited absorber with depth dependent absorption coefficient $\alpha(x, E_{Ph})$ and a depth dependent lifetime $\tau(x)$ will be presented but only results of the influence of the depth dependent absorption will be given, as the influence of a depth dependent lifetime $\tau(x)$ on the PL yield has already been discussed above.
One effect of a depth dependent absorption coefficient is the following: the various kinds of absorption (absorption of the incident excitation light, reabsorption of the emitted PL photons) are not only given by the propagation length l of the radiation inside the absorber from one position x_1 to another position x_2 with $x_i \in [0, d]$ (this can be the absorption of the incident light on the way through the absorber with propagation length d from $x_1 = 0$ and $x_2 = d$ or e. g. the propagation of emitted PL radiation from emission position $x_1 = x$ to the surface $x_2 = d$ with propagation length $d - x$) but also by the positions x_1 and x_2.
For a constant absorption coefficient the absorption described above is given by[6]

$$A(E_{Ph}) = 1 - \exp(-l\alpha(E_{Ph})). \tag{2.63}$$

In the case of a depth dependent absorption coefficient, an integration over the absorption at every position of the propagation between x_1 to x_2 is needed, so that the total amount of absorbed light is given by

$$A(E_{Ph}) = 1 - \exp\left(-\int_{x_1}^{x_2} \alpha(E_{Ph}, x)dx\right). \tag{2.64}$$

Hence the differential equation for the excess carrier concentration is given by

$$-D_c\frac{d^2n(x)}{dx^2} + \frac{n(x)}{\tau_0} = G_0 \exp\left(-\alpha(x, E_{Ph})(x - d)\right), \tag{2.65}$$

[6]Note: The absorption depends only on the distance between x_1 and x_2 and not on the explicit positions of both points.

which can be solved with the same boundary problem solver which has been used before (see chapter 2.3.2). The emissivity $E(E_{Ph})$ is also changed by a depth dependent absorption coefficient, because both (emissivity and absorption coefficient) are connected due to Kirchhoff's law of thermal radiation. The influence of the absorption on the refractive index in the absorber given by the Kramers-Kronig relation is neglected, since the variation of the refractive index is negligible.

A simple model for the depth dependence of the absorption coefficient is assumed: The band-gap of the absorber is varied linearly from one surface of the absorber to the other and the absorption coefficient versus photon energy is shifted with this variation of the band-gap. This is illustrated in Fig. 2.23 (left), where a variation of the band-gap below zero ($\Delta E_G < 0$) shifts the spectral absorption coefficient towards small photon energies and vice versa. Note that due to the nonlinear shape of the absorption coefficient the absorption for low photon energies are varied stronger than for high photon energies.
The linear variation of the band-gap throughout the absorber for the following simulations is plotted in Fig. 2.23 (right).
This model is rather simple, because a change in In and Ga concentration would also lead to different spectral dependences of the absorption coefficient in the different absorber positions. But unfortunately there is no experimental data available on this effect.

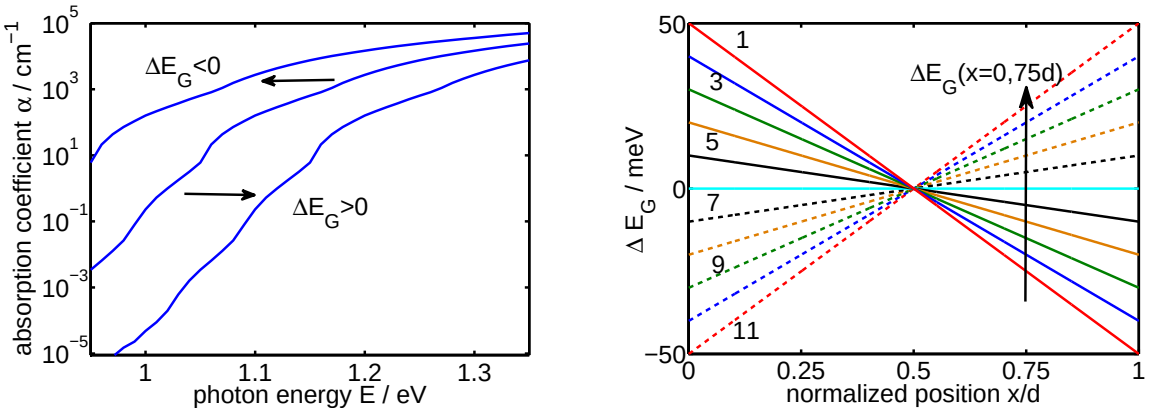

Figure 2.23.: Idealized effect of a variation in the band-gap (ΔE_G) on the absorption coefficient (left) and linear variation of the band-gap over the absorber depth characterized in this work (right).

2.3.3.1. Results of the PL for $\tau(x)$ and $\alpha(x, E)$

The discussion of the results is divided in two sections: The first section treats the PL emission with consideration of a constant excess carrier concentration through the depth of the absorber, the second one discusses the results with a depth dependent absorption coefficient included in the calculation of the excess carrier concentration.
A computation of the emitted PL for a constant excess carrier concentration ($n(x) = 10^{12}$ cm^{-1})

and with the absorption coefficients discussed above yields the PL spectra in Fig. 2.24 (left). Here the variation of the band-gap (equal if ascending or descending from bottom to top of the absorber) leads to a higher photon flux for small photon energies and the same photon flux for high photon energies. This equality is also illustrated in Fig. 2.24 (right), where the photon flux at $E_{Ph} = 1.05$ eV is plotted vs. the variation of the band-gap ΔE_G at $x = 0.75d$.
The reason for this behavior is simple: The excess carrier concentration in every absorber position is the same, so the quasi-Fermi level splitting in every absorber position is also the same, but the absorption coefficient is modified by the band-gap variation in such a way that $\Delta E_G < 0$ ($\Delta E_G > 0$) enhances (reduces) the absorption coefficient which enhances (reduces) the emission as well as the absorption, so both effects cancel each other.
But there is an enhanced photon flux for small photon energies, because the mean absorption coefficient of the absorber for small photon energies is enhanced for both kinds of band-gap variation, thus more photons with a small photon energy are emitted due to a higher emission.

Fig. 2.25 (left) shows the excess carrier concentration for the excitation from the top of the absorber with consideration of the different absorption coefficients given by the band-gap variations in Fig. 2.23 (right). For an increase in the band-gap on the top of the absorber, the absorption coefficient is reduced and thus the excess carrier concentration near the surface is also reduced because of the lower absorption of the excitation laser. The influence of the different absorption coefficients on the excess carrier concentration at the bottom of the absorber is negligible, because there the excess carrier concentration is mainly governed by carrier diffusion. These excess carrier concentrations break the "symmetry behavior" between absorptivity and emissivity between the different absorber positions as discussed before, so that a band-gap decay from top to bottom leads to a different PL photon flux than a rise. This is illustrated in Fig. 2.25 (right).
When the band-gap at the top of the absorber is higher than at the bottom (dotted line), the spectral PL for small photon energies is increased because in the top regime of the absorber a high electron concentration occurs and consequently creates high rates of radiative recombination. Moreover, the emitted photons show a low probability of absorption in the top regime with its corresponding high band-gaps.
For the opposite case, the absorption for photons in the top of the absorber is enhanced by a decrease in band-gap, in particular high energy PL photons on the way to the surface are attenuated. In this case photons emitted deep in the absorber (e. g. $x/d \leq 0.5$) can not compensate the reduction because the excess carrier concentration here is too small to have a strong impact on the emitted PL.
It is important to note that the impact on higher photon energies is very small, so that the estimation of the quasi-Fermi level splitting [56] from Planck's generalized law via the high photon energy wing is not remarkably affected.

Fig. 2.26 shows the results of a study on how the depth dependent excess carrier concentration influences the PL yield and particularly its high energy wing which is commonly used for

the determination of the splitting of quasi-Fermi levels μ. From numerically accurately available excess carrier concentrations exemplarily taken from data in Fig. 2.25 (left) at maximum density versus depth the according maximum splitting μ_{max} is derived. In dependence of this formally exact magnitude, the behavior of the high photon energy PL yield (here $\Gamma_{\text{total}}(1.4\text{ eV})$), generally used for e. g. $\mu \propto k_B T \log \Gamma_{\text{total}}(1.4\text{ eV})$, and the trend of the entire PL yield

$$int(PL) = \frac{1}{1.3\text{ eV} - 1\text{ eV}} \int_{1\text{ eV}}^{1.3\text{ eV}} \Gamma_{\text{total}}(E_{Ph}) \tag{2.66}$$

are plotted in Fig. 2.26. This has sometimes be misinterpreted as an indication of the quality of the absorber properties and its photoexcited state. It must be emphasized, that even the integrated PL e. g. used in [57] can only be reproduced numerically with consideration of the depth dependent absorption.

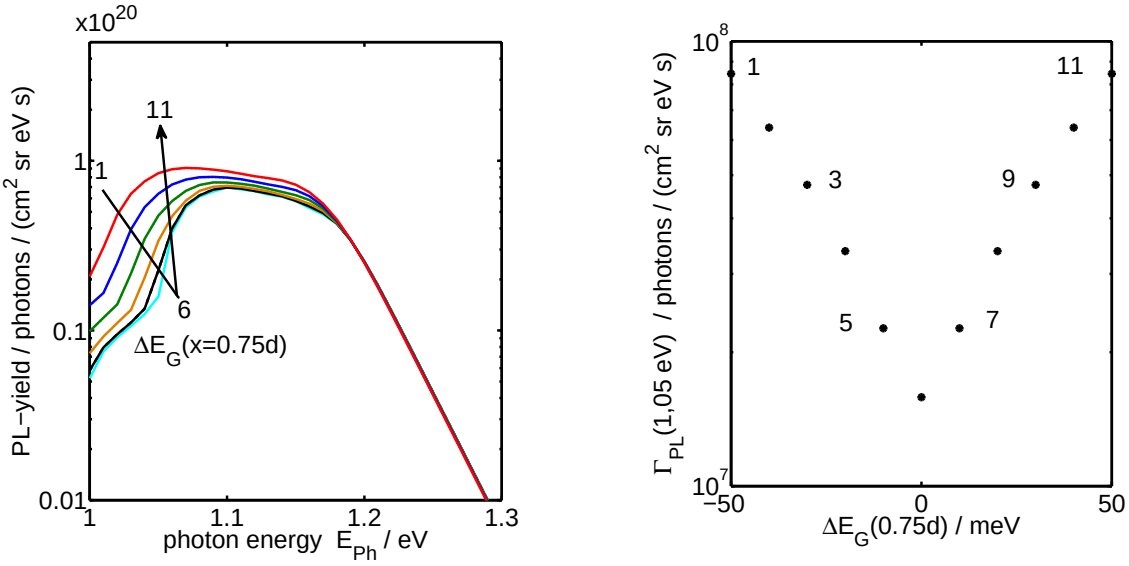

Figure 2.24.: PL photon flux for a constant excess carrier concentration ($n(x) = 1 \cdot 10^{12}$ /cm^3) with the different absorptions given by the band-gap variation in Fig. 2.23 (left) and illustration of the PL yield at $E_{Ph} = 1.05$ eV over the band-gap variation at $x = 0.75d$ (right).

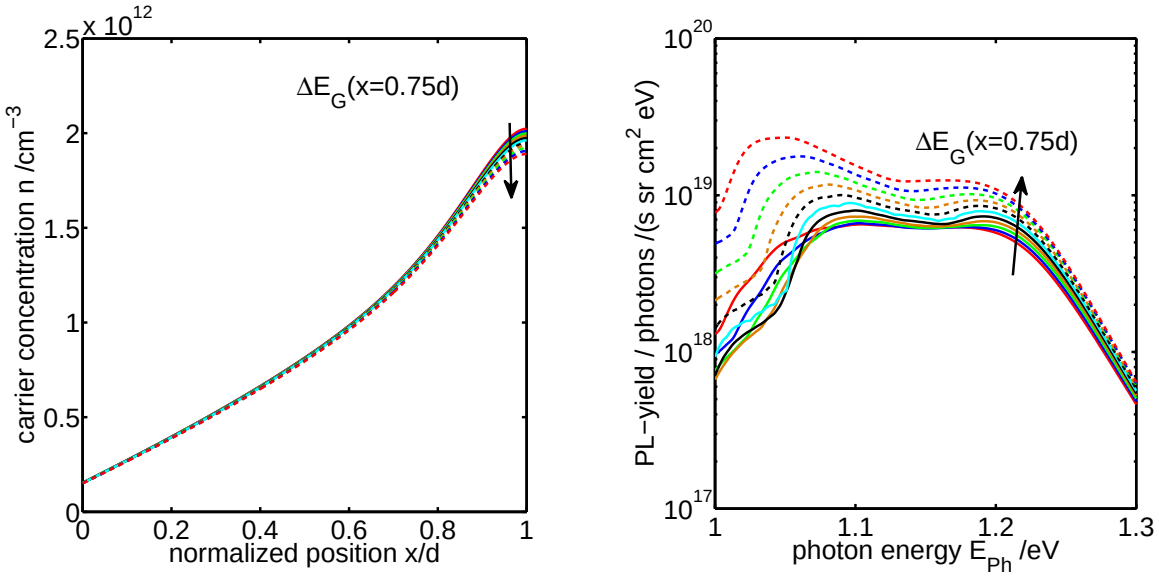

Figure 2.25.: Excess carrier concentration (left) for the absorption coefficients given by the band-gaps in Fig. 2.23 (right) and the resulting PL yields (right).

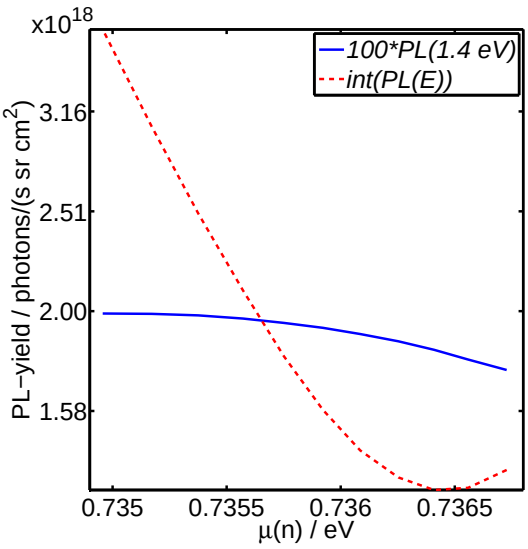

Figure 2.26.: Influence of the integrated PL yield and the PL yield for $E_{Ph} = 1.4$ eV on the quasi-Fermi level splitting calculated from the excess carrier concentration. No quasi-linear behavior can be observed anymore.

3. Experimental setups and samples

In this chapter a short description of the experimental setups and samples used in this work will be given. It shall only present an overview and no detailed information about the setups.

3.1. Angular dependent PL

The experimental setup to measure the angular dependent PL emission of an excited absorber is drafted in Fig. 3.1: on the right the excitation system, in the center a rotation stage system with sample holder and on the left the detection system.
The excitation system contains a laser (488 nm Ar^+-ion laser), a laser line filter[1] to suppress the lines of the excited gas in the laser, a polarizer to ensure that the excitation is s-polarized, a circular aperture with a diameter of $d = 1.1$ mm and a diffuser[2] which can be flipped into the optical beam path to get a homogeneous excitation over the entire sample, e. g. for the homogeneous excitation of a fluco.
To be able to vary both, the angle of excitation and the angle of detection, the sample holder is positioned on a double rotation stage, so that both angles can be varied independently. The sample holders described below are positioned in a third rotation stage, which gives the possibility to rotate the sample with the rotation axis on the optical axis of excitation and detection.
It is very important that the axis of rotation of the excitation and detection lies in the surface of the absorber as illustrated in Fig. 3.2 (left). Otherwise the excited or detected area of the absorber varies with the excitation/detection angle, which would lead to different detector signals not caused by a different excitation/emission angle but due to different sample positions.
In this case the PL radiation is collected with a collimator and coupled via a glass fiber into the optical multichannel analyzer (OMA) composed of a 0.5 m spectrograph with different gratings and a liquid nitrogen cooled InGaAs detector array with 1024 pixels.
The angular resolution of this setup is given by the distance between the surface of the sample and the collimator in combination with the width of the collimator where radiation is coupled into the glass fiber. For the used hardware, the angular resolution is $(1.47 \pm 0.15)°$. It could be enhanced by using a longer detector arm, which would extend the distance between the collimator and the sample is larger.
Two kinds of sample holders are illustrated in Fig. 3.2 (center) and (right): The first holder is used to measure the edge emission of a fluco and the second one to measure the emission from the top of an absorber with excitation on the opposite side.

[1] Thorlabs FL488-10.
[2] Thorlabs ED1-S20.

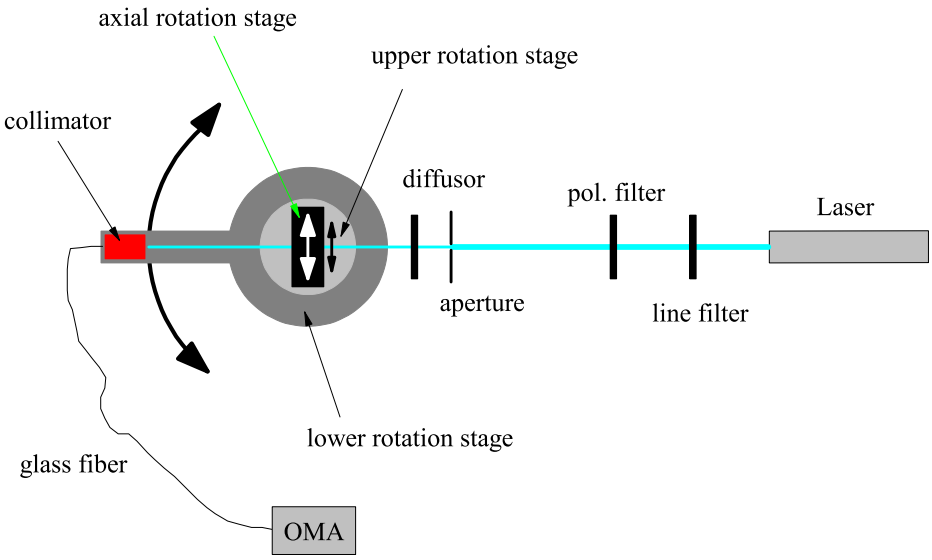

Figure 3.1.: Sketch of the experimental setup for PL measurements with angular dependent detection (lower rotation stage) and/or angular dependent excitation (upper rotation stage) for different absorber materials like c-Si or flucos. This setup also provides a rotation stage for the rotation of the sample around the axis of excitation. The excitation is done with a 488 nm laser and filtered by a bandpass filter and polarization filter. The emitted radiation from the absorber is collected by a collimator and coupled into an optical multichannel analyzer by a glass fiber.

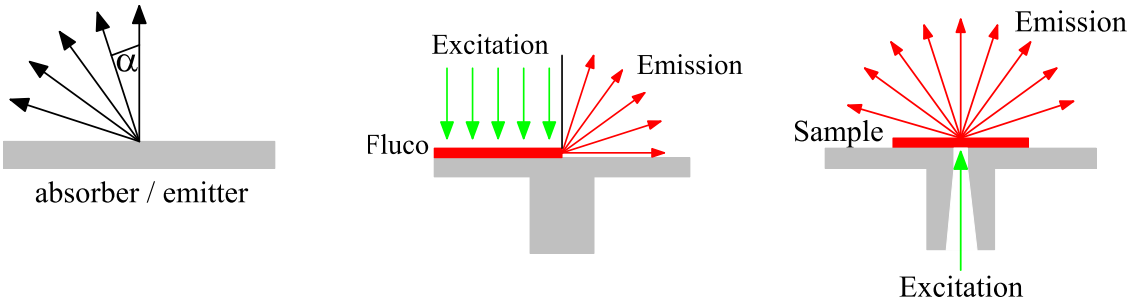

Figure 3.2.: Illustration of how the axis of rotation should always be on the top of the absorber/emitter (left), sketch of the sample holder for the detection of the edge emission with mount and shield to exclude the unwanted edge emission (center) and sample holder for the detection of the top/bottom emission (right).

3.1.1. Calibration

There different calibrations of the setup were performed as discussed in appendix B: wavelength calibration, relative callibration and absolute calibration.

3.2. Scattering

The experimental setup to measure the electro-magnetic radiation scattered on an illuminated sample is sketched in Fig. 3.3. The sources of radiation are different lasers (HeNe with 543 nm and 632.8 nm and a laser diode with 1112 nm) which hit (chopped by a chopper (CP)) the sample mounted in (S) on the rotation stage (red). This rotation stage has an arm with a photo diode[3] (PD) mounted on it and a holder where a neutral density filter (NDF) can be positioned in front of the photo diode to control the photon flux of the radiation hitting the photo diode. The rotation stage is moved by a motor (M) which can be controlled via a computer (PC), the chopper is controlled via a frequency controller (F). The computer also collects the photo current of the photo diode via a lock-in amplifier (L) which provides access to the scattered photon flux. With this setup the radiation scattered by the sample both in transmission and reflection is recorded, depending on the position of the detector arm for a variable angle of incident of the illumination.

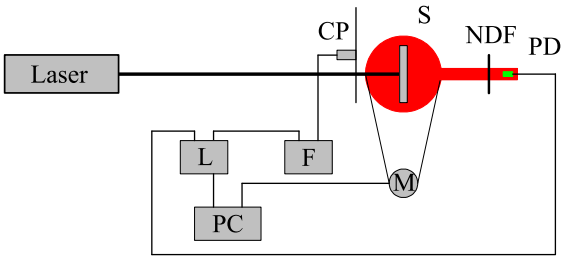

Figure 3.3.: Experimental setup to measure the scattering from a sample mounted in S in reflection or transmission with sample holder S, neutral density filter NDF, photo diode PD, frequency controller F and chopper CP, lock-in-amplifier L, motor M and a computer PC.

3.3. Fluco edge emission

Another possibility to measure the edge emission of an excited fluco as with the angular dependent PL is to couple a photo diode on the edge of the fluco like [41, 58]. In this method the

[3]BPX 61.

space between the edge of the fluco and the photo diode should be filled with a refractive index matching gel to attain a good optical connection.
Fig. 3.4 shows a sketch of this kind of setup used in this thesis: A photo diode[4] with the size of the fluco edge is integrated in a black sample holder and the fluco can be slid into this holder. This setup can be positioned on a scattering back reflector (e. g. bleached cellulose) or on an absorbing material (e. g. blackened brass).
The source for excitation is a high power LED with wavelength that matches the absorption of the fluco (in the case of Rodamin 6 G and Lumogen F rot 305: $\lambda = 505$ nm). The sample holder is high enough so that a photonic structure can be placed on top of the fluco with a spacer in between. These spacers between photonic structure and fluco are of great importance as will be discussed in chapter 4.4.2.2.

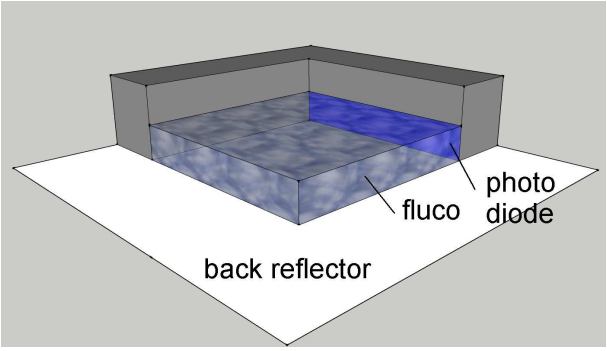

Figure 3.4.: Sketch of the setup to measure the edge emission of a fluco with a photo diode.

3.4. Additional Setups

The other experimental setups used for this work are either commercially available or rather simple so they will only be described roughly.

3.4.1. Reflection and Transmission

Most reflection and transmission measurements in this thesis are performed with a Cary 5E from Varian [59]. Measurements of the diffuse transmission and reflection are performed with the "Diffuse Reflectance Accessory", measurements of the direct transmission with a sample holder, measurements of the direct reflection with the "Absolute Specular Reflectance Accessory" and measurements of the angular dependent reflectance with the "Variable Angle Specular Reflectance Accessory".

3.4.2. AFM

All AFM measurements in this work where performed with the commercially available cantilever AFM "alphasnom" from Witec [60] (lateral resolution: about 8 nm, depth resolution: about 1

[4]SLSD-71N400.

nm).

3.4.3. Laterally resolved PL

The experimental results for the characterization of the lateral homogeneity of the emitted PL are obtained with three different setups depending on the lateral size of the inhomogeneities of the sample:

- one for the characterization of inhomogeneities in the mm-scale with a setup called Makro-PL;
- one for the characterization in the µm-scale with a setup called Micro-PL;
- and a SNOM (**s**canning **n**ear-field **o**ptical **m**icroscope) for even smaller scales.

Each of them have the same principle setup: An excitation laser is focused on the sample and the emitted radiation is collected and coupled into a glass fiber which guides the radiation to the OMA already mentioned in chapter 3.1.

3.4.3.1. Makro-PL

The laterally resolved PL setup with a resolution in the mm-range is composed of an excitation laser (Ar-Ion, 488 nm) with a photon flux of ca. $(2.92 \pm 0.13) \cdot 10^{17}$ photons $s^{-1}cm^{-2}$ focused on a spot on the sample with a diameter $d = 1.1$ mm and a collimator which couples the radiation into a glass fiber.

3.4.3.2. Micro-PL

In the Micro-PL setup the excitation laser is focused with a microscope objective onto the sample with a spot size of ca. $A \approx 1$ µm^2 and the emitted radiation is also collected through this microscope objective and coupled into a glass fiber via a beam splitter which "separates" the beam path of the excitation and collection.

3.4.3.3. SNOM

The "alphasnom" (WITec GmbH) is also able to perform SNOM measurements. This is a cantilever based SNOM where the cantilever tip is a pyramid with an opening on the top of around $d = 100$ nm or $d = 200$ nm diameter. The excitation is focused on the tip of the cantilever and the emission is measured in transmission through the sample. The detector system is the same as in chapter 3.1.

3.5. Samples

3.5.1. Crystalline silicon

One absorber used in this work is a p-type crystalline silicon (c-Si) wafer. This wafer is approximately $d = 250$ µm thick, on both sides polished and on both sides PCVD passivated with silicon nitride (SiC_X). Other informations of the wafer provided by the preparator are summarized in Tab. 3.1.
The wafer was provided by the ISE (Fraunhofer Institut für Solare Energiesysteme) Freiburg.

Table 3.1.: Properties of the c-Si wafer.

Passivation	PECVD SiC_X
Resistivity	1 Ωcm
Surface recombination velocity	$S_{\text{eff}} < 20$ cm/s

3.5.2. Fluorescence solar collector

The flucos used for this work are solid with the fluorescence dye (Rhodamin 6G or Coumarin 540a) in **P**oly**m**ethyl**m**eth**a**crylat (PMMA) on top of a glass substrate ([61]) or PMMA flucos with homogeneous dye (LUMOGEN F ROT 305) concentration (as illustrated in Fig. 3.5). The flucos on glass where produced by Nazila Soleimani at the university of Southampton and the PMMA flucos by an unknown French company.
All flucos have approximately the same size of $(25 \times 25 \times 1)$ mm^3 and have a rather flat surface in order to reduce scattering effects, and the dye concentrations vary within a broad range (e.g. 0.3 g/l and 0.8 g/l for LUMOGEN F ROT 305).

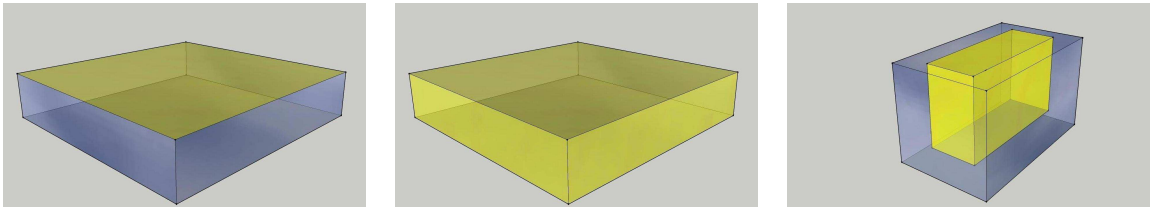

Figure 3.5.: Different realizations of flucos. Glass substrate with fluorescence dye in PMMA on top (left), a full PMMA fluco with homogeneous dye concentration (center) and a cuvette with a solution containing a fluorescence dye (right).

3.5.3. Photonic structures

The fundamental principle of photonic crystals is the variation of the refractive index throughout the photonic crystal so that the propagation of light with a specified wavelength is prohibited [62,63]. To this end there are three different kinds of photonic crystal possible, as illustrated in Fig. 3.6. They are specified by the number of dimensions in which the refractive index is

varied.
The simplest photonic structure is given by the variation of the refractive index in one dimension by alternating layers of different refractive index. A 1d photonic crystal can only prohibit the propagation of light in the direction in which the refractive index is varied.
For this reason a 3d photonic crystal with a varying refractive index in three dimensions has a so-called full stopgap at a specified wavelength which prohibits the propagation of light with this wavelength through the photonic crystal in all directions and thus reflects back all incident light with this wavelength.

All three kinds of photonic crystals have lately been discussed in the literature for varioust applications e. g. [64, 65].
In this work a one-dimensional photonic crystal in the shape of a Bragg-mirror and a three-dimensional photonic crystal in the shape of an opal have been used.

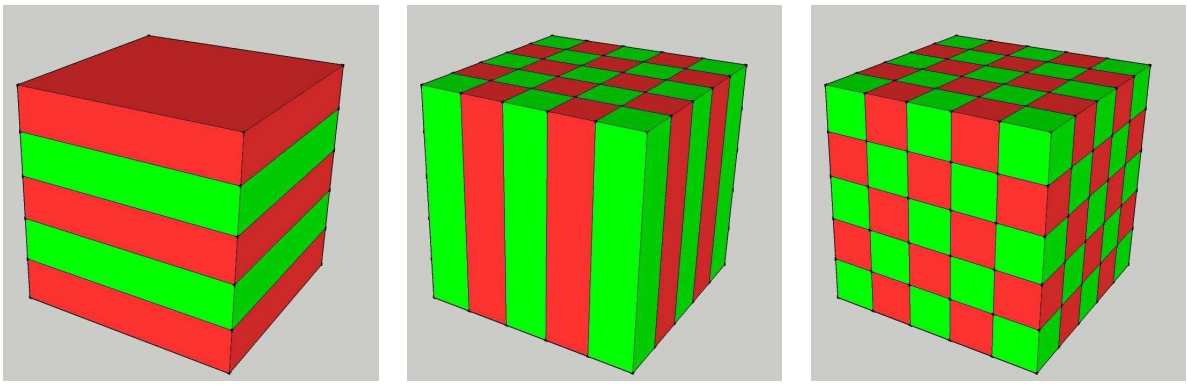

Figure 3.6.: Sketch of a 1d (left), 2d (center) and 3d (right) photonic crystal.

3.5.3.1. Bragg-mirror

A Bragg-mirror, Bragg stack or Bragg grating is the simplest example for a 1d photonic crystal, because it consists of a stack of layers with two different refractive indices n_1 and n_2 with the thickness d_1 and d_2 as depicted in Fig. 3.7 (left). The reflection on such a Bragg-mirror is plotted in Fig. 3.7 (right) for the parameters in Tab. 3.2. N is the number of double layers with two refractive indices.
The calculation of the reflection was done with the equations from [66] and shows the known reflection for a certain wavelength regime up to 100% and a very low reflection for other wavelengths.
This fundamental method to stack layers with materials of different refractive index is used for many interference filters like bandpass, lowpass or other filters. One of the more complex filters based on this principle is the so-called Rugate filter [67] which uses many ($N \gg 10$) layers of different refractive indices.
Such filters have the advantages of high optical quality (high transmission or reflection depend-

ing on the wavelengths, laterally homogeneous) and the possibility to design the filter for most spectral demands, but they can be rather expensive due to the high number of different layers needed (see e. g. in [67]), and an angular selectivity as in Fig. 1.3 is not achievable with such simple photonic structures.

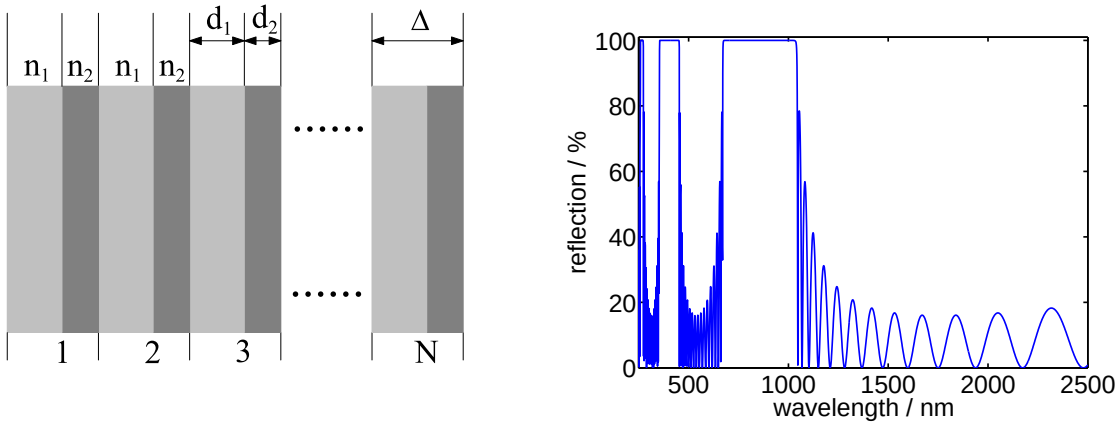

Figure 3.7.: Sketch of a Bragg-mirror with a stack of materials with refractive indices n_1 and n_2 and thicknesses d_1 and d_2 (left) as well as simulation of the reflection on such a Bragg-mirror (right).

Table 3.2.: Parameter for the simulation of the Bragg-mirror.

Parameter	Value
n_1	1.5
n_2	3.5
d_1	80 nm
d_2	80 nm
N	20

3.5.3.2. Opal

One of those 3d photonic crystal which are easiest to produce is the opal, which is composed of nanospheres of diameter D which are packed in a fcc (**f**ace **c**entered **c**ubic) lattice[5]. This type of photonic crystal has the advantage of having a stopgap which scales with the diameter of the PMMA nanospheres. The stopgap of the opal with PMMA nanospheres with a refractive index of $n_{\mathrm{PMMA}} = 1.5$ and air in the holes between the spheres with a refractive index of $n_{\mathrm{air}} = 1$ is given by

$$\lambda_{\mathrm{stop}} = \frac{a}{0.658} \tag{3.1}$$

[5]The opal shows no complete photonic band gap, which is e.g. observable in an inverse opal. But such an inverse opal needs a refractive index of about 3, so the inverse opal would not be transparent for the incident solar radiation.

with the lattice constant $a = \sqrt{2}D$. This can be derived from the photonic band diagram plotted in Fig. 3.8 (left) for the crystal orientations of the first Brillouin zone (right), which can be calculated with e. g. MPB (**M**IT **P**hotonic-**B**ands) [68] or Lumerical FDTD Solutions [69]. The band diagram shows a photonic band-gap for a $\Gamma - \mathrm{L}$-crystal orientation, which is called stopgap, because the propagation of electro-magnetic radiation with a wavelength in the band-gap of the photonic crystal is forbidden to propagate in the photonic crystal and thus is stopped and reflected back. The surface of an opal with $D = 540$ nm PMMA spheres is depicted in Fig. 3.9.

A fcc lattice has a filling factor of

$$f = \frac{\pi}{3\sqrt{2}} \approx 0.740 \tag{3.2}$$

and thus the effective refractive index of the opal layer is

$$n = f \cdot n_{\mathrm{sample}} + (1 - f) \cdot n_{\mathrm{air}} = 1.37, \tag{3.3}$$

which is between the refractive index of the samples (glass $n_{\mathrm{sample}} = 1.5$, crystalline silicon $n_{\mathrm{sample}} = 3.5$) and that of air $n_{\mathrm{air}} = 1$.

This additional layer of the opal with refractive index $n = 1.37$ influences the emission and excitation through this layer. In the following the influence of the transmission of electro-magnetic radiation from a $d = 250$ µm thick crystalline silicon wafer through a 3.7 µm thick layer of refractive index $n = 1.37$ (meaning the effective refractive index of an opal with approximately 10 layers of $D = 540$ nm PMMA spheres) for s- and p-polarized radiation as well as the transmission without the additional layer and the transmission in the opposite direction from air to c-Si absorber will be introduced.

Fig. 3.10 shows the refractive index for this simulation: A layer of refractive index $n = 3.5$ for silicon, then a layer of refractive index $n = 1$ for air (in the case of direct emission from the silicon) and an additional layer with refractive index of $n = 1.37$ for the emission through the opal. Here the inner structure of the opal is neglected.

The angular dependent emission is given by Fresnel's equations (eq. 2.37) and the phase factor for the respective wavelength and propagation length. In this case, the absorption inside the opal as well as inside the silicon is neglected.

Results for the angular and spectral dependent transmission from inside the crystalline silicon to the air without opal layer are plotted in Fig. 3.11 for s- and p-polarized radiation and with opal layer in Fig. 3.12. The direct emission for s-polarized radiation shows a reduction of the transmission with increasing emission angle and no wavelength dependence. The same can also be observed for the p-polarized light, but here the transmission from silicon to air increases with the emission angle up to the Brewster angle where transmission is perfect; for even higher emission angles it is reduced again.

Comparably thick Silicon with an additional layer of refractive index $n = 1.37$ shows a wavelength dependent transmission with interferences, which result from interferences inside the 3.7 µm thick layer of $n = 1.37$.

This result is not valid for a real opal layer, because the opal has no flat surface which is needed

for interferences, but it should be kept in mind, that an additional layer of a different refractive index influences the transmission. Thus, to reduce this effect (and to be able to neglect the inhomogeneity of the crystalline silicon (chapter 4.2.4)) in measurements, the comparison of the emission with and without opal is done for the transmission from silicon to air through glass with opal on top, and from silicon through glass.
The transmission for the inverse direction from air to c-Si with and without additional layer of refractive index $n = 1.37$ is plotted in Fig. 3.13 for s-polarized light and normal incidence. Applying such a layer on top of c-Si shows the properties of an anti-reflective coating, because the transmission into the c-Si absorber is enhanced up to 31%, depending on the wavelength.

A way to calculate the transmission through an opal and the reflection on an opal is described in [70]. Fig. 3.14, 3.15 and 3.16 show results calculated with a program based on this literature for an opal with $D = 540$ nm PMMA spheres with different numbers of layers, different angles of incidence and a rotation of the sample around the axis of excitation. The program has been provided by J. Üpping from MLU Halle.
The transmission through the opal with different number of layers with PMMA nanospheres of $D = 540$ nm diameter (Fig. 3.14) clearly shows a reduction in the transmission around $\lambda = 1200$ nm, which is the wavelength of the stopgap for this opal. Here the transmission does not vary if more than ten layers of spheres are simulated. Thus it should be good to have at least ten layers.
The calculation includes two different angles: the angle of incidence, i. e. the angle between normal incidence and the angle of excitation (from 0° to 90°), and the orientation of the opal around the axis of the incident radiation (from 0° to 360°). The first one is called the tilting angle and the second one the angle of rotation. Results of the transmission and reflection for an opal for different tilting angles are plotted in Fig. 3.15. Here one can observe a shift of the stopgap to lower wavelengths with increasing tilting angle which results from the Bragg effect and will be explained in chapter 4.1.2. There are also higher orders of the stopgap observable in the transmission and reflection and a reduced transmission for lower wavelengths. This is a disadvantage of the opal, namely photons with a low photon energy are also influenced by the opal.
Fig. 3.16 shows the transmission and reflection for an opal with ten layers of $D = 540$ nm PMMA nanospheres for a tilting angle of 30° and a rotation angle of the opal between 0° and 360°. Here a shifting of the stopgap is observable as well as the low transmission for $\lambda \leq 600$ nm.
Another possibility to calculate the transmission through an opal is a FDTD (**f**inite-**d**ifference **t**ime-**d**omain) algorithm. The result of the transmission through an opal of ten layers of $D = 540$ nm sphere with such a commercial algorithm [69] is plotted in Fig. 3.17. Here the reduced transmission around $\lambda = 1200$ nm is observable, but the transmission for small wavelengths below $\lambda \leq 600$ nm is very low. This would result in a reflection of much radiation in a solar cell, if the opal were attached to the top the absorber.
The results for an opal with other sphere diameters should equal these results, since the optical properties are scaled linear with the sphere diameter, so results for an opal with $D = 270$ nm

PMMA spheres will not be shown.

The production of an opal is rather simple: PMMA nanospheres in a solution with e. g. water are either spin- or dip/edge-coated on the substrate. Afterwards the opal can be heated to connect the PMMA nanospheres to each other in order to get a more stable structure. The opals for this work were prepared by J. Üpping at MLU Halle and literature about the preparation of opals can be found e. g. in [71–74].
One possibility to influence the position of the stopgap apart from the sphere diameter is to vary the refractive index of the spheres and that of the holes between the spheres. To this end the holes between the nanospheres can be filled with a material with high refractive index and the nanospheres can be etched out as described e. g. in [75].
All these results are for an opal in $\Gamma - \mathrm{L}$ direction, so the stopgap is in the direction of the transmission under normal incidence. As mentioned in the introduction, the aim is to put a photonic crystal on top of a solar cell in order to prevent the radiation from escaping the absorber for nearly all angles without influencing the incident radiation from the sun. This can be achieved by using an opal in $\Gamma - \mathrm{X}$ direction. But unfortunately no opal sample with this crystal orientation was available, since the production of such a crystal is much more complicated [76].
The wavelength and angular dependent transmission of an opal in $\Gamma - \mathrm{X}$ direction is plotted in Fig. 3.18. Here the radiation with an angle of incident below 10° is not influenced by the opal.

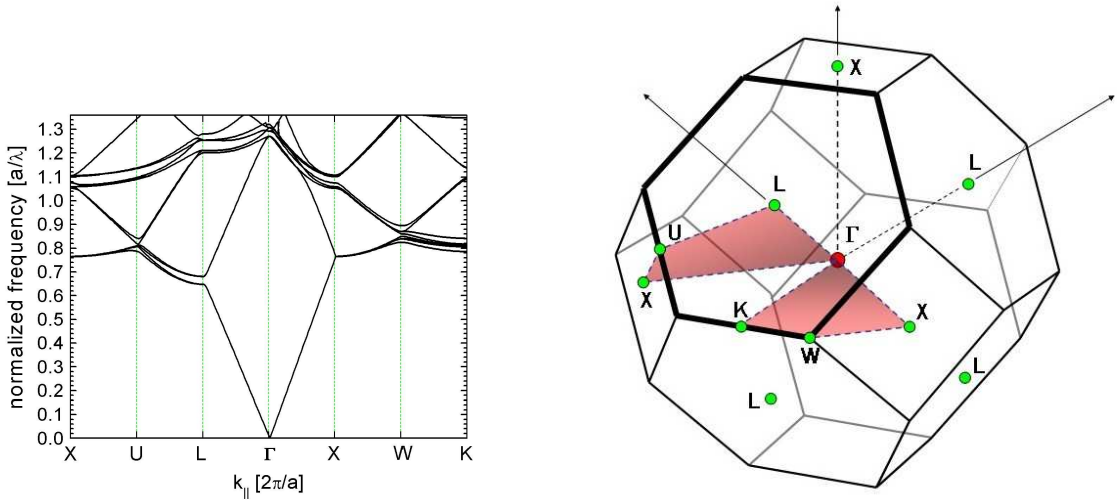

Figure 3.8.: Banddiagramm (calculated with mpb [68]) of an opal for different crystal orientations (left) and an illustration of these crystal orientations (right) of the first Brillouin zone. Provided by Andreas Billawny at MLU Halle.

3.6. Refractive Index matching

The experiments in chapter 4 often contain the attachment of a glass substrate on a sample, e. g. a photonic structure on a glass substrate with refractive index $n_{\mathrm{glass}} = 1.5$ on a c-Si wafer

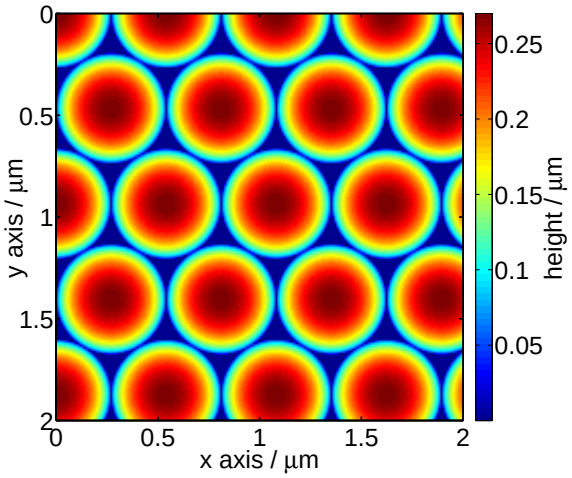

Figure 3.9.: Surface of an idealized opal in $\Gamma - \mathrm{L}$ direction.

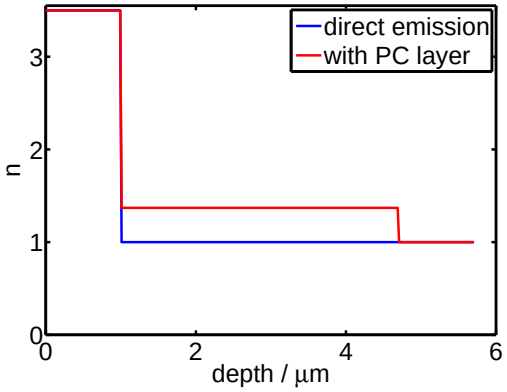

Figure 3.10.: Refractive index for the simulation of the transmission from crystalline silicon into air with and without additional photonic crystal layer on top of the silicon.

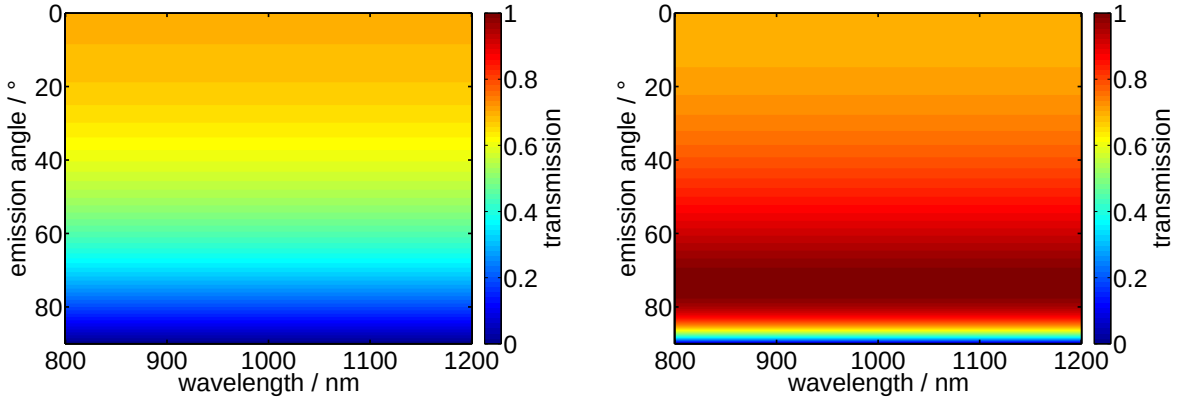

Figure 3.11.: Transmission from silicon to air for s- (left) and p-polarized (right) electro-magnetic radiation without additional layer on top of the silicon.

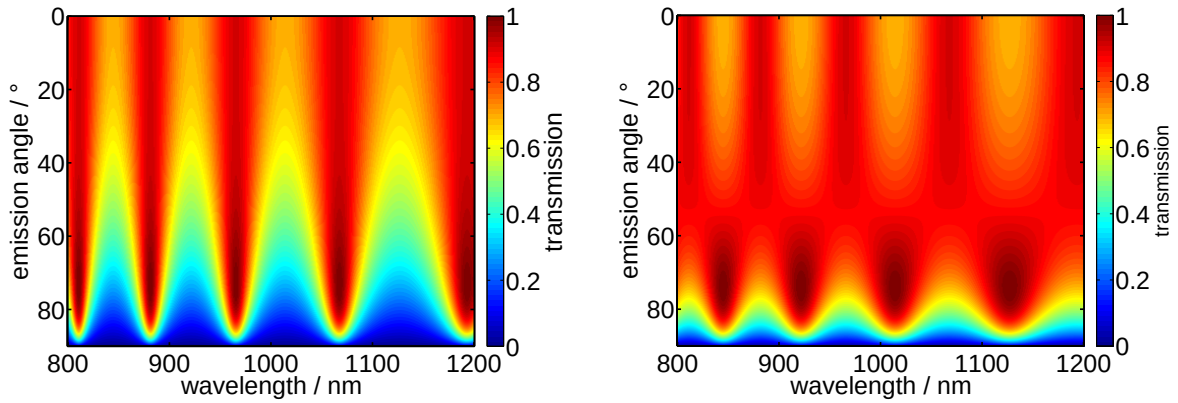

Figure 3.12.: Transmission from silicon to air for s- (left) and p-polarized (right) electro-magnetic radiation with additional layer of refractive index $n = 1.37$ and $d = 3.7$ µm thickness on top of the silicon.

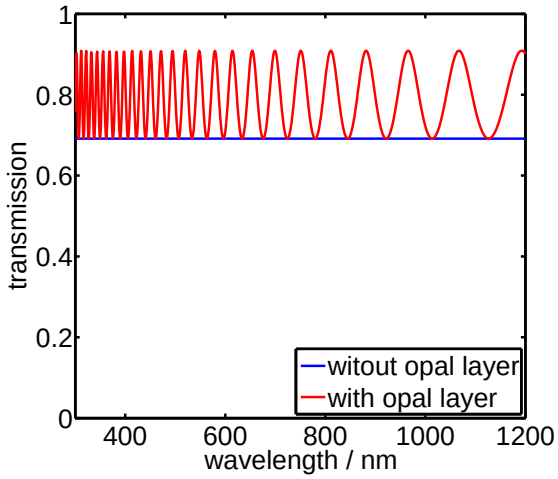

Figure 3.13.: Transmission from air to c-Si in comparison to the transmission from air through a $d = 3.7$ µm thick layer with refractive index $n = 1.37$ for s-polarized radiation.

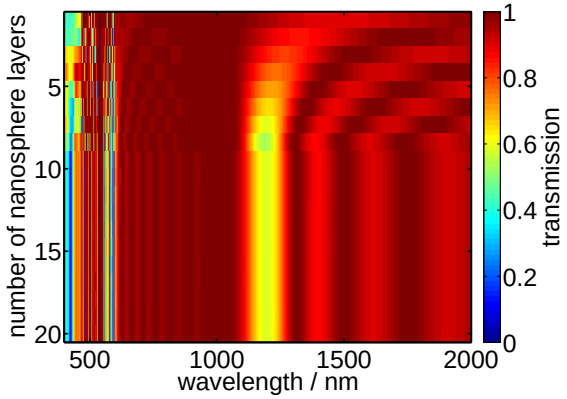

Figure 3.14.: Simulated transmission through an opal with different numbers of layers of $D = 540$ nm PMMA spheres.

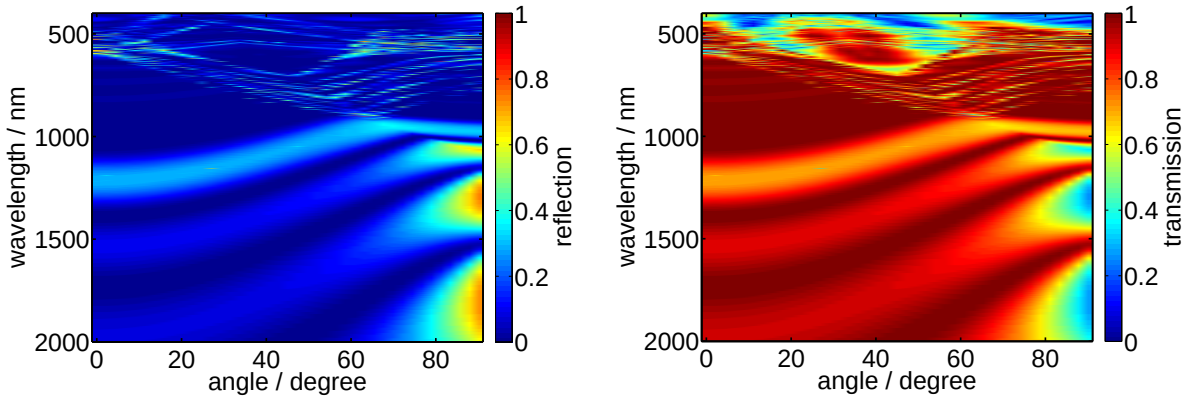

Figure 3.15.: Reflexion on (left) and transmission through (right) an opal with ten layers of $D = 540$ nm PMMA spheres for different tilting angles.

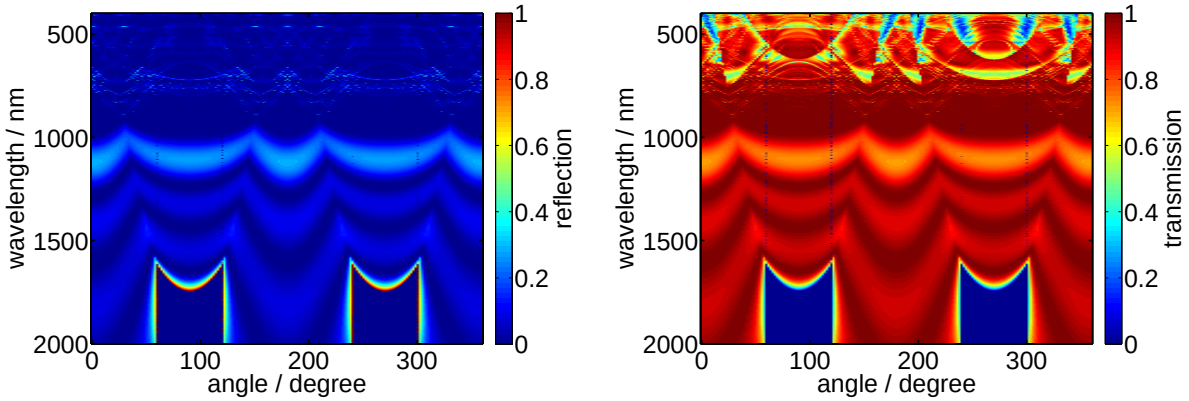

Figure 3.16.: Reflexion on (left) and transmission through (right) an opal with ten layers of $D = 540$ nm PMMA spheres for a tilting angle of 30° and a rotation of the sample around the axis of excitation.

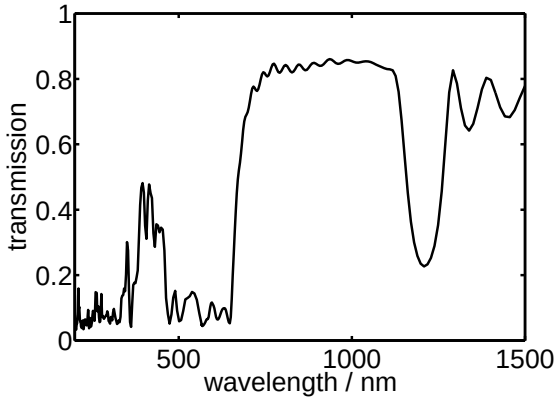

Figure 3.17.: Transmission in $\Gamma - \mathrm{L}$ direction through a ten layer opal of $D = 540$ nm PMMA nanospheres calculated with a FDTD algorithm.

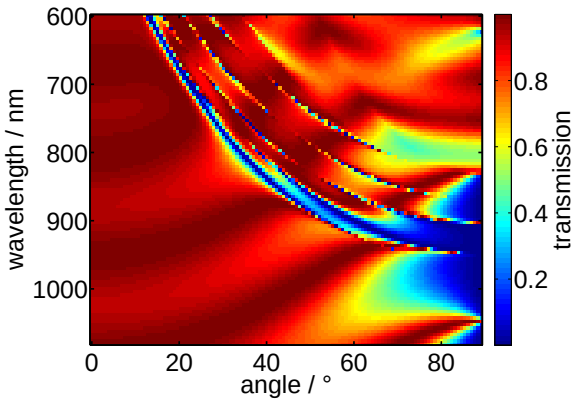

Figure 3.18.: Angularly resolved transmission in $\Gamma - X$ direction through a ten layer opal of $D = 540$ nm PMMA nanospheres. Provided by J. Üpping from MLU Halle.

with refractive index $n_{\mathrm{cSi}} = 3.5$[6]. A matching of these refractive indices is needed to reduce reflection losses and to make it easier to compare different results by neglecting the effect of this additional step (absorber, air, glass substrate) in the refractive index.

Transmission measurements are a possibility to analyze different materials as a refractive index matching medium. A sketch of the measurements is plotted in Fig. 3.19. The transmission of a thin index matching medium is measured by squeezing a little drop of the medium between two clean glass substrates and measuring the transmission of the electro-magnetic wave under normal incidence.

Results of such a measurement for different media like air, distilled water, oil of a turbo molecular pump and index matching gel from ThorLabs[7] are depicted in Fig. 3.20. In the optical regime of $500 \text{ nm} \leq \lambda \leq 1300$ nm (including the excitation wavelength of the setups and the emission of the fluorescence collectors and c-Si) the transmission through all tested media is rather constant (apart from the steps at $\lambda = 800$ nm for the detector changeover) but the index matching gel has the highest transmission and water is easiest to handle.

As a result, it is preferable to use the index matching gel in the case where a soling of the sample with a gluey liquid is fine (as with fluorescence collector), otherwise one should use distilled water (e. g. for c-Si wafers which are to thin to clean afterwards).

[6] A refractive index for c-Si of $n = 3.5$ is assumed, since the refractive index between 950 nm and 1200 nm (wavelengths of PL radiation) is between 3.5 and 3.6 and thus the influence of the wavelength on the refractive index is negligible.

[7] Thorlabs Item# G608N.

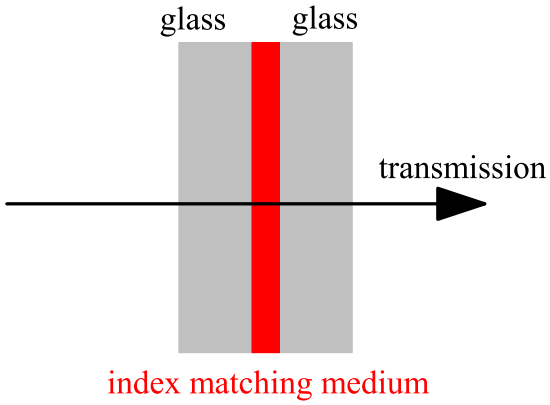

Figure 3.19.: Sketch of the measurements of the transmission through an refractive index matching medium between two glass substrates.

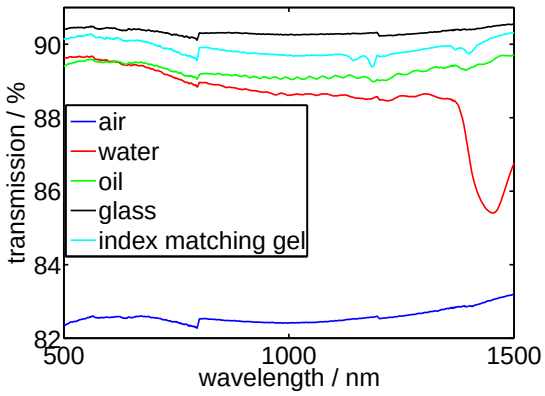

Figure 3.20.: Experimental results of the transmission through two glass substrates with different index matching media between them as sketched in Fig. 3.19.

4. Experimental results and their interpretation

The presentation of the experimental results and their interpretation is divided in 4 sections.
In the first section an overview over the optical properties of a real opal will be given and these results will be compared with the theoretical expectations discussed in chapter 3.5.3.2. A special focus will be dedicated to optical transmission and reflection and to the homogeneity of the opal.
In the second and third section the optical properties of both types of absorber (c-Si and fluco) will be presented. Here the results of transmission and reflection measurements will be given, but it will be concentrated more on the emission properties of both absorbers under excitation.
In the last section the possibilities to trap the PL radiation inside the absorbers with an opal and a Bragg-mirror will be discussed.

But first of all it shall be remarked, that the emission of an excited fluco and c-Si wafer will be called PL (photoluminescence), because the emission in both cases is luminescence and the excitation in done with a laser.

4.1. Characterization of the opal

The results in this section are for an opal in $\Gamma - \mathrm{L}$ direction on top of a glass substrate with a thickness of about $d = 1$ mm and the size of the opal varying in the cm^2 range with around ten layers of PMMA nanospheres. The diameter of the PMMA spheres is either ca. $D = 270$ nm or $D = 540$ nm which leads to a stopgap around $\lambda_{\mathrm{stop}} = 580$ nm and $\lambda_{\mathrm{stop}} = 1200$ nm, respectively. As will be shown in the section on the results of transmission measurements through the opal, the results of both opals are comparable, so often the results of only one of the two kinds of opals are presented.

4.1.1. Transmission

One of the fundamental optical properties of the opal is the reduced transmission around the stopgap, which is used for light trapping. The angularly and spectrally resolved transmission through the opals is plotted in Fig. 4.1. Both measurements for the opals with $\lambda_{\mathrm{stop}} = 580$ nm (left) and $\lambda_{\mathrm{stop}} = 1200$ nm (right) stopgap are performed with the setup described in chapter 3.4.1. Both opals have approximately ten layers of PMMA nanospheres.
The results show the same behavior: a high transmission for wavelengths above the stopgap, a reduced transmission around the stopgap, which shifts to smaller wavelengths with increasing

angle, and a reduced transmission for small wavelengths due to strong scattering. A comparison with the transmission through the substrate in Fig. 4.2 clearly shows the reduced transmission for photons with small wavelength (250 nm $\leq \lambda \leq$ 600 nm), but the transmission for larger wavelengths is also reduced due to scattering (backscattering and scattering to the edges). But the shape of the transmission for both opals apart from the wavelength of the stopgap is similar, which means that the influence of the layer with PMMA spheres is comparable for wavelengths outside the stopgap. The largest disadvantage of the opal is the reduction in the transmission for photons especially with small wavelengths due to scattering, since it reduces the photon flux incident on the absorber. The reasons therefor and a possible solution will be discussed in chapter 4.1.4.

But nonetheless, the stopgap of the opal reduces the transmission through the glass substrate to zero for the opal with $\lambda_{\text{stop}} = 580$ nm stopgap and to 12% for the opal with $\lambda_{\text{stop}} = 1200$ nm stopgap for wavelengths in the stopgap. Thus the opal with $\lambda_{\text{stop}} = 580$ nm stopgap seems to have a higher stopgap quality than the opal with $\lambda_{\text{stop}} = 1200$ nm stopgap, because this opal still shows a transmission above zero for wavelengths in the stopgap. This result will be confirmed in the section about light trapping in both types of absorber.

As mentioned before, from now on only the results for one of the two opals will be depicted and discussed, because the properties for the different stopgaps as in Fig. 4.1 are nearly the same, only the wavelengths of the stopgap being different.

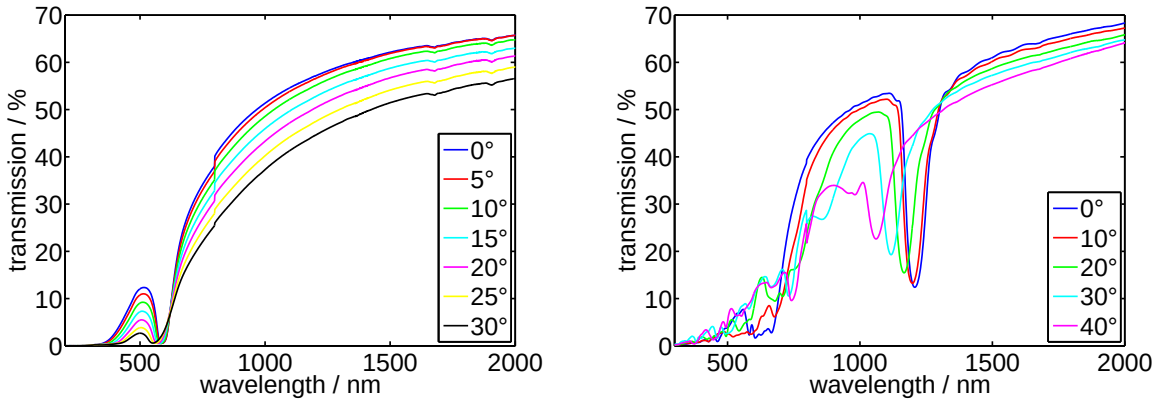

Figure 4.1.: Angular dependent and spectrally resolved transmission through an opal layer on a glass substrate with $\lambda_{\text{stop}} = 580$ nm (left) and $\lambda_{\text{stop}} = 1200$ nm stopgap (right). Both opals have approximately ten layers of PMMA nanospheres.

4.1.2. Reflection

Nearly the same behavior can be observed for the angularly and spectrally resolved reflection from the $\lambda_{\text{stop}} = 580$ nm stopgap opal on glass in Fig. 4.3. A low direct reflection away from the stopgap and a angular dependent reflection peak for wavelengths around the stopgap. The reflection and transmission do not sum up to unity, because of the scattered radiation.

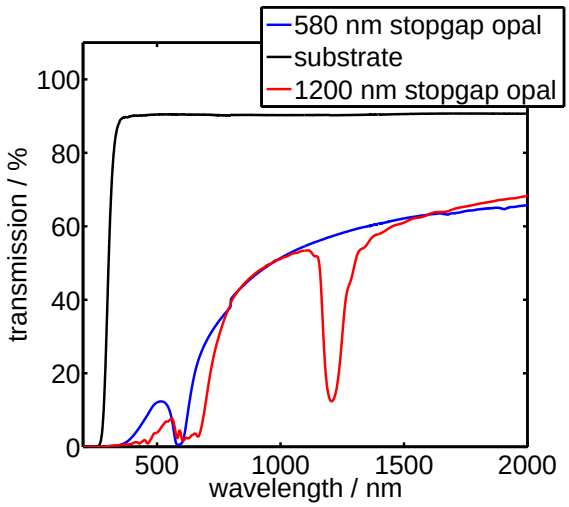

Figure 4.2.: Comparison of the transmission through the opals with $\lambda_{\text{stop}} = 580$ nm and $\lambda_{\text{stop}} = 1200$ nm stopgap with the transmission through the substrate. The reduction of the transmission due to scattering is reduced with increasing wavelength (Mie scattering).

The angular dependence of the reflection peaks can be described by Bragg's law

$$\lambda_{\text{max}} = 2d\sin(\theta) \tag{4.1}$$

with the wavelength of the reflection peak λ_{max}, the spacing between the planes in the atomic lattice d and the angle θ between the incident ray and the planes in the lattice as illustrated in Fig. 4.4.
By including the refractive index n, adjusting the angle to the angle of incidence φ and applying the following theorems for trigonometric functions

$$\sin(\alpha \pm \beta) = \sin(\alpha)\cos(\beta) \pm \sin(\beta)\cos(\alpha) \tag{4.2}$$

$$\cos\alpha = \sqrt{1 - \sin^2(\alpha)} \tag{4.3}$$

on gets the equation for the wavelength of the reflection peak

$$\lambda_{\text{max}} = 2d\sqrt{n^2 - \sin^2(\varphi)} \tag{4.4}$$

which can be found in the literature e. g. in [77].
The wavelength of the reflection peaks for the opal with $\lambda_{\text{stop}} = 580$ nm stopgap are plotted vs. the angle of incidence in Fig. 4.3 with the result of the fit with equation (4.4), but the distance between the lattice planes is expressed in terms of the nanosphere diameter D:

$$d = \sqrt{\frac{2}{3}}D. \tag{4.5}$$

As a result of this fit, the experimentally estimated sphere diameter is $D_{\text{exp}} = (258.7 \pm 6.2)$ nm and the refractive index $n_{\text{exp}} = 1.389 \pm 0.026$ which agrees very well with the nominal parameters

of $D = 270$ nm and $n = 1.37$ for the medium PMMA and air as described in chapter 3.5.3.2. The additional reflection peaks for larger angles of incidence (Fig. 4.3), where the peak wavelength increases with the angle, correspond to another crystal plane see e. g. [78].

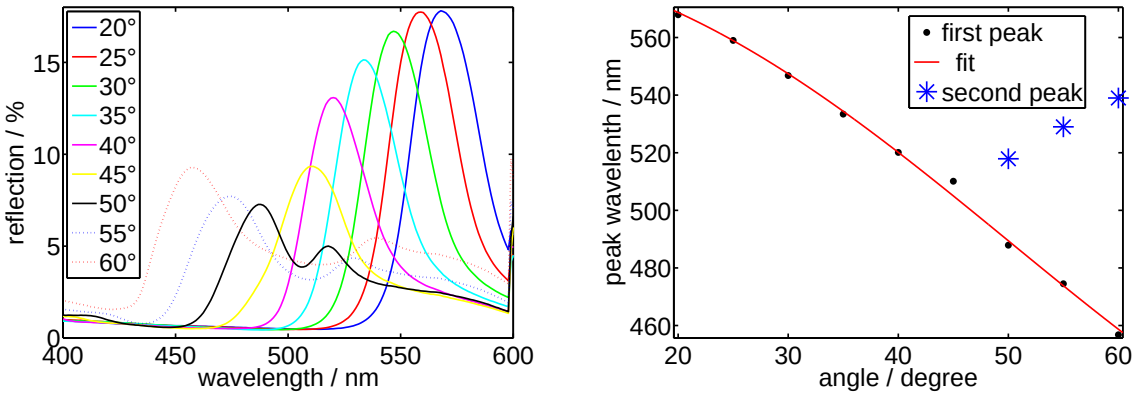

Figure 4.3.: Angular dependent and spectrally resolved reflection at an opal with $\lambda_{\text{stop}} = 580$ nm stopgap on a glass substrate (left) and wavelength of the reflection peaks vs. reflection angle in comparison with the theory (right). The additional reflection peaks for high angles are reflections on another opal plane.

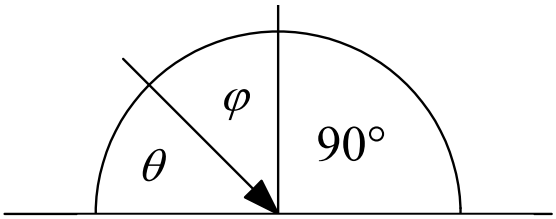

Figure 4.4.: Definition of the reflection angles for Bragg's law (θ) and the angle of incidence φ in the experimental setup.

4.1.3. Absorption

By measurement of the transmission T and the reflection R of a sample one gets access to the absorption $A = 1 - T - R$. The result of the absorption of an opal with $\lambda_{\text{stop}} = 1200$ nm stopgap is plotted in Fig. 4.5 for the measurement of the transmission and absorption with an integrating sphere to get the scattered as well as the direct radiation. To reduce the effect of the glass substrate, the absorption of a bare glass substrate with the same properties is also measured and subtracted from the combined absorption of opal and glass.
Apart from a low absorption for most wavelengths, there is one strong absorption around $\lambda = 670$ nm, which is a disadvantage of the opal as an angular selective filter on top of an

absorber, because the transmitted incident radiation is partly absorbed by the opal.
The reason for this absorption is not clear, because the opal contains only of PMMA nanospheres, which should be nearly transparent in this wavelength regime.
One problem of the subtraction of the absorption of the glass substrate is, that due to inhomogeneities the reference glass substrate and the substrate of the opal are not completely identical, so this could be the reason for an absorption of the opal at $\lambda = 436$ nm below 0%. Another possible reason is, that the angle of the incident radiation for transmission and reflection is not the same due to the design of the integrating sphere, so that the transmissions and reflections are not measured under excatly the same conditions.

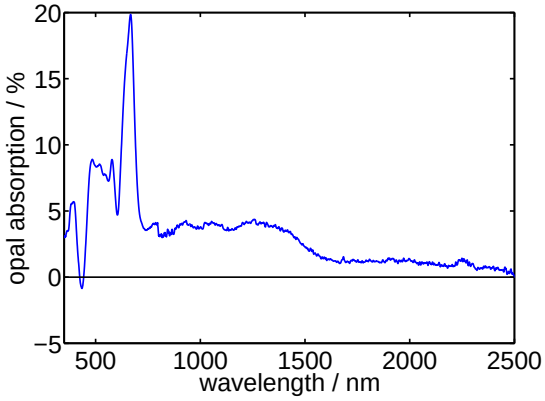

Figure 4.5.: Absorption of an opal with a stopgap at $\lambda_{stop} = 1200$ nm on a glass substrate. The absorption is calculated from the transmission and reflection, and the absorption of the bare substrate has been subtracted.

4.1.4. Scattering

As mentioned before, one of the disadvantages of the opal structure as a photonic crystal for applications on top of an absorber is the strong scattering of the incident light [79]. The differential scattering of the opal samples with $\lambda_{stop} = 580$ nm and $\lambda_{stop} = 1200$ nm stopgap is measured with the goniometer from chapter 3.2, and the result for the $\lambda_{stop} = 1200$ nm stopgap opal is plotted in Fig. 4.6 for excitation at 632.8 nm and 1112 nm. These wavelengths were selected to have one representative for visible excitation of the c-Si wafer and one in the infrared regime of the emitted PL. The scattering results for a clean glass substrate are also plotted in this graph. As can distinctly be observed, the scattered radiation from the opal has a much higher photon flux (about two orders of magnitude) than that from the glass substrate. Thus much of the incident light is scattered back when the opal is put on top of an absorber.
In comparison with the results in [79] the negative logarithm of the direct transmission ($\log_{10}(T)$) shows also a high reduction in the transmission around $\lambda = 600$ nm and $\lambda = 1200$ nm as well as for light with a wavelength below $\lambda = 600$ nm for spheres with $D = 540$ nm diameter.

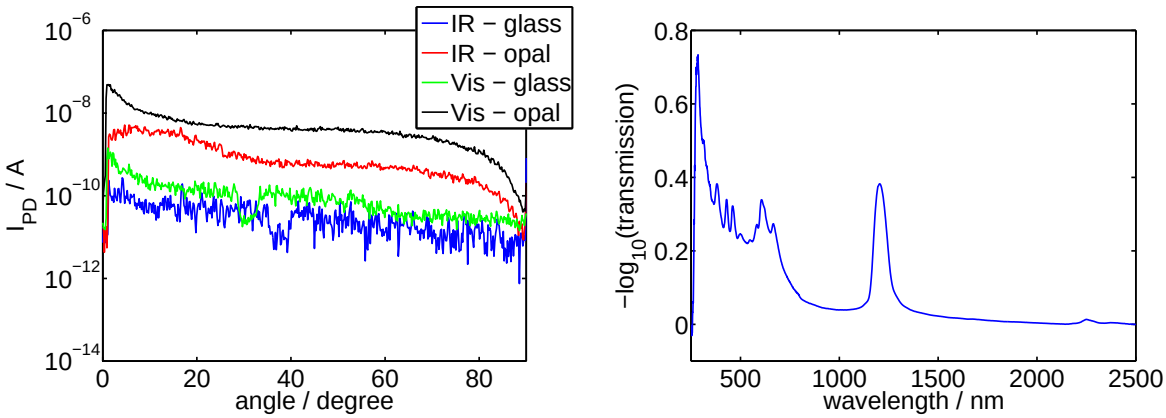

Figure 4.6.: Photon flux scattered by the opal on glass in comparison with the scattering on pure glass for 1112 nm and 632.8 nm (left), and transmission T from Fig. 4.1 (right) in logarithmic representation (right) (4π-analysis).

4.1.4.1. Simulation of Mie scattering

To separate the scattering at the opal structure from the scattering at the nanospheres, the differential scattering of a nanosphere with refractive index $n_{\text{medium}} = 1.5$ in air is simulated with the program MiePlot 4.2.03 [80]. The results in Fig. 4.7 for different sphere diameters (left), incident wavelengths (center) and scattering angles (right) show a behavior which is similar to that of the opal structure on glass:
For incident light with a wavelength of $\lambda = 488$ nm the scattering is rather strong for the sphere diameters of $D = 270$ nm and $D = 540$ nm, which corespondents to the actual samples. The scattering for the visible light is higher than for the infrared radiation and the angular dependence equals roughly the measured results.
In my opinion these results suggest, that the scattering by the PMMA nanospheres are the reason for the strong scattering of the opal for visible radiation and not the photonic structure of the opal. So even a perfect opal would provide strong scattering and thus for an application of this structure one should keep the scattering in mind.

4.1.5. Homogeneity

Important for the application of photonic crystals in a solar cell design is the homogeneity of the photonic crystal. The properties of a photonic crystal should be homogeneous on a µm-scale as well as on a mm-scale, so that in an ideal design no radiation can escape from the absorber and the solar cells have a constant efficiency over a large area.

4.1.5.1. On a µm-scale

The laterally resolved measurement of the reflection on and transmission through the $\lambda_{\text{stop}} = 1200$ nm stopgap opal are plotted in Fig. 4.8 (reflection) and 4.9 (transmission). These figures show the results of the spectrally integrated reflection and transmission measurements, for wave-

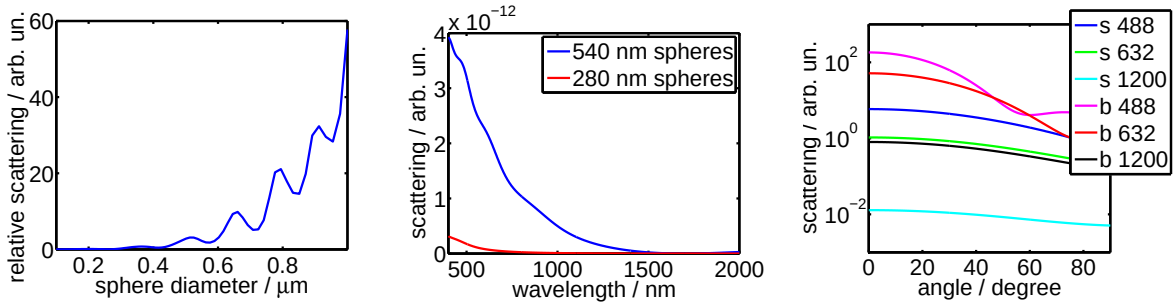

Figure 4.7.: Simulated differential scattering by a sphere with $n = 1.5$ for different sphere diameters (left) for $\lambda = 488$ nm, wavelengths (center) and angles (right) for s: 280 nm sphere and b: 540 nm sphere and the wavelengths: 488 nm, 632 nm and 1200 nm. The results of the simulation of the scattering for different angles equals roughly the measured results in Fig. 4.6.

lengths in the stopgap (a), for wavelengths outside the stopgap (b), for all measured wavelengths (c) and the ratio of (a) to (b) to specify the opal quality (d). The transmission and reflection is given in detector counts per detector element. Both measurements (reflection and transmission) were performed on the same spot of the sample.

One clearly can observe, that both the transmission and the reflection are low in disruptions of the opal which resulted from the drying after the dip-, knife- or spin-coating. Fig. 4.10 displays an AFM image of the opal plotted for a comparable area but on a different position of the sample, where the disruptions are also observable. Unfortunately it was not possible to do the AFM in the same position as the transmission and reflection. In these disruptions the radiation is just scattered away or transmitted.

At the other positions, where the opal is quite homogeneous, the incident radiation is mostly scattered back so that the transmission is low. This behavior is especially visible in the ratio of the radiation for wavelengths in the stopgap to that outside the stopgap. Here the transmission is strong in the disruptions and the reflection is low. The behavior in the good areas of the opal is the opposite.

The area of the good opal regimes is around 200 µm^2, so that the measurements with a larger excitation area will always be performed on several of these good opal regimes with disruptions in between. Also the crystal orientation can vary between these regimes.

Measurements of reflection and transmission of the opal with $\lambda_{\text{stop}} = 580$ nm stopgap shows no indications for disruptions. One reason for this could be, that the disruptions are much smaller due to the smaller PMMA nanospheres, so that the wavelength of the light is too large to actually "see" these disruptions. This could also be a reason for the better quality of the stopgap for the opal with the stopgap at $\lambda_{\text{stop}} = 580$ nm compared to the one with $\lambda_{\text{stop}} = 1200$ nm stopgap observed in the reflection measurements in chapter 4.1.2 and in the application of an opal on c-Si and fluco absorber.

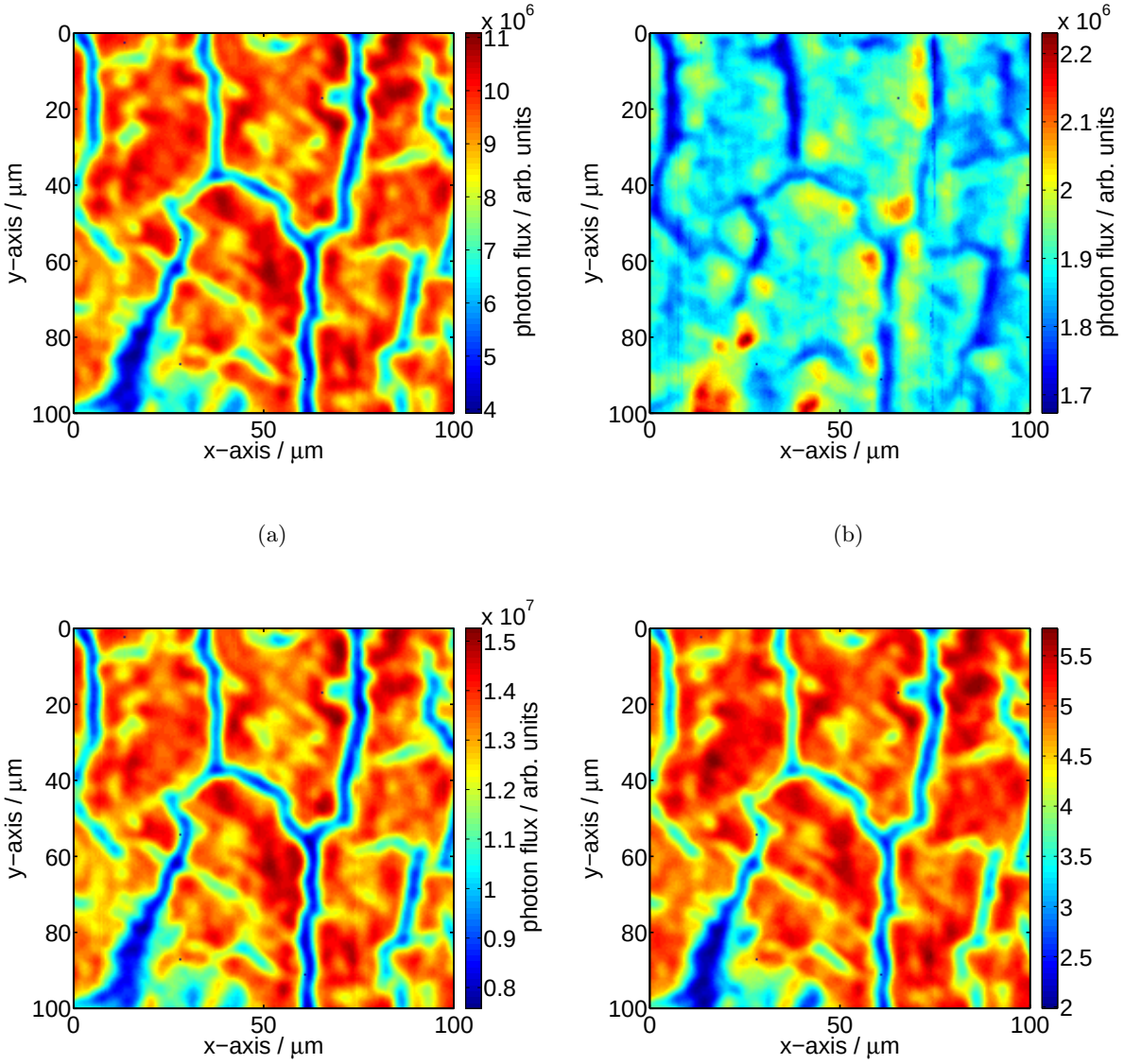

Figure 4.8.: Latterly resolved direct reflection on a 1200 nm stopgap opal on glass substrate with spectrally integrated reflection for wavelengths in the stopgap (a), outside the stopgap (b), all wavelengths (c) and (d) the ratio of (a) to (b).

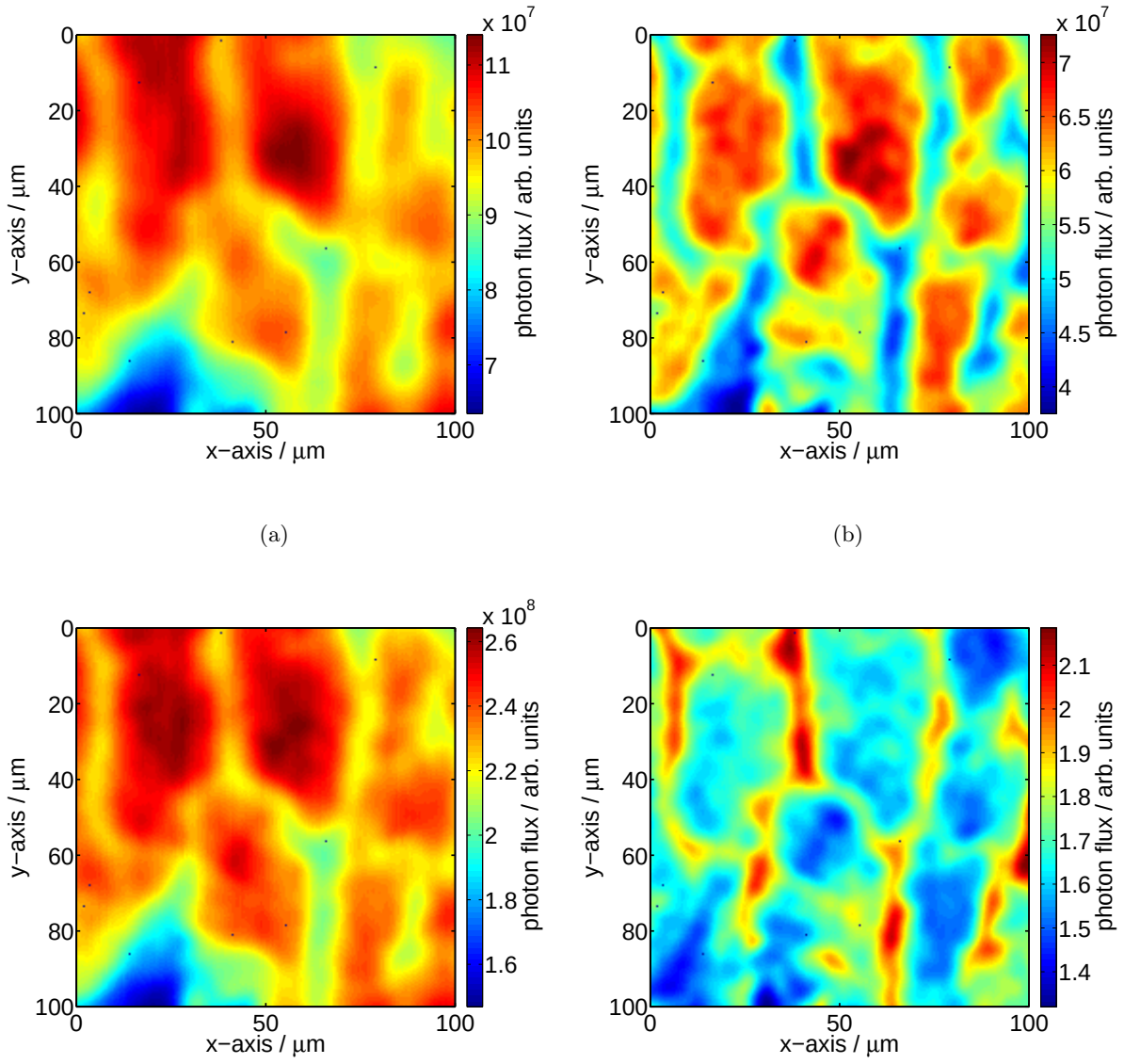

Figure 4.9.: Latterly resolved direct transmission on a 1200 nm stopgap opal on glass substrate with spectrally integrated reflection for wavelengths in the stopgap (a), outside the stopgap (b), all wavelengths (c) and (d) the ratio of (a) to (b).

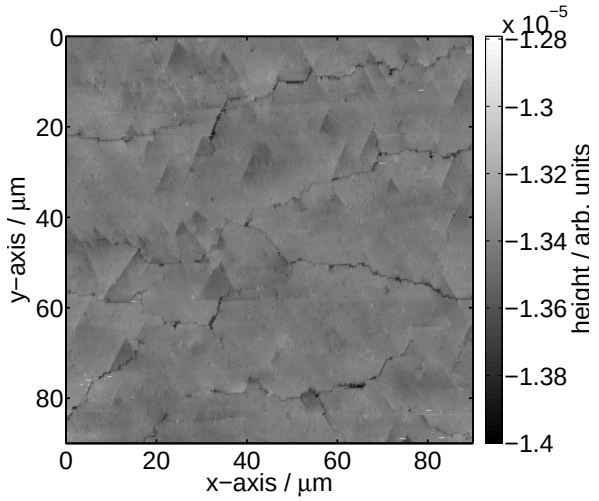

Figure 4.10.: AFM image of the 1200 nm stopgap opal. One can clearly see homogeneous parts of the opal divided by drying disruptions of the wet opal after the coting.

4.1.5.2. On a mm-scale

The characterization of the homogeneity of properties of a photonic structure on a mm-scale is more complicated, because here, the properties represent an average of the properties on the µm-scale.

One possibility to measure the homogeneity of an opal is a laterally resolved reflection measurement as shown before. Such a measurement can be performed on a mm-scale with the Makro-PL setup (see chapter 3.4.3.1): If the measurement is performed with white light (high power LED) and without high pass filter, which normally suppresses the reflection of the excitation source in PL measurements, the reflected radiation is collected and guided to the detector system.

Results of such laterally resolved reflection measurements are plotted in Fig. 4.11. But these results are not corrected with the spectral shape of the LED emission, because this is impossible due to the strong scattering of the opal, so that the values of the integrated photon flux yield no information about the real reflection.

The reflection for wavelengths/photon energies inside the stopgap (left) and outside the stopgap (right) show nearly the same behavior, thus the homogeneity of the reflection on the opal on a mm-scale is nearly independent on the disruptions observed on a µm-scale before.

There are, however, variations in the reflection with a factor of four over the sample visible, which may result from different layer thicknesses of the opal as well as from defects on top of the opal.

A more detailed characterization of the drying disruptions is presented in Fig. 4.12: The left plot shows a microscope image of the surface of an opal with $\lambda_{\mathrm{stop}} = 1200$ nm stopgap on glass under a magnification by a factor of 20. One can distinguish the different opal regimes which are interrupted by drying disruptions. The center image shows an illustration of these disruptions

and the right figure is a histogram of the size of the opal patches between the disruptions.
The illustration of the drying disruptions is a hand-made sketch of the disruptions which has been analyzed by a region growing algorithm for MatLab [81] to calculate the patch size of the enclosed opal regions. The histogram of these patch sizes shows a large number of small patches below 10 μm^2 which result from errors: When one pixel inside a disruption has the wrong value, the region growing algorithm counts this pixel as a disruption with the size of one pixel. Thus the bar at 0-10 μm^2 should be neglected. The real patches show a size between 10 μm^2 and 275 μm^2 and have an average size of about 65 μm^2.
To characterize the effect of the drying disruptions the Fourier transform of the surface of an artificial opal is calculated (as in Fig. 4.13) for round parts of the surface with different diameters. Fig. 4.13 (right) shows the result for an opal surface with a diameter of 40 µm as well as 10 µm and the Fourier transform of a square surface with 40 µm edge length.
All transforms show the same Fourier components but the round surfaces contribute by an additional noisy background which is increased when the sample surface is reduced. For areas $A > 160$ μm the Fourier transforms are almost identical. Thus the size of the patches in the range of the observed patch size has no big influence on the Fourier transform and thus the drying disruptions are of no great importance apart from the stronger transmission of photons with a wavelength inside the stopgap through the opal as discussed before.
Due to this "quasi-independence" of the Fourier transform from the size of the observed opal patches, the photonic band structure of the opal in Fig. 3.8 should also be valid for these patches, because the band structure results in principle from the Fourier transform of the opal structure.

This method provides access to the homogeneity of the opal but one should keep in mind that the sphere diameter must be large enough that the light actually "sees" the disruptions. The spheres of the 580 nm stopgap are so small ($D = 270$ nm diameter) that optical microscopes are not able to resolve the disruptions.

4.2. Characterization of crystalline silicon

In this section the fundamental physical properties of c-Si are displayed, which are needed for the understanding and discussion of the results for light trapping effects. In the literature many articles on c-Si, its properties and the production of silicon solar cells can be found. An overview is given e. g. in [82].

4.2.1. Absorption

One possibility to measure the absorption coefficient was demonstrated in chapter 4.1.3 by using transmission and reflection measurements. Another possibility to measure *low* absorption coefficients is extracting the absorption from the PL and computing the absorption coefficient from Lambert-Beer's law as in chapter 2.1.1.3.
But even if both methods are connected, larger absorption coefficients still pose a problem at

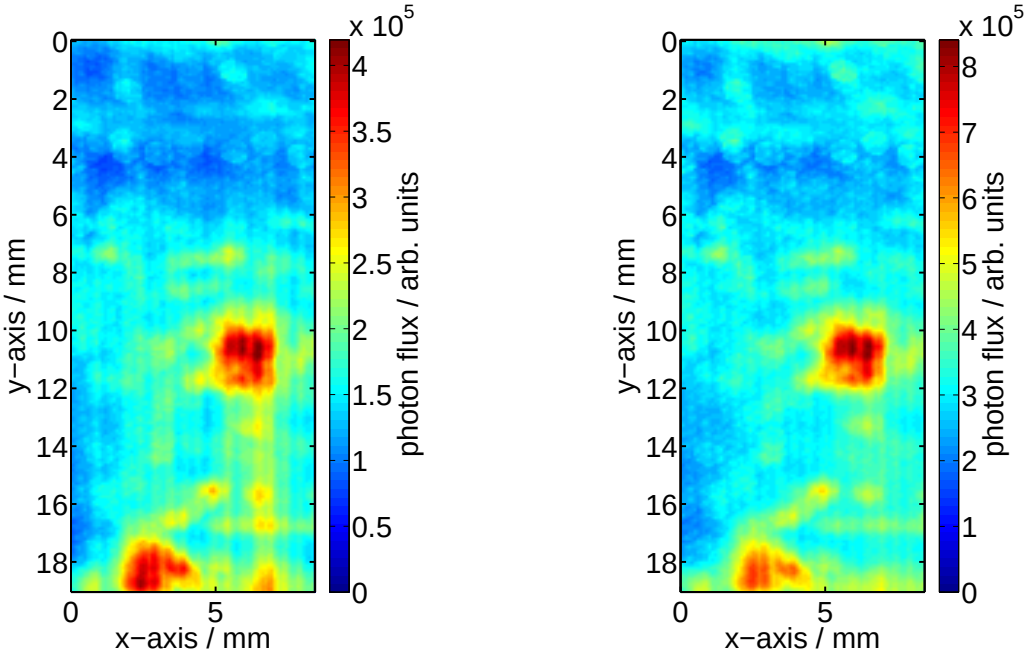

Figure 4.11.: Laterally resolved and spectrally integrated reflection of a white light source on an opal with λ_{stop} = 1200 nm stopgap on a glass substrate. Integration of the wavelengths inside (left) and outside the stopgap (right).The two diagrams are very similar, but the reflection varies strongly over the sample. Note that the reflection is not corrected with the spectral shape of the LED, thus the total values for the reflection inside and outside the stopgap are not quantitatively comparable, only the differences in the relative values are important.

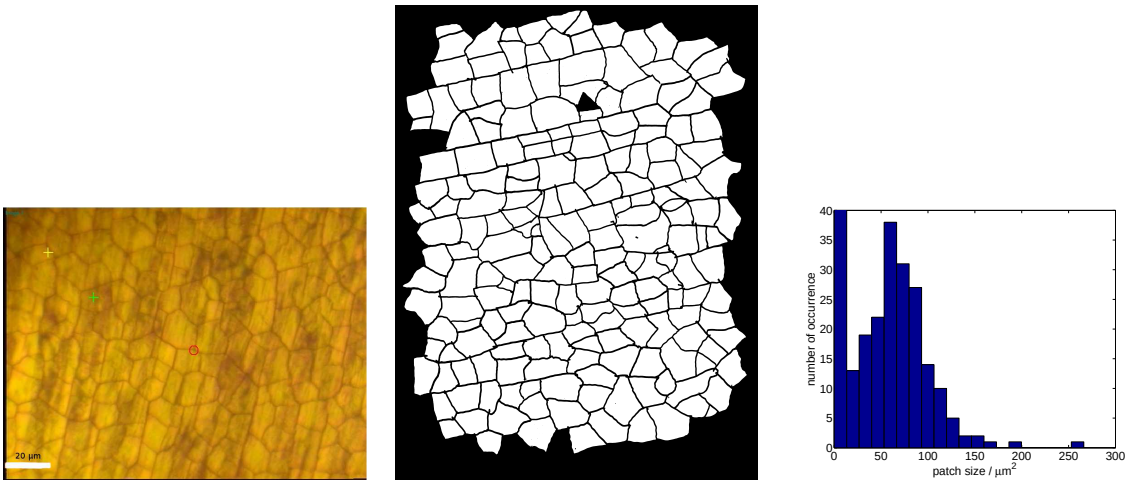

Figure 4.12.: Microscope image of an opal with λ_{stop} = 1200 nm stopgap, 20x magnified (left), illustration of the patches (center) and histogram of the patch size of homogeneous opal regimes (right).

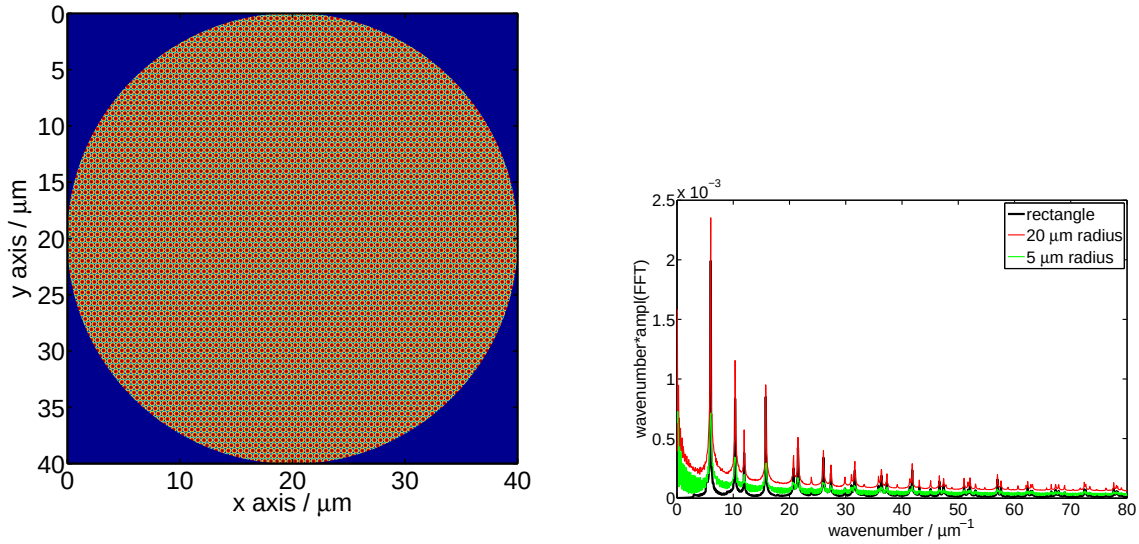

Figure 4.13.: Artificial surface of an opal with $D = 540$ nm spheres (left) with a diameter of 40 µm and 2d Fourier transform of the surface (right) for the rectangular sample and a round sample with a radius of $r = 5$ µm and $r = 20$ µm.

photon energies which correspond to zero transmission. In order to obtain an optimal absorption coefficient for simulations with c-Si, the results from [82] were used, which are plotted in Fig. 4.14. This absorption coefficient shows the indirect and direct band-gap at $E_{Ph} = 1.12$ eV and $E_{Ph} = 4.2$ eV, respectively, at $T = 300$ K temperature.

4.2.2. Angular dependent excitation

To analyze the influence of a photonic structure, located between excitation source and c-Si, on the excitation of the c-Si, the angular dependent excitation of c-Si is characterized. This is done with the setup described in chapter 3.1 with excitation under different angles γ on one c-Si wafer surface and detection under normal incidence on the opposite c-Si wafer surface. The excitation photon flux is $(2.92 \pm 0.13) \cdot 10^{17}$ photons $\mathrm{cm}^{-2}\mathrm{s}^{-1}$ at $\lambda = 488$ nm and the radiation is s-polarized. The result of this measurement is plotted in Fig. 4.15 (left). As expected, the PL yield is reduced with increased absolute value of the excitation angle $|\gamma|$ and the spectral behavior does not change with the angle of excitation. The reduction of the PL photon flux with the excitation angle can be explained by the reduced photon flux hitting the surface and a lower transmission through the front interface between air with refractive index $n_{\mathrm{air}} = 1$ and c-Si with refractive index $n_{\mathrm{cSi}} = 3.5$.
The excitation area A varies with the angle γ

$$A = \pi \left(\frac{d}{2}\right)^2 \cdot \frac{1}{\cos(\gamma)}, \tag{4.6}$$

as plotted in Fig. 4.16, d denotes the diameter of the excitation beam ($\gamma = 0°$ means normal incidence, then the excited area is a circle). So the incident photon flux has to be multiplied

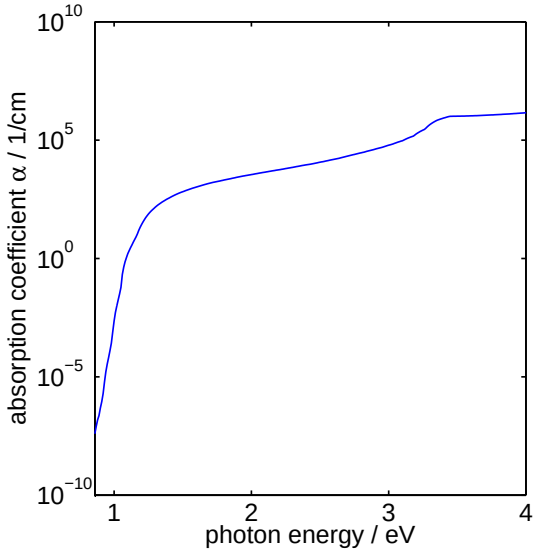

Figure 4.14.: Absorption coefficient $\alpha(E_{Ph})$ of c-Si from [82] with an indirect band-gap at $E_{Ph} = 1.12eV$ at $T = 300$ K.

with the factor $1/\cos(\gamma)$.
As mentioned above, the transmission of the s-polarized light from air to c-Si is given by Fresnel's equation (eq. (2.37)).
The combination of both effects (only the factor of $1/\cos(\gamma)$ and/or the factor of Fresnel's equation for s-polarized light TFs) in comparison with the experimental angular dependence is plotted in Fig. 4.15 (right). The difference between theory and experimental result can be explained by the roughness of the surface and the angular resolution of the setup. The angular resolution broadens the shape of the excitation profile and the angle of incidence is not well defined due to the roughness of the sample which slightly enhances the transmission given by Fresnel's equations.

This result is very important for experimental setups, where an excitation under normal incidence is not possible (e. g. due to other experimental components), because an absolute value of the excitation angle below 20° ($|\gamma| \leq 20°$) reduces the emitted PL photon flux only up to 7% and does not influence the spectral behavior, as a variation in the excitation should only lead to a variation in the splitting of the quasi-Fermi levels. So only the absolute values from eq. (2.1) are different and not the spectral behavior which is given by the spectral emissivity $E(E_{ph})$ and should not vary for reasonable excitation photon fluxes.

4.2.3. Angular dependent emission from top

To measure the angular dependent PL emission of c-Si the setup from chapter 3.1 is used with $\lambda = 488$ nm excitation, s-polarized light, excitation from one side and detection from the opposite side of the wafer (an illustration of the setup can be found in Fig. 4.17), an excitation spot with diameter $d = 1.1$ mm and a photon flux of $(2.92 \pm 0.13) \cdot 10^{17}$ photons $\mathrm{cm}^{-2}\mathrm{s}^{-1}$. As mentioned

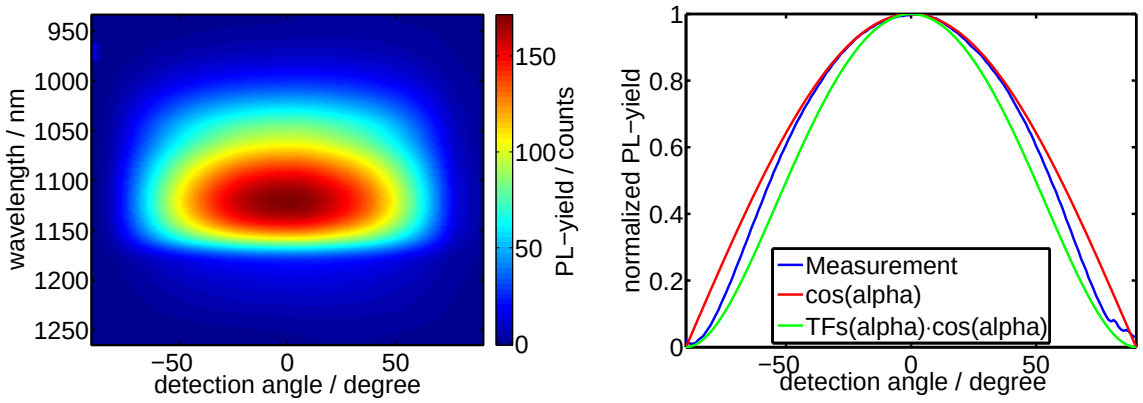

Figure 4.15.: Angular dependent and spectrally resolved emitted PL yield from c-Si for different excitation angles (left) and comparison of the angular dependency with a theoretical model (right).

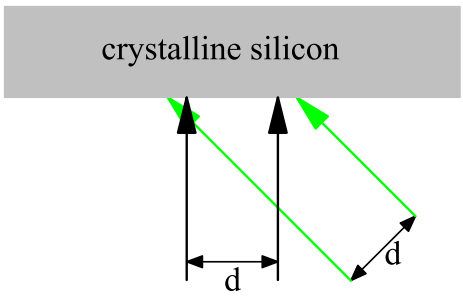

Figure 4.16.: Sketch of the increased excited absorber area when the excitation angle is varied from $\gamma = 0°$ to $\gamma = 45°$ for a laser beam with diameter d.

before, it is important, that the axis of rotation lies exactly in the surface of the c-Si from which the emission is detected.
The result is plotted in Fig. 4.18 (left), where one can observe a reduction of the photon flux with increasing absolute value of the detection angle δ and a shift of the maximum photon flux to larger wavelengths for larger angles. The reduction of the photon flux with increasing $|\delta|$ is caused by a reduced transmission due to Fresnel's equations (eq. 2.37). The shift of the maximum wavelength is caused by two facts:
The area from which the PL photons are collected on the surface of the c-Si varies with the detection angle in the same way as for the angular dependent excitation and thus this area is increased with the absolute value of the detection angle. But the excitation is only on a spot of $d = 1.14$ mm diameter, so that the PL emitted from positions outside this spot is composed of more photons with lower photon energy because of stronger reabsorption for photons with high photon energy and the longer propagation length inside the absorber for emission positions outside the excitation spot.
The second reason is the emission from the edge of the c-Si wafer. As will be shown in chapter 4.2.5, the PL leaving the edge of the c-Si wafer has a much lower photon flux for high photon energies than the emission from the top, and this radiation is also collected for larger absolute detection angles.
In Fig. 4.18 the normalized integral photon flux for photons with photon energies between $E_{Ph} = 0.99$ eV and $E_{Ph} = 1.31$ eV is plotted in comparison to the result of the PL emission simulated for 50% s- and 50% p-polarizations from chapter 2.2.2.2. The differences between simulation and experimental result can have several reasons:

- Fresnel's equations are only valid for perfectly flat surfaces and not for rough surfaces. The c-Si waver is polished but not perfectly flat.
- If the axis of rotation is not directly in front of the surface of the absorber, the emission is not perfectly symmetric with respect to the angle of detection.
- The area from which the emission is detected changes as discussed in chapter 4.2.2.
- As discussed in chapter 4.2.5 there is an emission from the edge of the c-Si wafer, which reaches the detector for larger angles and thus influences the angular dependence for larger angles.

Thus the experimental results agree with the simulation but the experimental setup has to be improved to measure the absolute angle dependence of the emitted PL yield. Especially the detection area must be kept constant. However this problem is of no concern for the comparison of the emission with and without a photonic structure, which is the aim of this work.

The disadvantage of the experimental setup discussed above consist in the positioning of the sample by hand: As depicted in Fig. 4.17 the surface of the sample must be directly in the axis of rotation of the emission. In the current setup, this position is judged by the eye. A much

better solution is the automatic positioning of the sample as plotted in Fig. 4.19. Here the sample holder is designed in a way that the sample is pushed against the holder, so that the surface of the sample is automatically in the right position.

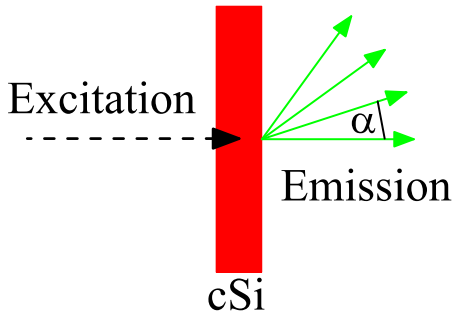

Figure 4.17.: Illustration of the measurement of the angular dependent PL emission of excited c-Si with excitation on one side and detection on the opposite side. Note that the axis of rotation must be in top of the c-Si wafer.

4.2.3.1. Calibrated PL from the top of the absorber

To discuss the emission properties of c-Si the calculation of the analysis of the PL yield as announced in chapter 2.1.1 will be presented. Therefore the calibrated PL yield of a c-Si wafer measured under normal incidence is plotted in Fig. 4.20. The excitation was performed with a 532 nm laser with a photon flux of $(1.4 \pm 0.1) \cdot 10^{18}$ photons $s^{-1}cm^{-2}$, which is higher than the AM1.5 equivalent photon flux of $2.7 \cdot 10^{17}$ photons $s^{-1}cm^{-2}$ to enhance the signal-to-noise ratio. The shape of the emitted PL is governed by the shape of the absorption coefficient plotted in Fig. 4.14 and the Bose term

$$\left[\exp\left(\frac{E_{Ph} - \mu}{k_B T}\right) - 1\right]^{-1}. \tag{4.7}$$

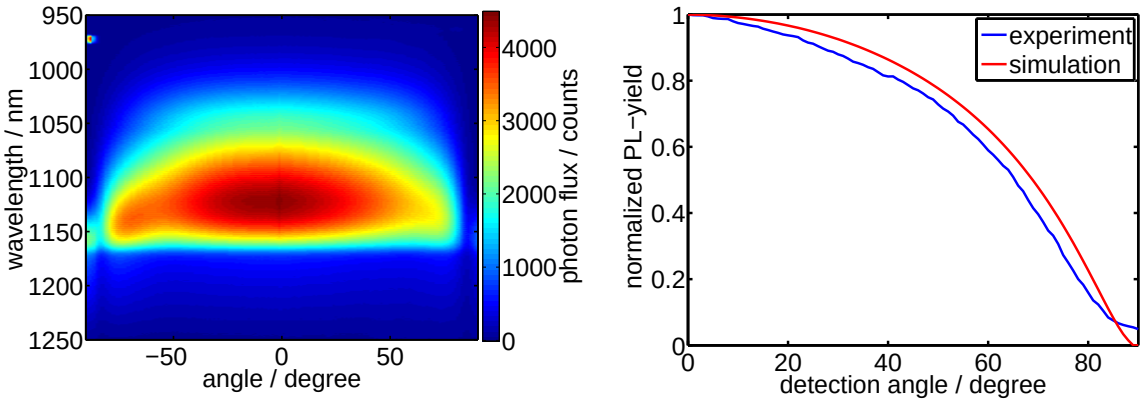

Figure 4.18.: Angular dependent and spectrally resolved PL yield from an excited c-Si wafer (left) and comparison of the angular dependence with the simulation (right).

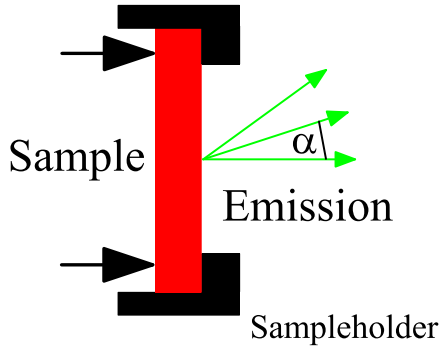

Figure 4.19.: Sketch of a better way to mount the sample, so that the surface of the emission side of the sample is directly on the axis of rotation.

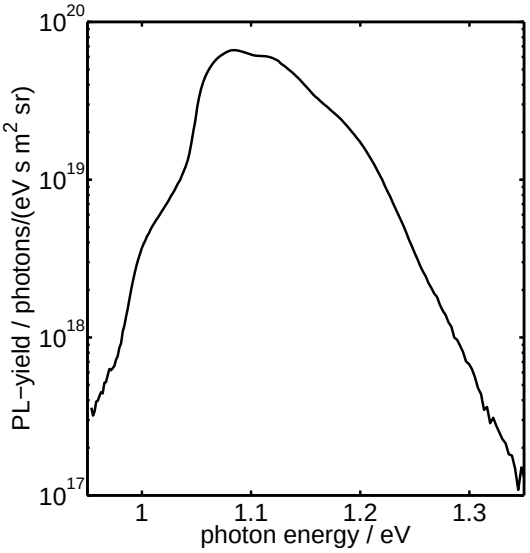

Figure 4.20.: Absolute PL yield from an excited c-Si wafer.

Results of the calculation of the splitting of quasi-Fermi levels and the temperature of the sample from the PL yield according to the theory in chapter 2.1.1 can be found in Tab. 4.1. Both values are rather large due to the high excitation photon flux which heats up the c-Si sample at the spot of the measurement.

4.2.4. Homogeneity

Fig. 4.21 depicts the integral

$$\Gamma_{\text{total}}(x,y) = \int_{E_{\text{min}}}^{E_{\text{max}}} \Gamma(x,y,E_{Ph}) dE_{Ph} \tag{4.8}$$

of the laterally (on mm-scale) and spectrally resolved (setup from chapter 3.4.3.1) PL yield $\Gamma(x,y,E_{Ph})$ for the different x- and y-positions and the photon energies E_{Ph} between $E_{\text{min}} =$

Table 4.1.: Results of the analysis of the c-Si PL yield in Fig. 4.20 (left).

Parameter	Value
T	(323 ± 12) K
μ	(676 ± 25) meV

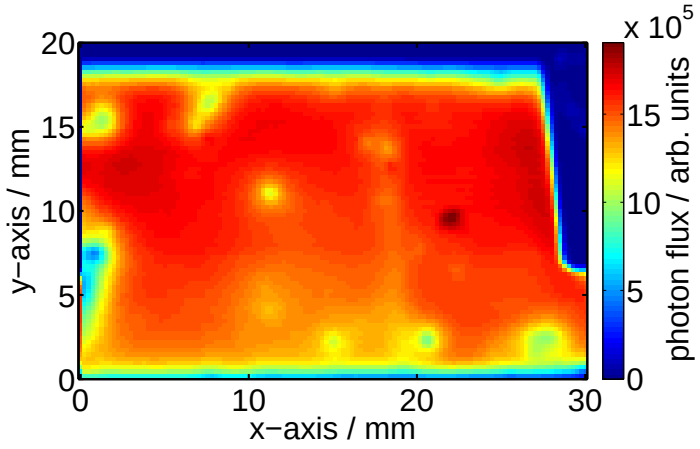

Figure 4.21.: Image of the laterally resolved and spectrally integrated PL yield from an excited c-Si wafer.

0.99 eV and $E_{\max} = 1.35$ eV given by the experimental setup. The blue area with nearly no detector signal is caused by the sample holder. The integral PL yield of the c-Si sample varies over nearly one order of magnitude between different sample positions which can result from the quality of the surface passivation, because the emitted PL yield is rather sensitive to the surface recombination velocity as shown in chapter 2.3.1.1.
As a consequence of this inhomogeneity, the PL yield of different wafer positions is not identical and thus cannot be compared.
So the influence of a photonic structure on the emitted PL yield is measured as illustrated in Fig. 4.22: The emission from the c-Si wafer without photonic structure is measured with a glass substrate on the side of detection, and the emission with a photonic structure is measured with the photonic structure on a glass substrate which is attached to the c-Si wafer. In both cases the measurements are performed with a refractive index matching medium (distilled water) between the c-Si wafer and the glass substrate. Thus the measurements are performed on the same spot of the c-Si wafer and the surface passivation of the c-Si is not influenced by the deposition of the photonic crystal, since it is deposited on a glass substrate and not on the c-Si wafer.
Due to this setup it is possible to neglect the influence of the glass substrate below the photonic structure on emission as well as the inhomogeneity of the c-Si wafer.

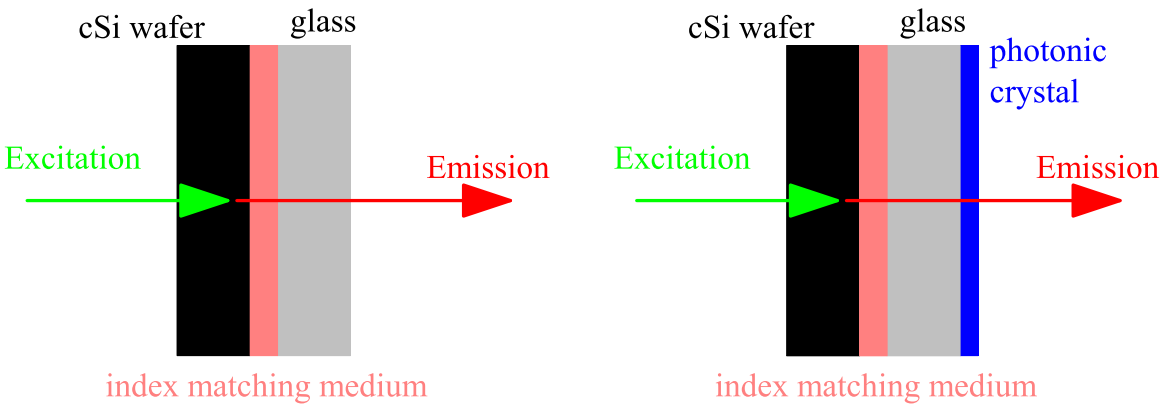

Figure 4.22.: Illustration of the experimental setup for the comparison of the PL emission from a c-Si wafer with glass substrate (left) and a c-Si wafer with photonic crystal on a glass substrate (right).

4.2.5. Edge emission

A c-Si wafer shows similar properties as a fluco but only for infrared instead of visible radiation: The reemission of the excited c-Si takes place inside a material with refractive index of $n \approx 3.5$ with polished surfaces, thus a part of the emitted infrared radiation is trapped inside the wafer by total internal reflection and guided to the edge of the wafer. On the way to the edge a part of the radiation is absorbed and thus the spectral shape of the edge PL should be different from that of the top PL.
Fig. 4.23 (right) shows the result of the measurement of the edge emission under normal incidence (on the edge) of a c-Si wafer for an excitation with a 488 nm laser which hits the sample ca. 1 cm away from the edge. This measurement is done with the angular dependent PL. The figure also shows the result of the simulation described in chapter 2.2.2 with the excess carrier concentration plotted in Fig. 4.23 (left) as well as the measured top PL under normal incidence. The PL yield for small photon energies of the edge emission is nearly the same as the one of the emission from the top, but for higher photon energies the PL yields are different due to absorption. The absorption increases with increasing photon energy due to the higher absorption coefficient as well as with increasing propagation length to the surface of the c-Si. The lateral excess carrier concentration in Fig. 4.23 (left) has been designed for the excitation in the middle of the absorber with infinitesimally small excitation area and an exponential decay to the edges ($\exp(-\alpha x)$) regarding the diffusion length of the excess carrier.
The experimental and theoretical results agree quite well, which is also an indication that the description of the propagation of radiation in the theory is a good model for many different problems.

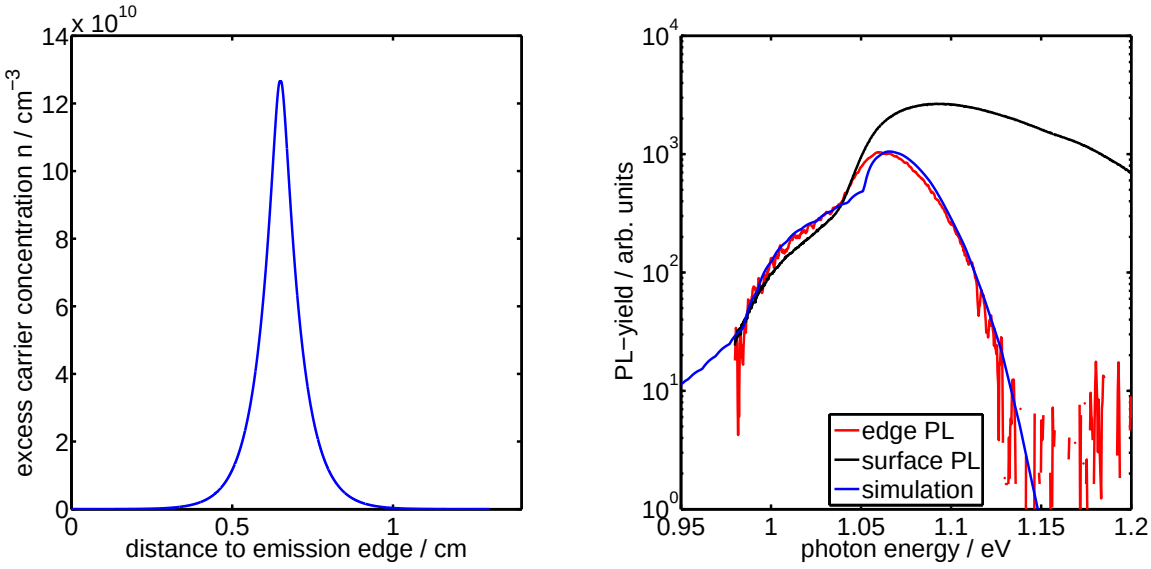

Figure 4.23.: Lateral excess carrier concentration for the simulation of the edge emission (left), measured PL from top and edge and simulated PL for a c-Si wafer (right). Note that the results for the edge and surface PL were measured under the same excitation but the edge PL was measured with a ten times longer integration time to get a better signal-to-noise ratio, and the result of the simulation is normalized to the maximum of the edge PL.

4.3. Characterization of the fluco

This section gives a short overview on the optical properties of the flucos used in chapter 4.4 in which light trapping possibilities are discussed. The design of the fluco should be improved by a photonic structure, which should enhance the edge emission, so the focus will be especially on the edge emission of the fluco.

4.3.1. Absorption

One important optical property of flucos is the absorption of light, which can be calculated from optical transmission T and reflection R by

$$A = 1 - T - R. \tag{4.9}$$

The results of direct transmission and direct reflection measured with the setup described in chapter 3.4.1 are plotted in Fig. 4.24 for flucos with the dyes Rhodamin 6 G and Cumarin 540A. These results show that both the reflection and the transmission of the flucos depend on the dye concentration given by the arbitrary numbers 500, 1000 and 2000 in the legend. An increased dye concentration results in a reduced transmission and a reduced or enhanced reflection (depending on the dye). Such a dye concentration dependent reflection results from the imperfection of the setup: The detector collects not only the transmitted radiation but part of the emitted radiation as well. So the reflection is dye concentration dependent, since the emission and the

reflection are dye concentration dependent. The reflection is dye concentration dependent, since the Kramers-Kronig relation connects the absorption and the refractive index and the latter yields the reflexion.
By consequence, the absorption (plotted in Fig. 4.25) should always be calculated from eq. (4.9) with transmission and reflection and not only from the transmission.
When comparing these results with literature (e. g. [83]), one has to consider that the dye in a fluco is embedded in a matrix material like PMMA, so the absorption and emission properties are slightly different from those for dyes in liquids.
One should also keep in mind that the experimental determination of transmission, reflection and absorption as described above for fluorescence materials like flucos is not perfect, because the spectrometer collects not only the transmitted and reflected radiation but the emitted radiation of the dye as well, so the reflection and transmission are always overestimated. An alternative method to estimate reflection, transmission and absorption with consideration of the dye emission is discussed in [41] or [84], which e. g. can yield the fluorescence emission as well as the parameters mentioned above.

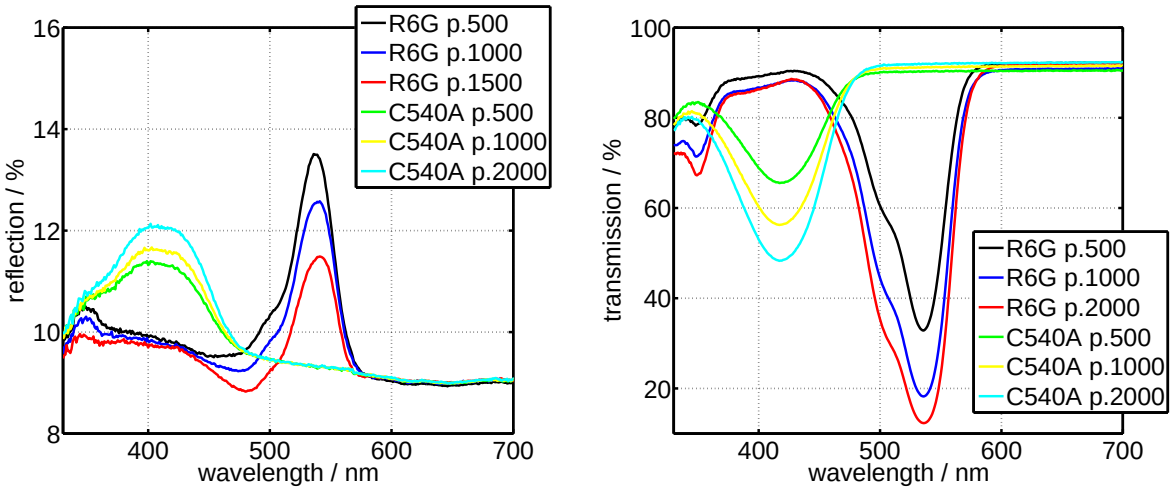

Figure 4.24.: Direct reflection (left) and transmission (right) results for flucos with Cumarin 540A and Rhodamin 6 G of different concentrations of different concentrations.

4.3.2. Emission

Before the angular dependent emission from the edge and top of the flucos with Rhodamin 6 G as well as those with Lumogen F rot 305 are discussed, the absorption and emission properties of the flucos will be introduced.
The normalized emission and normalized absorption of both flucos are plotted in Fig. 4.26 (Rhodamin 6 G (left) and Lumogen F rot 305 (right)). Both, absorption and emission strongly depend on the dye concentration. The difference in wavelength between maximum emission and absorption is called Stokes shift, which is caused by a "rapid decay to the lowest vibrational level" [85]. This spectral splitting of the emission and absorption provides an additional possibility for the

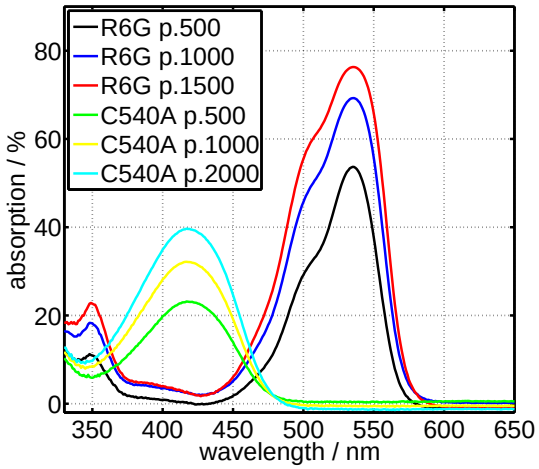

Figure 4.25.: Absorption calculated from the reflection and transmission in Fig. 4.24.

design of a photonic structure to reduce the reemission of the escape cone. All photons which are absorbed by the dye should be transmitted and the emitted photons should be reflected by a filter on top of the fluco. The edge wavelength of such a low-pass filter should be between the maximum absorption and the maximum emission. The disadvantage of such a design is the shift of the edge wavelength of the filter with the angle of the incident light on the photonic structure as discussed in chapter 4.1.2, so either the absorption of radiation with a larger angle of incidence is reduced or the reflection of the emitted radiation under small angles is not appropriate.
A discussion of the optimal edge wavelength of a low-pass filter for flucos can be found e. g. in [86], so a discussion of the perfect wavelength of the edge filter will not be given here, especially since only a low-pass filter with an edge of 550 nm was available in the size of the fluco and the excitation was performed with a laser with a wavelength of 488 nm or a high power LED with 505 nm which are both away from the edge of the filter.
The results of the absorption and emission in Fig. 4.26 indicate that the opal with a stopgap at 580 nm matches the emission from the Rhodamin 6 G fluco but not that from the Lumogen F rot 305 fluco, and that the 550 nm edge low-pass filter matches both emission spectra. The influence of both filters on the top and edge emission as well as on the excitation will be discussed in chapter 4.4.

4.3.3. Angular dependent edge emission

The measurement of the angular dependent edge emission from a fluco with Rhodamin 6 G in PMMA on glass was performed in the same way as described in chapter 4.2.5 for c-Si but not with a spot excitation but with a slit excitation with a specified distance from the edge of the collector. A sketch of the measurement is illustrated in Fig. 4.27 (right) where the fluco is positioned on a sample holder with a screen between excitation and emission. Here the sample is illuminated with a 488 nm laser along a line parallel to the edge from which the PL is measured. The dye in PMMA was located at the front of the fluco.

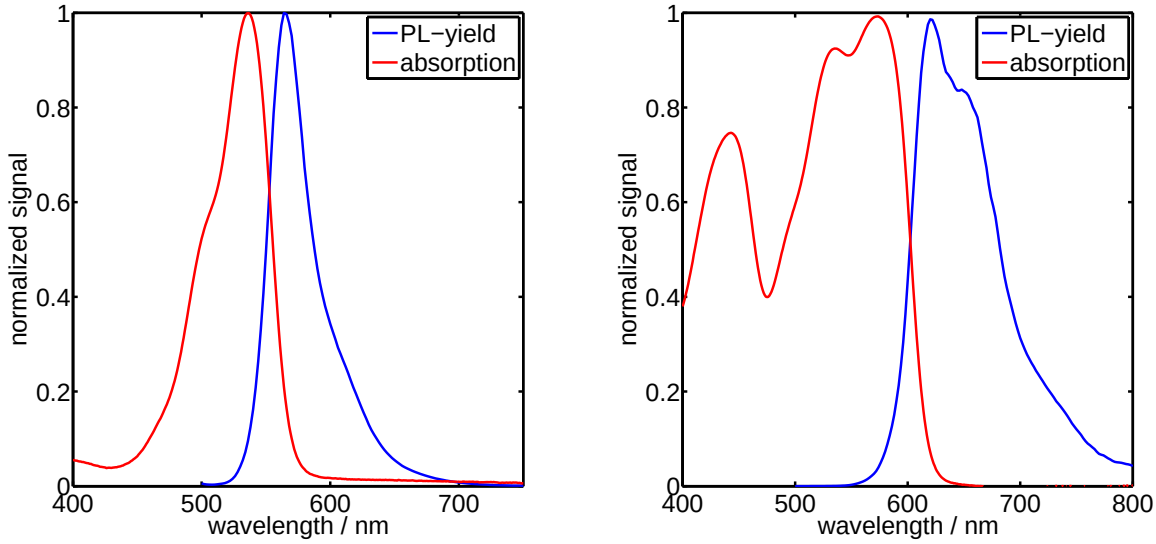

Figure 4.26.: PL emission from and absorption of an excited fluco with Rhodamin 6 G in PMMA on the surface of a glass substrate (left) and a fluco with Lumogen F rot 305 in PMMA (right).

The spectrally integrated PL yields are plotted in Fig. 4.27 (left) for different distances between excitation and fluco edge and compared with the results of the simulation in chapter 2.2.3. The solid lines represent the edges of the simulation results, so the experimental results agree quite well with the simulation.
The small spectral differences in the PL for different detection angles and for different distances between the excitation and the edge of the fluco are discussed in more detail in appendix D.
The angular dependent edge emission for different distances of the excitation to the emission edge for the fluco with homogeneous dye concentration are plotted in Fig. 4.28 for 0.8 g/l Lumogen F rot 305 (left) and 0.3 g/l dye concentration (right). The results for the fluco with the higher dye concentration still show the same behavior as the fluco with dye on top: There are angle-distance regimes with nearly no emission and such with high emission. But for the fluco with the lower dye concentration the emission vs. distance and angle is more homogeneous, because the excitation depth profile of the dye is more homogeneous so that the upper and lower halves of the fluco nearly have the same emission as was described for a fluco with homogeneous dye concentration in chapter 2.2.3.2.
This behavior can also be observed in the angular dependence of the spectrally integrated edge emission for a spot excitation on top of the fluco in Fig. 4.29. The entries in the legend with "from top" refer to a measurement for a spot excitation on the top of the fluco whereas "from bottom" indicates that the emission was measured for an excitation (Fig. 4.27 (right)) from the bottom of the fluco. The second measurement yields the emission for negative emission angles.
Here the results show also a more homogeneous emission for the lower dye concentration due to a more homogeneous excitation depth profile. The emission is asymmetric around zero degrees

because of the non-constant emission depth profile, and the emission around zero degrees is lower than expected, because the design of the sample holder influences the emission measurements for small angles.
It would be interesting to compare the excitation depth profile with the efficiency (here the efficiency that an absorbed photon reaches the edge of the fluco after reemission) of the fluco to obtain the best excitation depth profile for a fluco.
The image on the title page shows the opposite case: A fluco with dye in PMMA on a glass substrate is illuminated on the edge with a laser and some areas on the top show fluorescence.

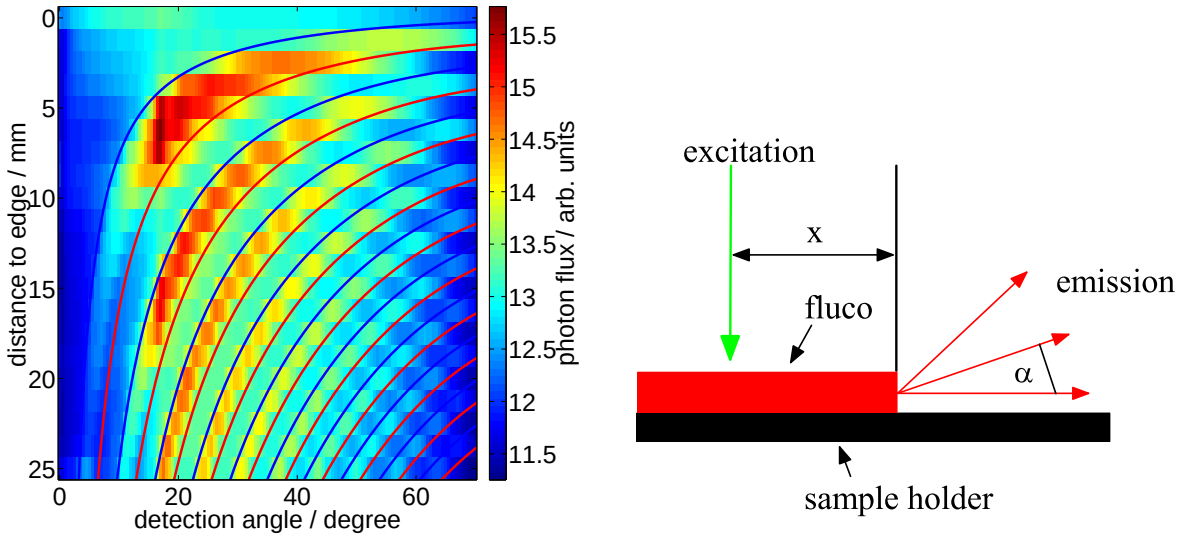

Figure 4.27.: Spectrally integrated angular dependent edge emission of a fluco doped with Rhodamin 6 G in PMMA on glass in dependence of the distance between edge and excitation spot in comparison with the simulation results from chapter 2.2.3 (left) and sketch of the experiment (right).

4.3.4. Angular dependent emission from top

The angular dependent emission from the top of a Lumogen F rot 395 fluco with 0.3 g/l dye concentration plotted in Fig. 4.30 (left) was measured with the same setup and excitation as in chapter 4.2.3 with c-Si. As with c-Si the emission is reduced with increased absolute detection angle $|\gamma|$ but the spectral shape of the emission is nearly constant. Fig. 4.30 shows the comparison of the angular dependence of the emission from the fluco with 0.8 g/l and 0.3 g/l dye concentration together with the emission from c-Si from Fig. 4.18, the simulation of the angular dependence for c-Si as well as a simple simulation of the edge emission for a fluco.
This simulation is based on an isotropic emission of the dye inside the substrate with refractive index of $n_{\mathrm{sub}} = 1.5$, the transmission through the surface into the air ($n = 1$) given by Fresnel's equations eq. (2.37) and the increase of the angle increment eq. (2.44). It does not consider reabsorption and multiple reflections.

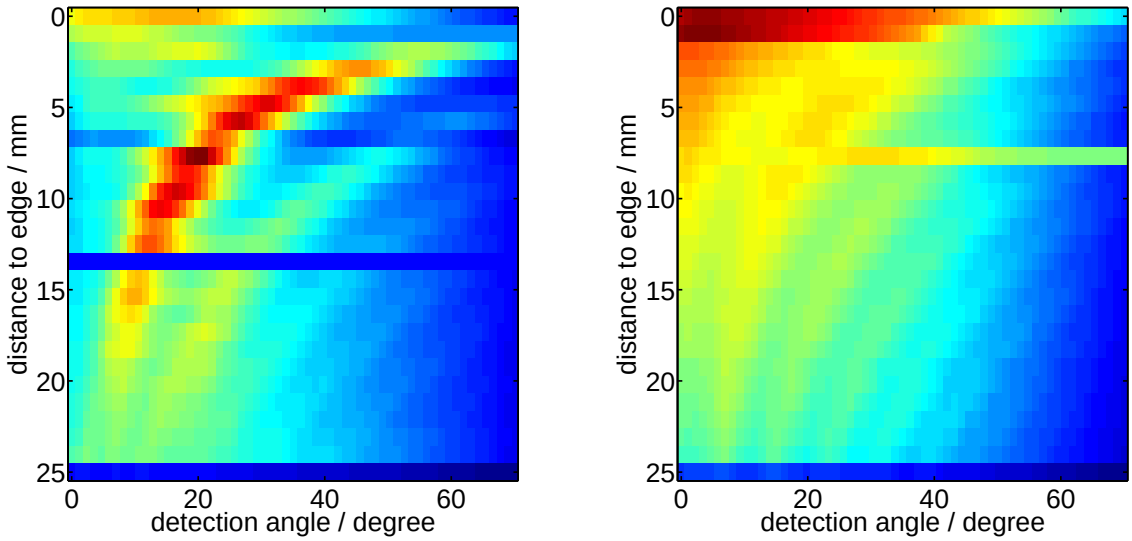

Figure 4.28.: Angular dependent and spectrally integrated PL yield for various distances of the excitation from the emission edge for the Lumogen F rot 305 fluco with a dye concentration of 0.8 g/l (left) and 0.3 g/l (right).

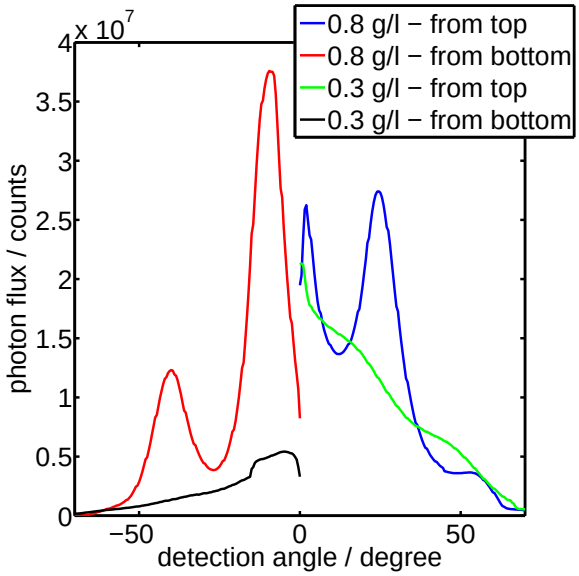

Figure 4.29.: Angular dependence of the spectrally integrated PL yield for a spot excitation of the Lumogen F rot fluco with 0.8 g/l and 0.3 g/l dye concentration.

The angular dependence of all results (experimental and simulated c-Si emission, emission of the fluco with low and high dye concentration and fluco simulation) are nearly equal, especially if the disadvantages of the angular dependent PL setup from chapter 4.2.3 are considered. Thus to be able to discuss the differences of the angular dependences of the different flucos in more detail, a better adjustment of the sample with the surface on the axis of rotation is needed.
Differences between the results of the two dye concentrations also must be caused by the error of the not exactly adjusted sample, because a higher dye concentration leads to a higher reabsorption, but this reabsorption should be similar for the different emission angles, because

- an emission angle outside the absorber of 89° corresponds to an angle of about 41.8° inside the fluco and thus the propagation length differ between an emission with 0° and 89° by a factor of 0.31 which does not alter the emission by a factor of 2 at 80° like observed in the experiment.

- the excitation depth profile for a higher dye concentration is not as constant as for the lower dye concentration, but this would lead to an even more reduced photon flux for larger emission angles, because the excitation is performed on the side of the fluco and the PL emission is detected on the opposite side, so that the emitted photons propagate a longer distance inside the fluco for a higher dye concentration and this propagation length is even longer for high emission angles as has been discussed above.

It is recommended for future approaches to repeat these measurements with an improved setup and include reabsorption and an emission depth profile in the modelling.

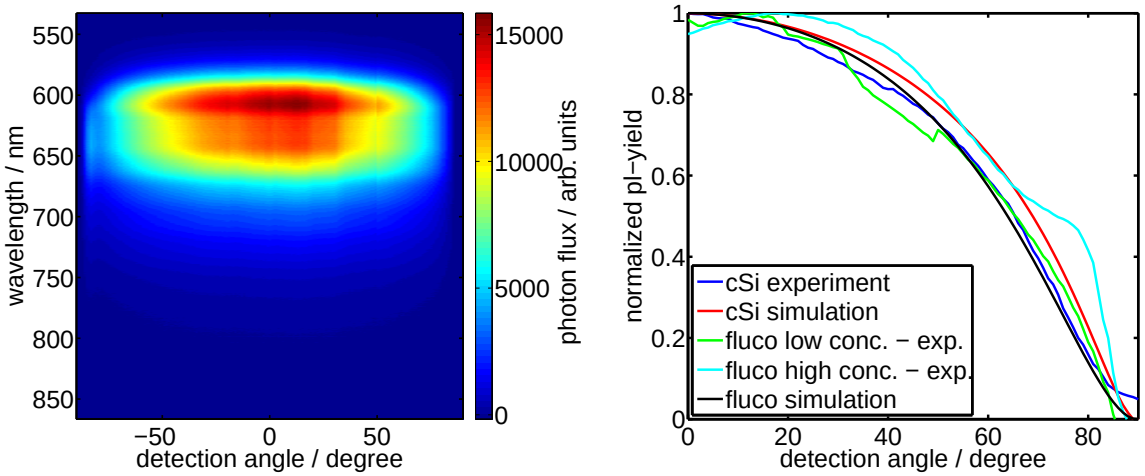

Figure 4.30.: Angular dependent and spectrally integrated top emission of an excited Lumogen F rot 305 fluco (left), the angular dependence in comparison to the angular dependence of c-Si, the simulation for c-Si as well as a simple simulation for the fluco (right).

4.3.5. Angular dependent excitation

The angular dependent excitation of the fluco is measured in the same way as for crystalline silicon in chapter 4.2.2: Different excitation angles with 488 nm excitation on a spot with $d = 1.1$ mm diameter and a photon flux of $(2.92 \pm 0.13) \cdot 10^{17}$ photons $\mathrm{cm}^{-2}\mathrm{s}^{-1}$ on one side of the absorber and spectrally resolved detection under normal incidence on the opposite side of the absorber.
As can be seen in Fig. 4.31 the normalized PL yield is nearly constant over a broad range of the excitation angle between $-40°$ and $40°$ compared to the more cosine-like shape of the curve for c-Si. The reason therefor is not clear.
This is the great advantage of flucos: They are able to absorb diffuse radiation (with a higher efficiency than a semiconductor) as well as direct radiation and can concentrate both direct and diffuse light [41].

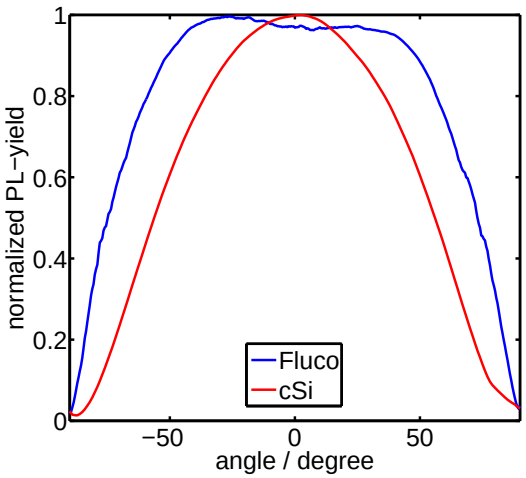

Figure 4.31.: Normalized angular dependence of the spectrally integrated PL yield for different excitation angles and detection under normal incidence for a fluco with Rhodamin 6 G and c-Si. A fluco can absorb diffuse radiation better than e. g. c-Si.

4.3.6. Homogeneity

One requirement for flucos is a flat surface in order to achieve the light trapping by total internal reflection of fluorescence radiation as described in chapter 1.3. To be able to reduce the complexity of the fluco for simulation, the absorption and emission properties should also be homogeneous. It is possible to characterize this homogeneity with the setups described in chapters 3.4.3.2 and 3.4.3.3 on two different lateral resolutions.
On a mm-scale, emission and absorption are recorded with the lateral resolved PL setup with 488 nm excitation from chapter 3.4.3.1. The spectrally integrated PL from a fluco with Rhodamin 6 G in PMMA on a glass substrate in Fig. 4.32 (left) shows some positions with high PL photon flux on a rather homogeneous background. This is also visible in the histogram of the spectrally integrated photon fluxes in Fig. 4.32 (right) where most PL show yields between $2.5 \cdot 10^5$ and $3.5 \cdot 10^5$ counts.

The absorption and emission properties of this fluco are fairly homogeneous except for some positions with a different dye concentration in the PMMA layer or defects on the surface of the fluco which scatter the radiation.

On a µm-scale the AFM image of the fluco in Fig. 4.33 (left) shows dents with a diameter of 3-5 µm and a depth of about $d = 50$ nm. Such dents can lead to scattering and a stronger escape cone loss, because it is possible that radiation above the critical angle for a flat surface has a lower angle of incidence on such dents. Apart from these dents there a scratches on the surface of the fluco, which also result in a non-perfectly flat surface, which is assumed in many theoretical calculations for flucos like [87, 88].
The SNOM measurement of the transmission for $\lambda = 532$ nm in Fig. 4.33 (left: image of the topography, right: transmission) with the setup described in chapter 3.4.3.3 with a SNOM cantilever with a 200 nm aperture also shows the scratches on the surfaces of the fluco with Rhodamin 6 G but also some areas with an equivalent size as the dents in the AFM where the transmission is rather low.
When the SNOM is not used to measure the transmission but the PL emission of the dye for excitation through the 200 nm aperture, only the scratches are observable in the transmission but not the dents as in the AFM (Fig. 4.34 (left) AFM and (right) SNOM in emission mode), since the SNOM cantilever follows the Surface of the fluco. So the dents on the surface do not seem to influence the emission of the dye out of the escape cone but the scratches influence the PL emission. The dents should not be neglected, however, because they can still scatter radiation inside the fluco.

A characterization of a fluco with homogeneous dye concentration with a SNOM is not reasonable, because the high lateral resolution is achieved with an evanescent wave with a dimension below one µm. Thus all dye molecules outside this regime of the evanescent radiation are either not excited or excited by the far field. As a result, a SNOM measurement on a fluco with homogeneous dye concentration with a thickness of $d = 1$ mm yields emission and transmission data, which are a mixture of evanescent and non-evanescent wave propagation. Thus one loses the high resolution of the SNOM.

4.4. Light trapping

The term "light trapping" here means two different things as discussed in 1.2: trapping of the incident radiation (e. g. solar radiation in absorber) or trapping of the radiation inside a fluco.
In this chapter different ways to characterize the application of photonic structures on two different absorbers are presented:
First the application of a photonic structure on the top of a c-Si wafer is discussed. c-Si is often used in solar cells [89] but shows the disadvantage of a rather low quantum efficiency in the infrared regime of the solar radiation (see e. g. the external quantum efficiency of c-Si cells in [58]). One possibility to increase the efficiency of the c-Si solar cells is to trap the infrared radiation

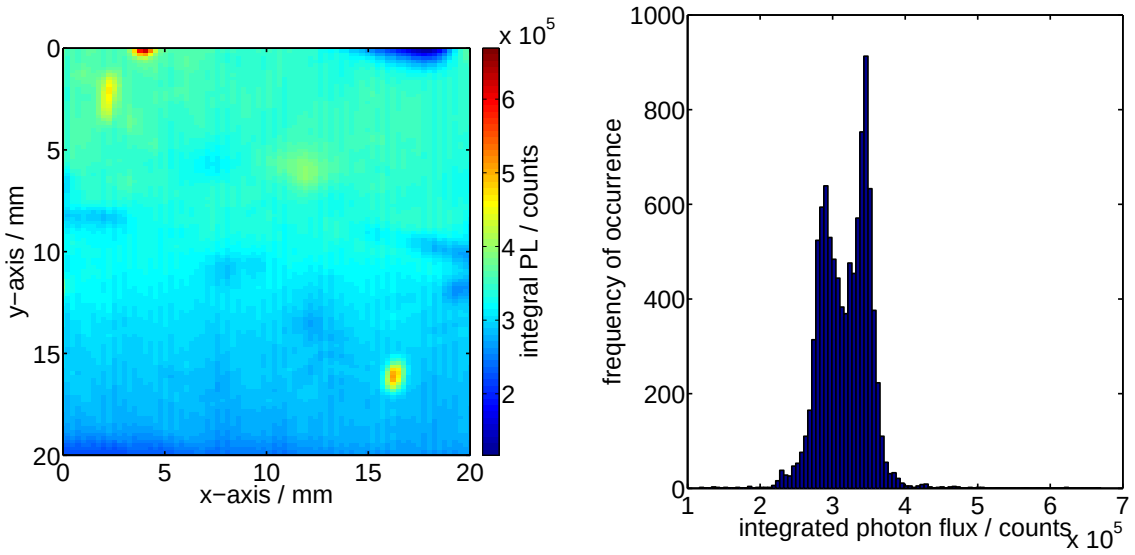

Figure 4.32.: Image of the laterally resolved (mm-scale) and spectrally integrated PL yield of a fluco with Rhodamin 6 G (left) and histogram of the spectrally integrated photon flux (right).

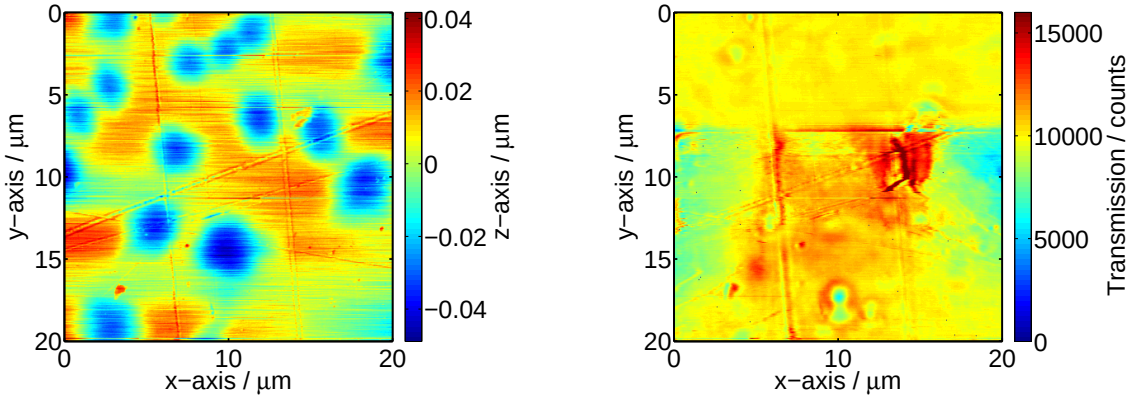

Figure 4.33.: AFM image (left) and SNOM in transmission for the fluco (right) with Rhodamin 6 G in PMMA on glass.

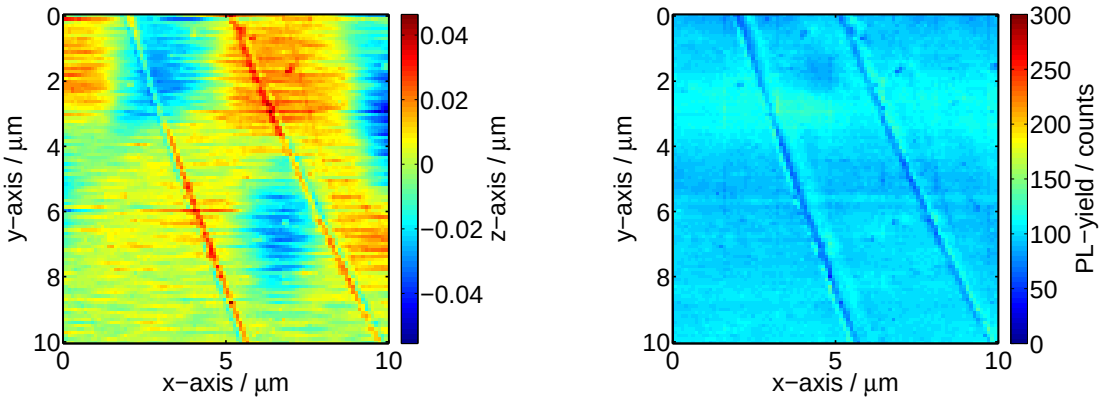

Figure 4.34.: AFM image (left) and SNOM in emission mode (right) for a small area of the fluco in Fig. 4.33 for a fluco with Rhodamin 6 G in PMMA on glass.

inside the absorber to enhance the propagation length of this radiation inside the absorber and thus to enhance the absorption for, by positioning a photonic structure on top of the absorber. The second type of absorber is a fluco, which has the disadvantage of radiative losses from the escape cone. These losses could be reduced by a photonic crystal on top of the fluco, which "reflects" the emitted radiation back into the fluco.

4.4.1. In c-Si

The application of a photonic crystal on c-Si reduces the reemission of radiation with photon energies around and below the band-gap by trapping this radiation inside the absorber and thus to enhance the probability for absorption. One source of radiation with photons with such a photon energy in c-Si is PL radiation as can be seen in Fig. 4.20 (left). The PL radiation is composed of photons with photon energies in the range of 0.95 eV $\leq E_{Ph} \leq$ 1.35 eV which corresponds to wavelengths in the range of 900 nm $\leq \lambda \leq$ 1300 nm. Thus the opal characterized in chapter 4.1 with a stopgap around $\lambda = 1200$ nm is very convenient for the PL emission regarding the light trapping.
Before the discussion of the effect of an opal on the PL emission and on the excitation, it will be shown with a Bragg-mirror what happens when PL radiation is trapped inside a c-Si absorber. Fig. 4.35 (left) shows the direct transmission through the Bragg-mirror which has been used. The Bragg-mirror is an edge filter which reflects the radiation with a photon energy above $E_{Ph} > 1.05$ eV. The upper edge of the reflection band is unknown, since it is in the wavelength regime, where the glass substrate absorbs the radiation.
Attaching a Bragg-mirror to the c-Si wafer on the side of the detection as illustrated in Fig. 4.35 (right) reduces the PL emission as plotted in Fig. 4.36 (left). The PL yield was measured under excitation by a 488 nm laser with a photon flux of $(2.92 \pm 0.13) \cdot 10^{17}$ photons/(cm^{2}s) under normal incidence on one side of the absorber and the detection on the opposite side, either without ("T-without") or with filter ("T-with"). The difference between both emissions agrees

quite well with the transmission of the Bragg-mirror.
Even more important is the PL yield measured in the direction of reflection, which means that both the excitation and the measurement of the PL are performed on the same side of the wafer and in this case the Bragg-mirror is located on the opposite side. The results of this measurement are also plotted in Fig. 4.36 (left) labelled "R-without" and "R-with". Attaching the mirror to the c-Si wafer enhances the photon flux for photons with photon energies below $E_{ph} \leq 1.2$ eV but does not change the PL photon flux for higher photon energies.
The same can be observed in the simulation of the PL emission from a c-Si wafer (as described in the theory) as plotted in Fig. 4.36 (right). Here the emission of the c-Si wafer without attached filter ("without mirror") is plotted as well as the emission with the reflection given by the filter ("with mirror") and with total reflection ("total reflection"). The results of the photon flux for photon energies above $E_{ph} \geq 1.2$ eV are also the same.
Absorption is the reason for this behavior: The emitted PL on the side of the filter is reflected back by the Bragg-mirror and the photons with photon energies above $E_{ph} \geq 1.2$ eV are absorbed on the way to the other surface of the c-Si wafer whereas the photons with lower photon energy are transmitted through the c-Si and leave the absorber on the opposite side and thus enhance the PL emission on that side.
The overall excitation of the c-Si wafer is not noticeably enhanced by the absorption of the reflected PL radiation, because the part of radiative recombination is small compared to the non-radiative recombination, and thus the absorption of the reflected PL photon flux is negligible in comparison to the photon flux of the excitation laser [38]. Consequently the PL photon flux for photon energies above $E_{ph} \geq 1.2$ eV is not influenced by the Bragg-mirror.

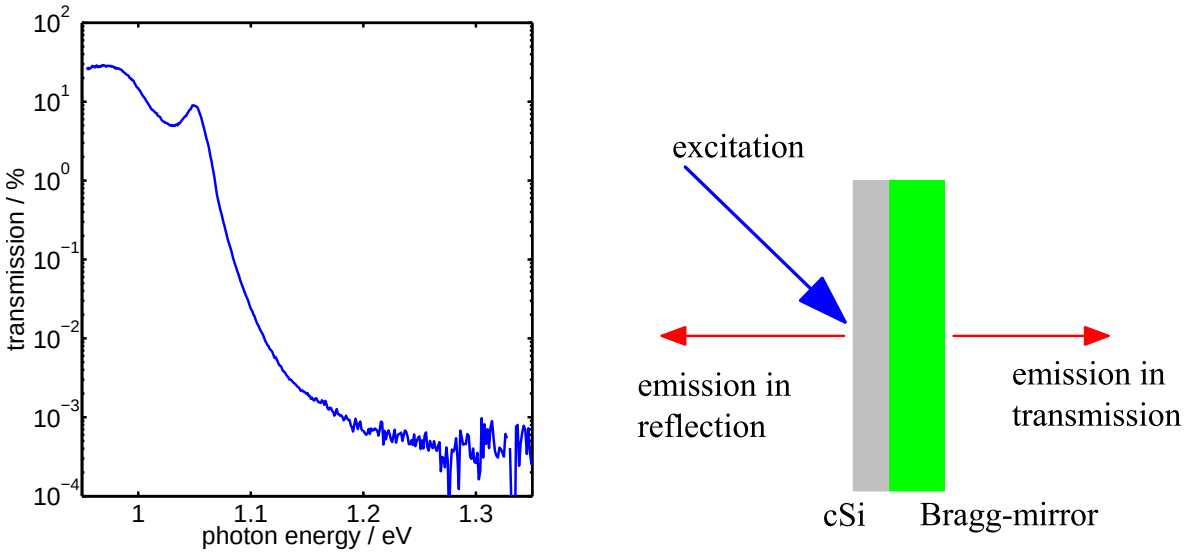

Figure 4.35.: Spectral transmission through a Bragg-mirror (left) and illustration of the application of a Bragg-mirror with 1.05 eV edge wavelength to reduce the PL emission (right).

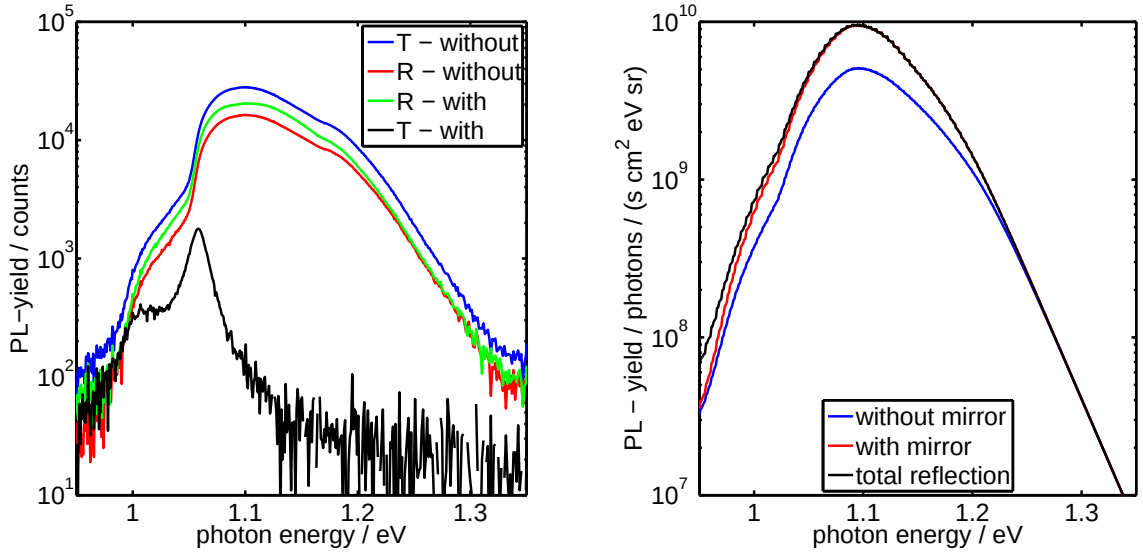

Figure 4.36.: Emission from the top of an excited c-Si wafer with and without Bragg-mirror on top (T: in transmission and T: in reflection, the Bragg-mirror is located on the side of excitation). Comparison of experiment (left) and simulation (right).

4.4.1.1. Absorption enhancement

One possible application of photonic crystals is the enhancement of the absorption for photons with a photon energy for which the absorption coefficient in a semiconductor is so small, that most photons are transmitted and not absorbed. The probability for these photons to be absorbed is enhanced by trapping them inside the semiconductor, so that the propagation length inside the absorber is increased. In this way the absorption of solar photons in e. g. c-Si is enhanced by using a photonic crystal instead of using a thicker absorber.
The simplest way to test this concept is to position a photonic crystal on a semiconductor and to estimate the absorption from transmission and reflection measurements. In this case, a part of the transmitted radiation is reflected by the photonic crystal. This reflected radiation can be absorbed on the way back through the absorber.
Fig. 4.37 (left) shows the calculated absorption of a polished crystalline silicon wafer, of the same wafer with a glass substrate and of the same wafer with an opal with 1200 nm stopgap on glass. There is hardly any influence of the glass substrate observable but the opal slightly enhances the absorption around the stopgap.
Such an application of a photonic crystal is not perfect, because this is not real light trapping: The absorber should be positioned between the photonic crystal and a back reflector in combination with a scatterer to trap the light. But it is possible to verify the effect of the photonic crystal on the absorption.
With a software like SCAPS [90] the theoretical external quantum efficiency (EQE) of a diode (ideal) on the basis of an absorption coefficient has been calculated. To calculate the EQE of the absorptions in Fig. 4.37 (left) for plain c-Si and c-Si with opal, the absorption coefficient is taken

from Green [82] for plain c-Si and the difference in the absorption coefficient between plain c-Si and c-Si with opal is computed from the absorptions in Fig. 4.37 (left).
The results of both EQEs are plotted in Fig. 4.37 (right). Here the EQE is enhanced for photon energies around the stopgap of the opal, the overall solar cell efficiency is increased by 0.3%. This enhancement is quite good compared to the simple system.

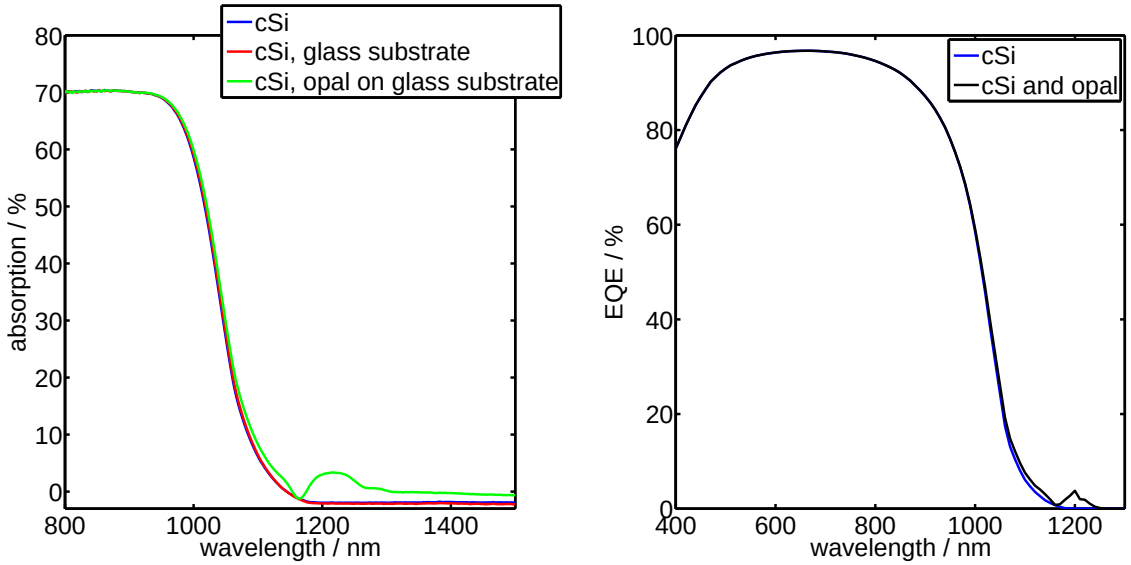

Figure 4.37.: Enhancement of the absorption in crystalline silicon with an opal on glass substrate with a stopgap at $\lambda_{\text{stop}} = 1200$ nm (left) and calculated EQE for a c-Si solar cell with the absorption coefficient from the left diagram (right).

4.4.1.2. Effect of an opal on emission from the top

In this chapter it will be discussed how well an opal with $\lambda_{\text{stop}} = 1200$ nm stopgap can reduce the spectrally and angular dependent PL emission from an excited c-Si wafer. Fig. 4.38 shows an illustration of the experiment: A c-Si absorber is excited under normal incidence with a 488 nm laser with a photon flux of $(2.92 \pm 0.13) \cdot 10^{17}$ photons $\text{cm}^{-2}\text{s}^{-1}$ on one side of the absorber. On the opposite side the PL emission of the c-Si is collected under various detection angles with either a glass substrate on top of the c-Si absorber or an opal with $\lambda_{\text{stop}} = 1200$ nm stopgap on a glass substrate on top of the absorber. The comparison of the emission with glass substrate and opal on glass substrate is done so that one can neglect the effect of the glass substrate (as mentioned in chapter 3.6), measure both emissions on the same spot of the c-Si wafer and ignore the c-Si inhomogeneities.
The PL emissions of an c-Si absorber without ($\Gamma(\alpha, \lambda)$) and with opal ($\Gamma_{\text{with}}(\alpha, \lambda)$) are plotted in Fig. 4.39. The emission without opal is known from chapter 4.2.3 and one can clearly see that the opal with a stopgap of $\lambda_{\text{stop}} = 1200$ nm reduces the PL emission inside the stopgap: For a detection angle φ of 0° the emission is reduced at $\lambda = 1200$ nm. The reduction by the opal shifts

to smaller wavelengths with increasing absolute value of the detection angle $|\varphi|$ and reaches a wavelength of $\lambda = 1000$ nm at $|\varphi| = 50°$ due to the blue shift described in chapter 4.1.2.
A computation of the ratio of the PL with and without opal

$$\chi(\alpha, \lambda) = \frac{\Gamma_{with}(\alpha, \lambda)}{\Gamma(\alpha, \lambda)}, \tag{4.10}$$

depicted in Fig. 4.40 (left), shows the relative reduction of the PL emission. Inside the stopgap, the PL emission is reduced to approximately 50% and the overall emission is reduced to 78%.
A simulation of the PL reduction by an opal of ten layers of PMMA nanospheres with a diameter of $D = 540$ nm is plotted in Fig. 4.40 (right), which agrees quite well with the experimental results regarding the spectral shape of the PL reduction.

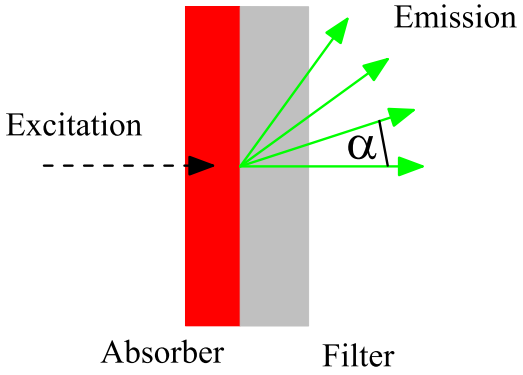

Figure 4.38.: Sketch of the measurement for the characterization of the influence of an opal on the top emission.

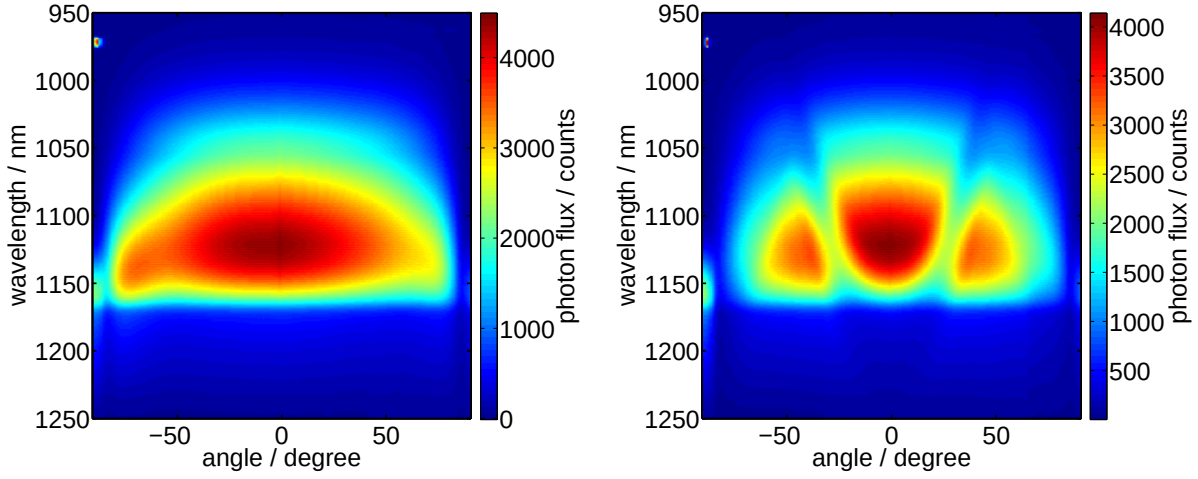

Figure 4.39.: Angular and spectrally resolved top emission from c-Si with glass on top (left) and from c-Si with glass and $\lambda_{\text{stop}} = 1200$ nm stopgap opal on top (right).

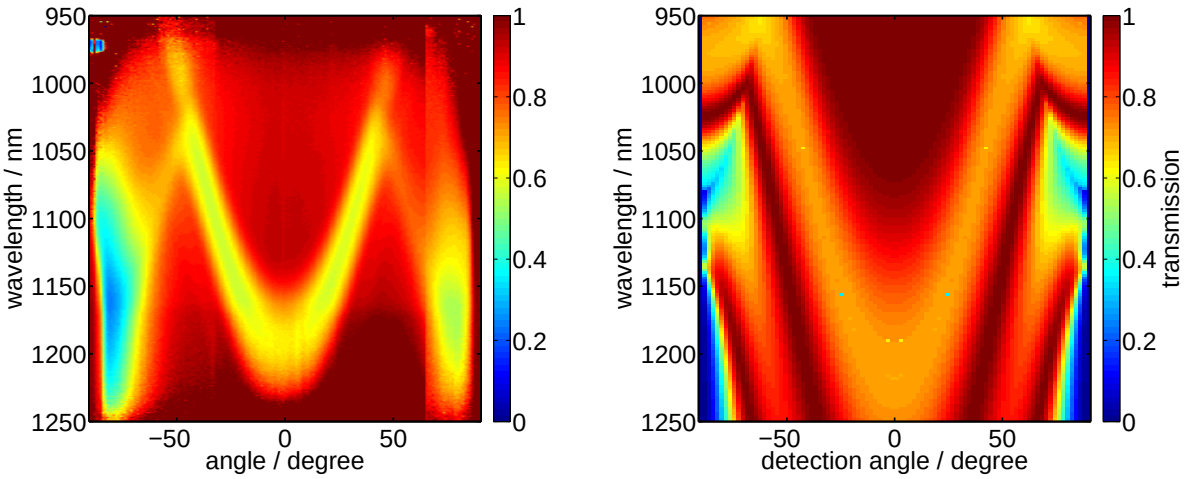

Figure 4.40.: Ratio $\chi(\alpha, \lambda)$ of emission with glass substrate and opal to PL emission with only a glass substrate from experiment (left) and theory (right).

4.4.1.3. Effect on the excitation

A perfect photonic structure designed for the trapping of solar radiation inside an absorber should have no influence on the excitation so that the incident direct sunlight (perpendicular to the surface) is not reduced on the way to the absorber. To characterize the effect of an opal on the incident light the influence on the angular dependent excitation through the opal was measured. To this end a c-Si wafer was excited through the opal with $\lambda_{\text{stop}} = 1200$ nm stopgap on glass under various excitation angles and the PL was recorded under normal incidence on the opposite side of the c-Si wafer as illustrated in Fig. 4.41 (left).
The results of these measurements (one for different excitation angles through glass, index matching gel ($\Gamma_{\text{glass}}(\lambda, \alpha)$) and one for the measurement with excitation through the opal ($\Gamma_{\text{opal}}(\lambda, \alpha)$) where also characterized as before in terms of the influence of the opal on the PL emission by the ratio

$$\chi = \frac{\Gamma_{opal}(\lambda, \alpha)}{\Gamma_{glass}(\lambda, \alpha)}. \tag{4.11}$$

This fraction is plotted for the opal with $\lambda_{\text{stop}} = 1200$ nm stopgap in Fig. 4.41 (right). This ratio amounts to about 0.5, meaning that the emission is reduced by a factor of two, which results from the reduced transmission through the opal (see chapter 4.1.1) resulting from the strong backscattering of the excitation laser photons ($\lambda = 488$ nm).
A beneficial effect emerges: The excitation through the opal is nearly independent of wavelength and angle.
The influence of an opal on the incident radiation however, shows the drawback for applications on top of solar cells by strong reflection / backscattering that exceeds the beneficial effect of light trapping. The opal however, can be used e. g. as an intermediate reflector in tandem solar cells [91], where backscattering is no problem, because the scattered radiation keeps still inside the absorber.

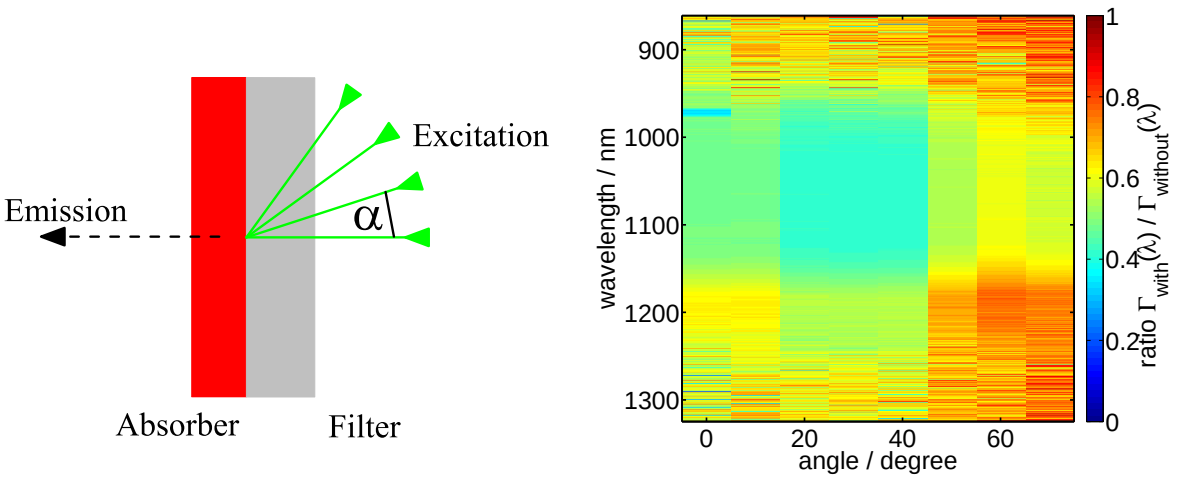

Figure 4.41.: Sketch of the measurement of the angular dependent excitation (left) and ratio of the PL emission from c-Si with opal ($\Gamma_{\text{with}}(\lambda)$) and without opal ($\Gamma_{\text{without}}(\lambda)$) between excitation source and sample (right).

4.4.2. In a fluco

The influence of a photonic crystal on a fluco will is slightly different from the one on c-Si, because the ratio of radiative to non-radiative emission is much higher in a fluco than in c-Si, e. g. Rhodamin 6 G has a quantum efficiency > 0.9 [92]. As the goal is to reduce the top emission and thus to enhance the photon flux at the edge of the fluco for the application of photonic crystals on top of flucos, the edge emission is of much greater interest than in the application of photonic crystals on c-Si.

4.4.2.1. Effect on emission from the top

The measurement of the reduction of the emission with opal on top of the fluco is the same as in chapter 4.4.1.2 for a c-Si wafer: Same setup, same excitation etc. with similar results but for a fluco with Rhodamin 6 G in PMMA on glass and an opal with $\lambda_{\text{stop}} = 580$ nm stopgap on a glass substrate[1]. Fig. 4.42 illustrates the emission without (left) and with (right) opal and Fig. 4.43 (left) shows the ratio of the emission with opal and without opal.
This photonic structure reduces the emission of PL radiation even stronger. The emission inside the stopgap is reduced to 20% and the overall emission to 47.5%. A reason that the opal with smaller PMMA nanospheres yields better results may be the quality of the spheres:
An opal with $\lambda_{\text{stop}} = 1200$ nm stopgap needs spheres with diameter $D = 540$ nm and an opal with $\lambda_{\text{stop}} = 580$ nm spheres with $D = 270$ nm. If both sphere diameters show the same standard deviation ΔD (in % of D) the absolute error of the stopgap wavelength $\Delta\lambda$ is given by

$$\Delta\lambda = \left| \frac{\partial}{\partial D} \frac{\sqrt{2}D}{0.658} \right| \Delta D = \frac{\Delta D \sqrt{2}}{0.658}. \tag{4.12}$$

[1]Note: Also comparison of fluco with glass substrate on top and fluco with glass substrate and opal on top and according refractive index matching.

For spheres with $D = 540$ nm the absolute error $\Delta\lambda$ is larger than for $D = 270$ nm, since ΔD is proportional to the sphere diameter D.
The second reason is the weight of the spheres: Our samples were made by dip-coating by J. Üpping at MLU[2] Halle from a solution of PMMA nanospheres in water. The bigger spheres are heavier than the small ones and thus in the solution they decline faster to the bottom of the beaker which could also reduce the opal quality.
A third reason could be the production of the spheres: L. Steidl at the University of Mainz produced the nanospheres for the opals by growing them. But to grow the spheres with $D = 540$ nm diameter two growing steps are needed in comparison to the growing of the spheres with $D = 270$ nm diameter which only need one step. Thus the error of the sphere diameter is larger for the big spheres because of the second step, so the error of the stopgap wavelength is increased more.

The same measurement and calculation of the PL emission can be done with a Bragg-mirror instead of the opal on top of the fluco. Fig. 4.43 (right) shows the ratio according to eq. (4.12) of the emitted PL photon flux with Bragg-mirror (550 nm edge filter) and the emission without filter. Here the edge of the filter transmission can clearly be observed and shifts to smaller wavelengths with increasing absolute detection angle $|\theta|$ because of the Bragg effect which is the same as for the opals.
This filter reduces the emission up to 0% and the overall emission to only 3.0%, but this kind of filter does not provide the possibility of an angular dependence as e. g. an opal in $\Gamma - X$-direction.

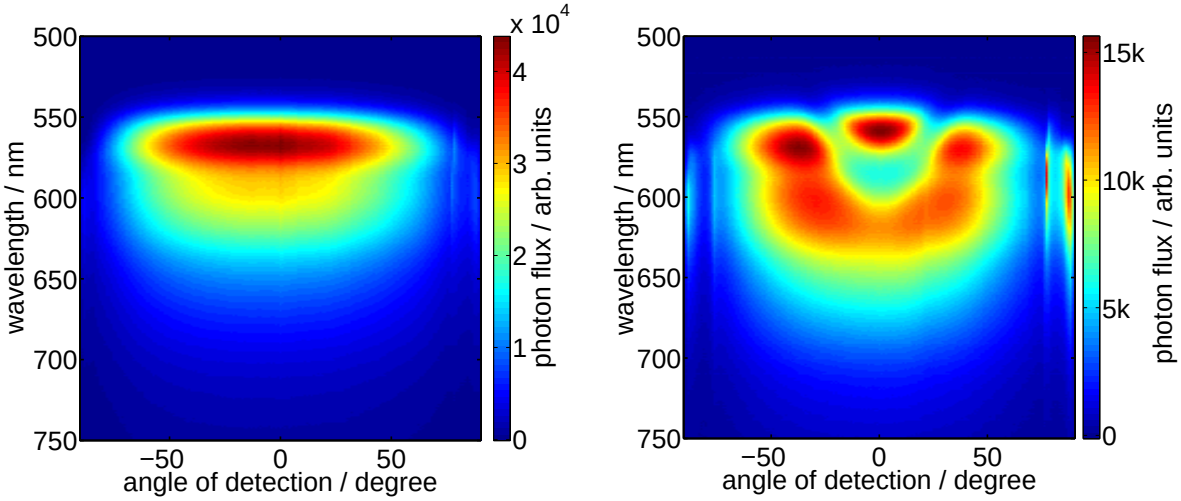

Figure 4.42.: Angular and spectrally dependent top emission from a fluco (Rhodamin 6 G) with glass (left) and from the fluco with glass and $\lambda_{\text{stop}} = 580$ nm stopgap opal on top (right).

[2]Martin-Luther-Universität Halle-Wittenberg.

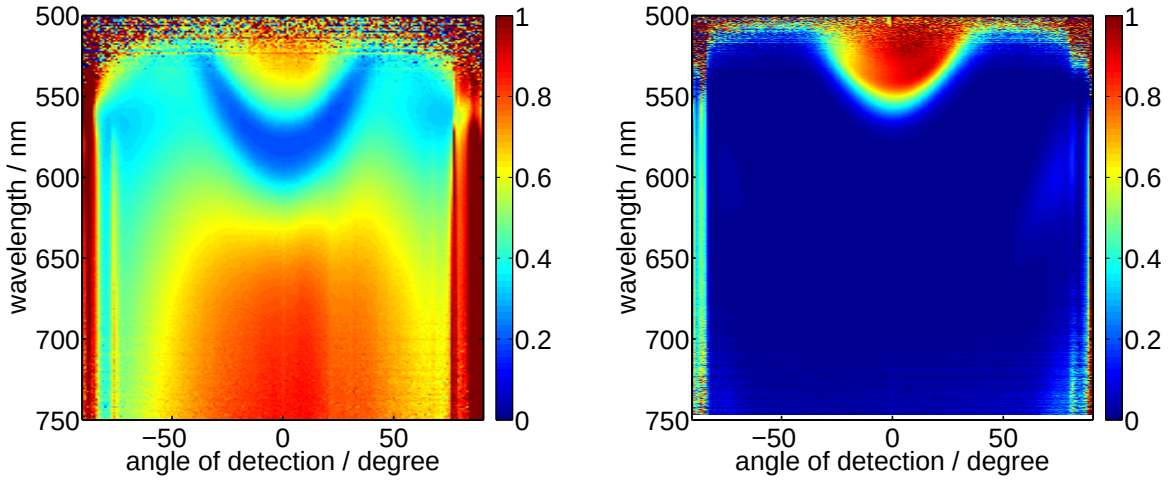

Figure 4.43.: Ratio of the PL emission with photonic structure to that without photonic structure for the opal (left) and a Bragg-mirror with 550 nm edge (right).

4.4.2.2. Effect on the edge emission

The impact of photonic structures on the edge emission is discussed in chapter F.

4.4.2.3. Effect on excitation

The influence of the filter on the excitation of a fluco is characterized in the same way as in chapter 4.4.1.3 for c-Si: Excitation with a 488 nm laser with $d = 1.1$ mm diameter through the photonic structure under various angles of incidence with rotation axis on the top of the fluco and detection on the opposite side under normal incidence (compare Fig. 4.41 (left)). The results for the emission for different excitation angles in comparison to the emission without photonic structure on the side of the excitation are plotted in Fig. 4.44 for the opal with 580 nm stopgap (left) and for the low-pass filter with 550 nm edge (right).
The result for the opal is nearly the same as before for the opal with 1200 nm stopgap, because this opal also scatters the incident radiation back, so that the emitted photon flux is smaller with the opal than without it and there is no real angular and spectral dependence observable.
A better result can be observed for the low-pass filter with 550 nm edge. Here the ratio (compare eq. (F.1)) of the emission with filter and without filter is greater than one for a wavelength $\lambda > 550$ nm, because the emitted light in the escape cone is reflected back by the filter and leaves the fluco on the opposite side (side of detection). For $\lambda < 550$ nm the ratio χ is below one, because the filter has only a transmission of the excitation below 80% (compare Fig. F.3). The ratio χ approaches zero, however, above a critical angle, because due to the blue-shift described in chapter 4.1.2 the edge wavelength of the low-pass filter reaches the excitation wavelength (488 nm) and reflects all radiation back, so that the fluco is not excited.

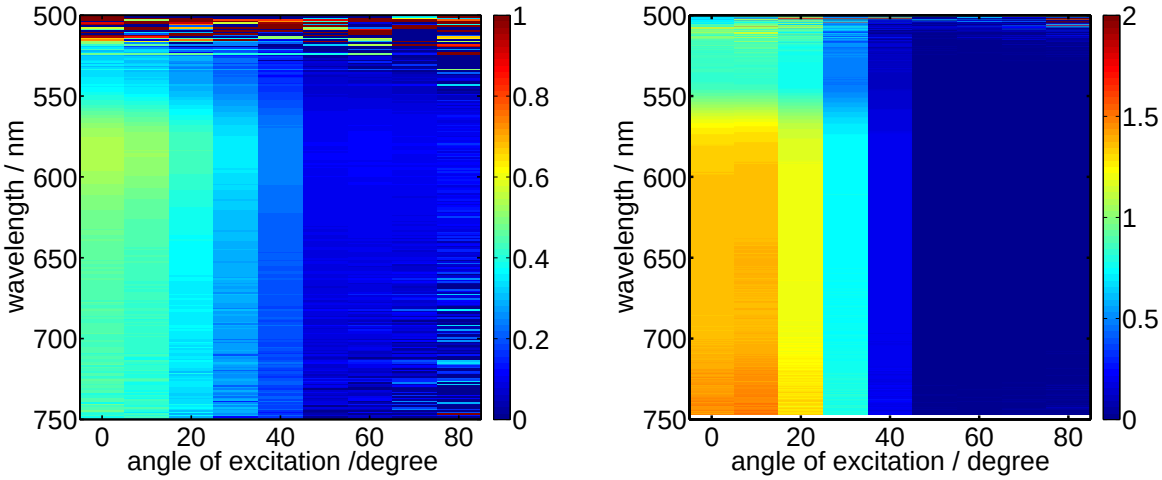

Figure 4.44.: Effect of the photonic structure on the excitation of a fluco for a 580 nm stopgap opal (left) and for a 550 nm low-pass filter (right).

5. Summary, conclusion and outlook

In this thesis results of different experiments were presented (e. g. angular dependent photoluminescence) to characterize the propagation of electro-magnetic radiation inside and out of absorbers using the examples of crystalline silicon and fluorescence collectors with and without manipulation of the in- and out-coupling of the radiation by photonic structures (opal and edge filters). Experimental results were compared with results from simulations of the propagation of radiation, which are based on the fundamental equations for the properties of electro-magnetic radiation like reflection, transmission, absorption or phase accumulation.
The source of the radiation either was an external light source like a laser or photoluminescence radiation from an excited absorber, which is described by Planck's generalized law.
In the case of semiconductors the photoluminescence is governed by the recombination of excess carrier concentration which is strongly influenced by the properties of the semiconductor. Results of the simulation of the photoluminescence for different excess carrier concentration depth profiles clearly indicate that the spectral shape of the emitted radiation is governed strongly by the depth profile of the excess carrier concentration, which must be considered in the evaluation of parameters from photoluminescence measurements. Here magnitudes, such as parameters of the absorption coefficient $\alpha(E_{Ph})$, surface recombination velocities S_0 and S_d, and excess carrier lifetime are of major importance; the influence of these parameters on the excess carrier concentration and the spectral photoluminescence were discussed conversely.
Fluorescence concentrators show two different options for the propagation of radiation:

- the emitted radiation propagates from the fluorescence dye to the edge of the concentrator, where a solar cell is attached
- the radiation leaves the concentrator through the top and bottom surfaces and is lost from the system.

Both kinds of propagation of radiation were simulated and experimentally recorded. The experimental data provides means to estimate loss effects due to reabsorption and scattering of photoluminescence photons in fluorescence collectors.
Results from simulations and experiments show that the edge emission is anisotropic regarding the emission angle and depends strongly on the position of the excitation of the fluorescence collector and on the emission depth profile, governed by the dye concentration: a higher dye concentration leads to a stronger dye emission close to the excitation surface and thus to a more anisotropic edge emission. A comparison of the emission depth profile and the efficiency of the fluco allows for optimization of the edge emission in terms of dye concentration.

The in- and out-coupling of the electro-magnetic radiation in both types of absorbers are to be manipulated to enhance the absorption of the incident radiation (e. g. for crystalline silicon) and/or to reduce the emission of photoluminescence radiation out of the absorber (e. g. for fluorescence concentrators to enhance the edge emission).
Both types of photonic crystals mentioned above were characterized to specify the quality of the reduction of the reemission, the influence on the incident radiation in the case that the photonic crystal is on top of the absorber and the influence of the edge mirror on the enhancement of the edge emission of the fluorescence collector.
It was shown that (spectral and spatial) reflection, transmission and photoluminescence emission measurements yield results, to characterize the quality of the photonic structures and the absorption enhancements of absorption by several percent and for a reduction of the emission of up to 100%.
A discussion of the enhancement of the edge emission with the edge filter includes possible influences of different designs for the fluorescence collector. It is not preferable to locate a photonic crystal with glass substrate directly on top of the concentrator, because the fundamental concept to trap light by total internal reflection is counterbalanced by the influence of the refractive index of the glass substrate of the photonic structure.
A great disadvantage of photonic structures is the influence on the incident radiation. Especially the opal shows a strong scattering of the incident radiation which reduces the overall efficiency of a solar cell by 50% when located on top of the solar cell. Consequently the system of photonic crystal and absorber has to be designed in such a way that the scattered radiation is also absorbed.
One possibility is to stack various fluorescence concentrators on top of one another and to position different types of opals between these as depicted in Fig. 5.1. Such a “tandem” or “multispectral” design is based on: Flucos with different dyes and respective absorptions are stacked on top of one another, so that the radiation scattered by the opal on a fluco is absorbed by the fluco above but the opal still traps the radiation emitted by the dye inside the fluco. Thus the guided radiation inside the fluco should be enhanced and the losses due to the scattering of the incident radiation by the opal should be reduced. The solar cells attached to edges of the flucos should have a band-gap corresponding to the emitted radiation.

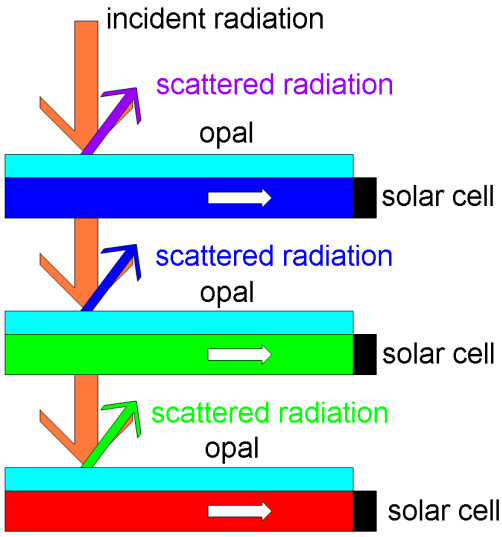

Figure 5.1.: Schematic design of a multi-spectral fluco system with opals. Flucos with dyes for different absorption wavelengths are stacked with opals with a stopgap according to the fluco between them. In this way the radiation scattered by a fluco is still inside another fluco. The flucos guide the trapped radiation to an attached solar cell with corresponding band-gap.

6. Zusammenfassung

In dieser Arbeit werden Ergebnisse verschiedener experimenteller Aufbauten (z. B. winkelabhängige Photolumineszenz) vorgestellt um die Propagation von elektromagnetischer Strahlung innerhalb und ausserhalb von Absorber am Beispiel von kristallinem Silizium und Fluoreszenzkollektoren mit und ohne Manipulation der Ein- und Auskopplung der Strahlung durch photonische Strukturen (Opal und Kantenfilter) zu charakterisieren. Die experimentellen Ergebnisse von diesen Aufbauten und Proben werden mit den Ergebnissen der Simulation der Propagation von Strahlung verglichen, welche auf den grundlegenden Gleichungen für die Propagation elektromagnetischer Strahlung wie Reflektion, Transmission, Absorption und Phasenansammlung beruhen Die Strahlungsquelle ist entweder eine externe Lichtquelle wie ein Laser oder Photolumineszenz Strahlung von einem angeregten Absorber, welche durch das verallgemeinerte Plancksche Strahlungsgesetzt beschrieben wird.
Im Fall von Halbleitern wird die Photolumineszenz Strahlung durch die Rekombination von Überschussladungsträgern verursacht, welche stark durch die Eigenschaften des Halbleiters beeinflusst wird. Ergebnisse der Simulation der emittierten Photolumineszenz für verschiedene Überschussladungsträgertiefenprofile zeigen deutlich, dass die spektrale Abhängigkeit der emittierten Strahlung deutlich durch das Profil der Überschussladungsträger beeinflusst wird. Dieser Einfluss muss bei der Auswertung der Ergebnisse von Messungen der Photolumineszenz berücksichtigt werden. Hierbei sind insbesondere der Absorptionskoeffizient $\alpha(E_{Ph})$, die Oberflächenrekombinationsgeschwindigkeiten S_0 und S_d und die Lebensdauer der Überschussladungsträger von beträchtlich Bedeutung. Daher wird der Einfluss dieser Parameter auf die spektrale Photolumineszenz diskutiert.
Fluoreszenzkollektoren zeigen zwei verschiedene Strahlungspropagationen: Zum einen propagiert die emittierte Strahlung von dem Fluoreszenzfarbstoff zur Kante des Kollektors, wo eine Solarzelle angebracht ist um die Strahlung in elektrische Energie zu wandeln, zum anderen verlässt die Strahlung den Kolkletor durch die obere und untere Oberfläche wodurch sie für das System verloren ist. Beide Arten der Ausbreitung der Strahlung wurden simuliert und gemessen. Sie bieten die Möglichkeit, die Verlussteffekte durch Reabsorption und Streuung abzuschätzen. Dies sollte in anderen Arbeiten noch detaillierter untersucht werden.
Die Ergebnisse der Simulationen und Messungen zeigen, dass die Emission an der Kante nicht isotropisch ist, sondern stark von der Position der Anregung auf der Oberfläche des Fluoreszenzkollektors und dem Tiefenprofiel der Emission abhängt, welches durch die Konzentration des Farbstoffes beeinflusst wird: Eine hohe Konzentration des Farbstoffes führt zu einer starken Emission in der Nähe der Oberfläche, an der angeregt wird, und dadurch zu einer ziemlich anisotropen Emission an der Kante. Das Emissionstiefenprofiel sollte in weiteren Arbeiten noch mit

der Effizienz des Fluoreszenzkollektors vergleichen werden um Zugriff auf das ideale Tiefenprofil der Emission zu erhalten.

Die Ein- und Auskopplung von elektromagnetischer Strahlung in beide Absorber soll manipuliert werden, um die Absorption der einfallenden Strahlung (z. B. bei kristallinem Silizium) zu erhöhen oder die Reemission von Photolumineszenz Strahlung aus einem Absorber heraus zu reduzieren (z. B. um die Emission an der Kante bei Fluoreszenzkonzentratoren zu erhöhen). Beide Arten von photonischen Kristallen, die oben genannt wurden, werden hinsichtlich der Qualität der Reduktion der Reemission, dem Einfluss auf die einfallende Strahlung in dem Fall dass der photonische Kristall auf dem Absorber positioniert ist und in dem Fall des Kantenfilters auf die Verbesserung der Emission an der Kante des Fluoreszenzkollektors charakterisiert.
Es wird gezeigt, dass (spektrale und räumliche) Reflektion, Transmission und Photolumineszenz Messungen Ergebnisse liefern, welche ausreichen, die Qualität der photonischen Strukturen zu charakterisieren und dass die Absorption um einige Prozentpunkte erhöht werden kann bzw. die Reemission um bis zu 100% reduzieren werden kann. Die Diskussion der Verbesserung der Kantenemission durch den Kantenfilter beinhalten mögliche Einflüsse von verschiedenen Designs des Fluoreszenzkollektors. Eine Positionierung eines photonischen Kristalles mit Glassubstrat direkt auf dem Kollektor ist nicht sinnvoll, denn das fundamentale Konzept die Strahlung durch totale innere Reflektion einzusperren wird durch das Glassubstrat beeinflusst.
Ein fundamentaler Nachteil von photonischen Strukturen ist die Beeinflussung der einfallenden Strahlung. Vor allem der Opal weist eine besonders starke Streuung der einfallenden Strahlung auf, z. B. kann ein Opal die Effizienz einer Solarzelle um 50% reduzieren, wenn er auf der Solarzelle positioniert wird. Diese Eigenschaft ist desaströs für viele Anwendungen. Daher sollte ein System aus photonischem Kristall und Absorber so aufgebaut sein, dass die gestreute Strahlung ebenfalls absorbiert wird.
Eine Möglichkeit ist es, mehrere Fluoreszenzkollektoren übereinander zu stapeln und verschiedene Opale zwischen diesen zu legen, wie es in Abb. 6.1 gezeigt wird. Solch ein “Tandem” oder “multispektrales” Design beruht auf folgender Idee: Fluoreszenzkollektoren mit verschiedenen Farbstoffen und zugehörigen Absorptionen werden aufeinander gestapelt, so dass die Strahlung, die durch einen Opal gestreut wird, durch den Fluoreszenzkollektor oberhalb des Opals absorbiert wird und der Opal die Strahlung die vom Farbstoff emittiert wird innerhalb des Fluoreszenzkollektor einsperrt. Dadurch wird die Strahlung innerhalb des Fluoreszenzkollektors verstärkt und die Verluste durch die Streuung der einfallenden Strahlung durch den Opal werden reduziert. Die Solarzelle an der Kante des Fluoreszenzkollektors sollte eine Bandlücke aufweise, die zu der emittierten Strahlung des Fluoreszenzkollektors passt.

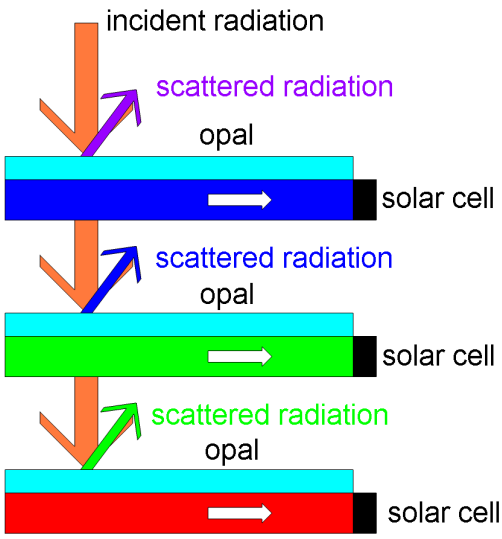

Abbildung 6.1.: Mögliches Design eines multispektralen Fluoreszenzkollektorsystems mit Opalen. Fluoreszenzkollektoren mit Farbstoffen für verschiedene Absorptionswellenlängen werden mit passenden Opalen dazwischen übereinander gestapelt. Auf diese Weise wird die Strahlung, die von dem Opal gestreut wird, von einem Fluoreszenzkollektor absorbiert. Die Fluoreszenzkollektoren leiten die eingesperrte Strahlung zu einer Solarzelle an der Kante, welche eine passende Bandlücke besitzt.

Bibliography

[1] F. Hallermann, C. Rockstuhl, S. Fahr, G. Seifert, S. Wackerow, H. Graener, G. v. Plessen, F. Lederer, "On the use of localized plansmon polaritions in solar cells", phys. stat. sol (a) **205**, 2844-2861 (2008).

[2] http://mikromd.physik.uni-halle.de/nanovolt/, last time called November 2010.

[3] C. Ulbrich, S. Fahr, J. Üpping, M. Peters, T. Kicherartz, C. Rockstuhl, R.B. Wehrspohn, A. Gombert, F. Lederer, U. Rau, "Directional selectivity and ultra-light-trapping in solar cells", phys. stat. sol (a) **205**, 2831-2843 (2008).

[4] M. Kroll, S. Fahr, C. Helgert, C. Rockstuhl, F. Lederer, T. Pertsch, "Employing dielectric diffractive structures in solar cells - a numerical study", phys. stat. sol (a) **205**, 2777-2795 (2008).

[5] B. Ahrens, P. Löper, J.C. Goldschmidt, S. Glunz, B. Henke, P.T. Miclea, S. Schweizer, "Neodymium-doped fluorochlorozirconate glasses as an upconversion model system for high efficiency solar cells", phys. stat. sol (a) **205**, 2822-2830 (2008).

[6] K. Baumgartner, B. Ahrens, O. Angelov, M. Sendova-Vassileva, D. Dimova-Malinovska, B. Holländer, S. Schweizer, R. Carius, "Photon Down-Conversion in Terbium (III)-doped Thin Dielectric Films and Fluorozirconate Glasses for Thin Film Solar Cells", Proceedings of SPIE : Photonics for Solar Energy Systems III, / ed. R.B. Wehrspohn, A. Gombert, Vol. 7725. S. 77250T (2010).

[7] http://rredc.nrel.gov/solar/spectra/am1.5/, last time called: November 2010.

[8] G. Kirchhoff, "Über das Verhältnis zwischen dem Emissionsvermögen und dem Absorptionsvermögen der Körper für Wärme und Licht", Poggendorfs Annalen der Physik und Chemie **109**, 275-301 (1860).

[9] E.D. Palik, "Handbook of Optical Constants of Solids", San Diego, illustrated edition, Academic Press Inc. (1997).

[10] W. Shockley, H.J. Queisser, "Detailed balance limit of efficiency of p-n junction solar cells", J. Appl. Phys. **32**, 510-519 (1961).

[11] M.J. Kerr, A. Cuevas, P. Campbell, "Limiting efficiency of crystalline silicon solar cells enhanced to Coulomb-enhanced auger recombination", Prog. Photovolt: Res. Appl. **11**, 97-104 (2003).

[12] M.A. Green, "Third Generation Photovoltaics: advanced solar energy conversion", Berlin, Sringer (2003).

[13] S. Fahr, C. Ulbrich, T. Kirchartz, U. Rau, C. Rockstuhl, F. Lederer, "Rugate filter for light-trapping in solar cells", Optics express **16**, 9332-9343 (2008).

[14] E. Yablonovitch, "Statistical ray optics", J. Opt. Soc. Am. **72**, 899-907 (1982).

[15] M. A. Green, "Lambertian light trapping in textured solar cells and light-emitting diodes: analytical solutions", Prog. Photovolt: Res. Appl. **10**, 235-241 (2002).

[16] P. Bermel, C. Luo, L. Zeng, L. C. Kimerling, J. D. Joannopoulos, "Improving thin-film crystalline silicon solar cell efficiencies with photonic crystals", Opt. Express **15**, 16986-17000 (2007).

[17] L. Zeng, Y. Yi, C. Hong, J. Liu, N. Feng, X. Duan, L. C. Kimerling, B. A. Alamariu, "Efficiency enhancement in Si solar cells by textured photonic crystal back reflector", Appl. Phys. Lett. **89**, 111111 (2006).

[18] A. Luque, G.L. Araujo, "Physical limitations to photovoltaic energy conversion", chapter "Optical confinement in photovoltaics", pp. 50-83, Adam Hilger, Bristol, England (1990).

[19] M. Peters, J.C. Goldschmidt, P. Loeper, B.Bläsi, G. Willeke, "Lighttrapping with angular selective filters", Proceeding of 23rd European Photovoltaic Solar Energy Conference and Exhibition, Valencia, Spain, WIP Renewable Energies, Munich, 354-359 (2008).

[20] K.R. Lang, "Sun, Earth and Sky", Berlin, 1. Edition, Springer (1995).

[21] P. Campbell, "Enhancement of light absorption from randomizing and geometric textures", JOSA B **10**, 2410-2415 (1993).

[22] P. Campbell, M. A. Green, "Light trapping properties of pyramidally textured surfaces", J. Appl. Phys. **62**, 243-249 (1987).

[23] S. Fahr, C. Rockstuhl, F. Lederer, "Engineering the randomness for enhanced absorption in solar cells", Appl. Phys. Lett. **92**, 171114 (2008).

[24] W.H. Weber, J. Lambe, "Luminescent greenhouse collector for solar-radiation", Appl. Opt. **15**, 2299-2300 (1976).

[25] V. Wittwer, W. Stahl, A. Goetzberger, "Fluorescent planar concentrators", Sol. Energy Mater. **11**, 187-197 (1984).

[26] J.S. Batchelder, "The luminescent solar concentrator", PhD thesis, California Institute of Technology, Pasadenda, California (1982).

[27] P. Würfel, "Physics of Solar Cells: From Principles to New Concepts", Wiley-VCH, Weinheim (2005).

[28] K. Schick, E. Daub, S. Finkbeiner, P. Würfel, "Verification of a generalized Planck law for luminescence radiation from silicon solar-cells", Appl. Phys. Lett A **54**, 109-114 (1992).

[29] G. Smestad, H. Ries, "Luminescence and current voltage characteristics of solar-cells and optoelectronic devices", Sol.En.Mat. and Solar Cells **25**, 51-71 (1992).

[30] T.J.J. Meyer and T. Markvart, "The chemical potential of light in fluorescent solar collectors", J. Appl. Phys. **105**, 063110 (2009).

[31] L. Gütay, G.H. Bauer, "Analysis of Band Gap Fluctuations in Cu(In, Ga)Se2 by Confocal Optical Transmission and Photoluminescence", Mater. Res. Soc. Symp. Proc. Materials Research Society Vol. **1012**, Y08-03 (2007).

[32] G.H. Bauer, R. Brüggemann, S. Tardon, S. Vignoli, R. Kniese, "Quasi-Fermi level splitting and identification of recombination losses from room temperature luminescence in $Cu(In_{1-x}Ga_x)Se_2$ thin films versus optical band gap", Thin Solid Films **480**, 410-414 (2005).

[33] L. Gütay, "Konfokale Photolumineszenz von Cu(In,Ga)Se2 - Charakterisierung optoelektronischer Eigenschaften mit lateraler Sub-Mikrometer-Auflösung", PhD thesis at Carl von Ossietzky Universität Oldenburg (2008).

[34] Finkbeiner S, Daub E, Würfel P, "Maximum open-circuit voltage for solar-cell silicon from absolute intensities of photoluminescence", Proceedings of the 11th E.C. Photovoltaic Solar Energy Conference Montreux, Switzerland, WIP Renewable Energies, Munich, 320-324 (1992).

[35] E. Hecht, "Optik", München, 5th edition, Oldenbourg (2009).

[36] M. Born, "Principles of optic", Oxford, 5th edition, Pergamon Press (1975).

[37] http://www.mathworks.de/, last time called: June 2010.

[38] T. Jürgens, L. Gütay, G.H. Bauer, "Photoluminescence, open circuit voltage, and photocurrents in Cu(In,Ga)Se-2 solar cells with lateral submicron resolution", Thin Solid Films **511**, 678-683 (2006).

[39] P. Würfel, "The chemical potential of radiation", J. Phys. C **15**, 3967-3985 (1982).

[40] Hendrik Sträter, "Winkel- und spektralabhängige Emission von Fluoreszenzkollektoren", Masterthesis, Carl von Ossietzky University, Oldenburg (2010).

[41] J.C. Goldschmidt, "Novel solar cell concepts", PhD thesis, Universitiy Konstanz, Konstanz (2009).

[42] A. Zastrow, "Physikalische Analyse der Energieverlustmechanismen in Fluoreszenzkollektoren", PhD thesis, University of Freiburg, Freiburg (1981).

[43] H. Sträter, S. Knabe, G.H. Bauer, "Spectrally and angle resolved emission of a thin film fluorescence collector", to be published.

[44] S. Knabe, L. Gütay, G.H. Bauer, "Interpretation of quasi-Fermi level splitting in Cu(Ga,In)Se-2-absorbers by confocally recorded spectral luminescence and numerical modeling", Thin Solid Films **517**, 2344-2348 (2009).

[45] J. Kierzenka, L.F. Shampine, "A BVP solver based on residual control and the MATLAB PSE ", ACM Transactions on Mathematical Software **27**, 299-316 (2001).

[46] S. Knabe, M. Langemeyer, F. Heidemann, G.H. Bauer, "Influence of the excess carrier lifetime depth profile on the emitted PL-spectrum of chalcopyrite thin films", Proceeding of 24rd European Photovoltaic Solar Energy Conference and Exhibition, Hamburg, Germany, WIP Renewable Energies, Munich, 2964-2966 (2008).

[47] S. Knabe, M. Langemeyer, F. Heidemann, R. Brüggemann, G.H. Bauer, "Study of the effect of excess carrier lifetime depth profiles and depth dependent absorption coefficients on the emitted photoluminescence spectrum of chalcopyrite thin films", Progress in Photovoltaics, accepted (12/2010).

[48] R. Mainz, F. Streicher, D. Abou-Ras, S. Sadewasser, R. Klenk, M.C. Lux-Steiner, "Combined analysis of spatially resolved electronic structure and composition on a cross-section of a thin film $Cu(In_{1-x}Ga_x)S_2$ solar cell", Phys. Status Solidi (a) **206**, 1017-1020 (2009).

[49] W.N. Shafarman, R. Klenk, B.E. McCandless, "Device and material characterization of Cu(InGa)Se2 solar cells with increasing band gap", J. Appl. Phys. **79**, 7324-7328 (1996).

[50] I. Repins, M.A. Contreras, B. Egaas, C. DeHart, J. Scharf, C. L. Perkins, B. To, R. Noufi, "19.9%-efficient ZnO/CdS/CuInGaSe2 solar cell with 81.2% fill factor", Prog. Photovolt. **16**, 235-239 (2008).

[51] R. Klenk, J. Klaer, R. Scheer, M.C. Lux-Steiner, I. Luck, N. Meyer, U. Rühle, "Solar cells based on CuInS2 - an overview", Thin Solid Films **480**, 509-514 (2005).

[52] J. Klaer, R. Klenk, H.W. Schock, "Progress in the development of CuInS2 based mini-modules", Thin Solid Films **515**, 5929-5933 (2007).

[53] E. Daub, P. Würfel, "Ultralow Values of the Absorption Coefficient of Si Obtained from Luminescence", Phys. Rev. Lett. **74**, 1020-1023 (1995).

[54] L. Gütay, G.H. Bauer, "Local fluctuations of absorber properties of Cu(In,Ga)Se-2 by sub-micron resolved PL towards "real life" conditions", Thin Solid Films **517**, 2222-2225 (2009).

[55] F. Heidemann, R. Brüggemann, G.H. Bauer, "The correlation between local defect absorbance and quasi-Fermi level splitting in CuInS2 from photoluminescence", Journal of Physics D **43**, 145103 (2010).

[56] G.H. Bauer, L. Gütay, "Analyses of local open circuit voltages in polycrystalline Cu(In,Ga)Se-2 thin film solar cell absorbers on the micrometer scale by confocal luminiscence", Chimia **61**, 801-805 (2007).

[57] P. Würfel, T. Trupke, T. Puzzer, E. Schaeffer, W. Warta, S.W. Glunz, "Diffusion lengths of silicon solar cells from luminescence images", Journal of Applied Physics **101**, 123110 (2007).

[58] P. Kittidachachan, "Reducing the cost of crystalline silicon solar cells by using fluorescent collectors", PhD thesis, Faculty of Engineering, Science and Mathematics, University of Southampton (2007).

[59] http://www.varianinc.com/, last time called: November 2010.

[60] http://www.witec.de/en/home/, last time called: November 2010.

[61] T.J.J. Meyer, "Photon Transport in Fluorescent Solar Collectors", PhD thesis at Faculty of Engineering, Science and Mathematics, University of Southampton (2009).

[62] J.D. Joannopoulos, R.D. Meade, J.N. Winn, "Photonic Crystals: Molding the Flow of Light", Princeton, Princeton University Press (1995).

[63] M. Skorobogatiy, J. Yang, "Fundamentals of Photonic Crystal Guiding", Cambridge, first edition, Cambridge University Press (2008).

[64] P.C. Mathias, H.Y. Wu, B.T. Cunningham, "Employing two distinct photonic crystal resonances to improve fluorescence enhancement", Appl. Phys. Lett. **95**, 021111 (2009).

[65] B. Curtin, R. Biswas, V. Dalal, "Photonic crystal based back reflectors for light management and enhanced absorption in amorphous silicon solar cells", Appl. Phys. Lett **95**, 231102 (2009).

[66] B.E.A. Saleh, M.C. Teich, "Fundamentals of photonics", New Jersey, second edition, John Wiley and Sons, New York (2007).

[67] P. Baumeister, "Simulation of a rugate filter via a stepped-index dielectric multilayer", Applied Optics **25**, 2644-2645 (1986).

[68] http://ab-initio.mit.edu/wiki/index.php/MIT_Photonic_Bands, last time called: November 2010.

[69] http://www.lumerical.com/fdtd.php, last time called: November 2010.

[70] P.M. Bell, J.B. Pendry, L. Matrin Moreno, A.J. Ward, "A program for calculating photonic band structures and transmission coefficients of complex structures", Computer Physics Communications **85**, 306-322 (1995).

[71] A.S. Dimitrov, K. Nagayama, "Continuous Convective Assembling of Fine Particles into Two-Dimensional Array on Solid Surfaces", Langmuir **12**, 1303-1311 (1996).

[72] Z.Z. Gu, A. Fujishima, O. Sato, "Fabrication of High-Quality Opal Films with Controllable Thickness", Chem. Mater. **14**, 760-765 (2002).

[73] Y.H. Ye, F. LeBlanc, A. Haché, V.V. Truong, "Self-assembling three-dimensional colloidal photonic crystal structure with high crystalline quality", Applied Physics Letters **78**, 52-54 (2001).

[74] S. H. Im, M.H. Kim, O.O. Park, "Thickness Control of Colloidal Crystals with a Substrate Dipped at a Tilted Angle into a Colloidal Suspension", Chem. Mater. **15**, 1797-1802 (2003).

[75] J.K. Kim, C. Mao, J. Kim, "Fabrication and properties of inverse opal photonic crystal films of La-doped bismuth titanate", Journal of Physics and Chemistry of Solids **69**, 1468-1470 (2008).

[76] J. Üpping, chapter "Optische und elektrische Eigenschaften von invertierten Opalen", PhD thesis, Martin-Luther-Universität Halle-Wittenberg, to be submitted 2011.

[77] M. Romanelli, C. Vion, C. Barthou, P. Benalloul, J.M. Frigerio, A. Maitre, P.T. Nga, P.T. Cuong, A. Gruzintsev, A. Redkin, "Angle-Resolved Reflectivity and Self-Activated Luminescence of 3D Photonic Crystals", Journal of Korean Physical Society **52**, 1589-1593 (2008).

[78] G.M. Gajiev, V.G. Golubev, D.A. Kurdyukov, A.V. Medvedev, A.B. Pevtsov, A.V. Sel'kin, V.V. Travnikov, "Bragg reflection spectroscopy of opal-like photonic crystals", Physical Review B **72**, 205115 (2005).

[79] S.A. Asher, J.M. Weissman, A. Tikhonov, R.D. Coalson, R. Kesavamoorthy, "Diffraction in crystalline colloidal-array photonic crystals", Physical Review E **69**, 066619 (2004).

[80] http://www.philiplaven.com/mieplot.htm, last time called: June 2010.

[81] http://www.mathworks.com/matlabcentral/fileexchange/19084-region-growing, last time called: November 2010.

[82] M.A. Green, "Silicon solar cells: advanced principles & practice", Sydney, Centre for Photovoltaic Devices and Systems, Univ. of New South Wales, (1995).

[83] http://www.photochemcad.com/, last time called: June 2010.

[84] M. Manssen, "Spektrale Transmission, Reflexion, Absorption und Fluoreszenz von Dielektrika", Bachelor Thesis, Carl von Ossietzky University Oldenburg (2009).

[85] J.R. Lakowicz, "Principles of Fluorescence Spectroscopy", second edition, Kluwer Academic/Plenum Publishers, New York (1999).

[86] D.K.G. de Boer, "Optimizing wavelength-selective filters for Luminescent Solar Concentrators", Proceedings of SPIE **7725**, 77250Q-1, SPIE Digital Library, USA (2010).

[87] T.J.J Meyer, J. Hlavaty, L. Smith, E.R. Freniere, T. Markvart, "Ray tracing techniques applied to modeling of fluorescent solar collectors", Proceedings of SPIE **7211**, 72110N, SPIE Digital Library, USA (2009).

[88] G. Smestad, H. Ries, R. Winston, E. Yablonovitch, "The thermodynamic limits of light concentrators", Solar Energy Materials **21**, 99-111 (1990).

[89] "2008 Solar Technologies Market Report: January 2010", NREL Report TP-6A2-46025, DOE/GO-102010-2867 (2010).

[90] http://trappist.elis.ugent.be/ELISgroups/solar/projects/scaps.html, last time called November 2010.

[91] A. Bielawny, J. Üpping, R.B. Wehrspohn, "Spectral properties of intermediate reflectors in micromorph tandem cells", Solar Energy Materials & Solar Cells **93**, 1909-1912 (2009).

[92] P. Sathy, R. Philip, V.P.N. Nampoori, C.P.G. Vallabhan, "Fluorescence quantum yield of Rhodamine 6G using pulsed photoacoustic technique", Pramana **34**, 585-590 (1990).

[93] http://www.lambdares.com/software_products/tracepro/, last time called: November 2010.

[94] J.A. Nelder, R. Mead, "A simplex method for function minimization", Computer Journal **7**, 308-313 (1965).

[95] http://www.shef.ac.uk/acse/research/ecrg/gat.html, last time called: November 2010.

[96] J.A. Giesecke, M. The, M. Kasemann, W. Warta, "Spatially resolved characterization of silicon as-cut wafers with photoluminescence imaging", Prog. Photovolt: Res. Appl. **17**, 217-225 (2009).

[97] J.A. Giesecke, M. Kasemann, W. Warta, "Determination of local minority carrier diffusion lengths in crystalline silicon from luminescence images", J. Appl. Phys **106**, 014907 (2009).

[98] P. Würfel, T. Trupke, T. Puzzer, E. Schäffer, W. Warta, S.W. Glunz, "Diffusion lengths of silicon solar cells from luminescence images", J. Appl. Phys **101**, 123110 (2007).

[99] http://pvcdrom.pveducation.org/APPEND/Silicon.htm, last time called: November 2010.

A. Symbols

Table A.1.: Symbols used in this work - I.

Symbol	physical property
$A(E_{Ph})$	spectral absorption
$\alpha(E_{Ph})$	absorption coefficient for the photon flux
$\tilde{\alpha}$	absorption coefficient for the amplitude
c	speed of light
γ	defect diffusion depth
$\Gamma(E_{Ph})$	spectral photon flux
$\Gamma_{norm}(E_{Ph})$	normalized emission
$\Gamma_{total}(\omega)$	spectral emission of the full absorber
$\Gamma(\omega, x)$	spectral emission from the absorber position x
δ	angle of detection
ΔE_G	variation in the band gap
d	absorber thickness
D	PMMA nanosphere diameter
D_c	diffusion coefficient of the excess carrier
e	elementary charge
E_{Ph}	photon energy
$\tilde{E}_{Ph}$	spectral emissivity
E_{F_n}	quasi Fermi level for electrons
E_{F_p}	quasi Fermi level for holes
E_g	band gap
g	generation rate
G_0	photon flux for excitation
h	Planck's constant
ϑ_{total}	angle of total reflection
I	intensity or photon flux
j	current density

Table A.2.: Symbols used in this work - II.

Symbol	physical property
$\vec{k}$	wave vector
k_B	Boltzmann's constant
L	diffusion length
μ	splitting of quasi-Fermi levels
n	excess carrier concentration
n_0	thermal equilibrium electron concentration
n_i	refractive index of medium i
P	amplitude of the source S
p_0	thermal equilibrium hole concentration
r	recombination rate
R	reflection coefficient for the intensity
S_0, S_d	surface recombination velocity at $x = 0$, $x = d$
r_{ij}	reflection coefficient for the amplitude between medium i and j
T	sample temperature
t_{ij}	transmission coefficient for the amplitude between medium i and j
T_{ij}	transmission coefficient from layer i to j for the intensity
τ_0	excess carrier lifetime
$\tau(x)$	excess carrier lifetime depth profile
τ_f	reduction of the excess carrier lifetime at $x = d$
v	effective drift speed of electrons
V_{OC}	open circuit voltage
Ω	solid angle

B. Calibration of the experimental setups

There are different calibrations needed, depending on how the experimental results are further processed:
The spectral calibration of the spectrometer is always needed. In this case, the first and second order of the Ar^+-ion excitation laser (488 nm and 976 nm) were used to calibrate the spectrometer. This gives a wavelength calibration needed for the measurements of the flucos (between 500 nm and 800 nm) as well as for c-Si (around 1100 nm). When the wavelength of the measured radiation is much larger than the upper calibration wavelength, the wavelength error is increased. Additionally the wavelength dependent sensitivity of the detector should be corrected in a relative calibration if the experimental results are compared with other experiments or with the literature. This includes a calculation of the wavelength dependence of all filters in the experimental setup to get the "real" radiation. This is done e. g. with a calibration lamp with known emission.
Depending on the calibration lamp and on the setup there is either a relative or an absolute calibration possible. Absolute means that the photon flux for all wavelengths is known whereas only the differences in the photon flux between the wavelengths are known with a relative calibration. The experimental results in this work are either only spectrally calibrated (when a comparison between the results is sufficient) or absolutely calibrated.

C. Estimation of the excess carrier concentration from the PL yield

C.1. Idea

The simulation described in the theory (chapter 2.2 and 2.3) for the PL emission from the top of the absorber for a specified excess carrier concentration provides excess to parameters of the excess carrier concentration from PL measurements. This possibility will be introduced in the following. This topic is not really related to the rest of the thesis, so unfortunately, only a short introduction to the idea of the estimation of excess carrier density depth profile parameters from PL yields will be given.
Other possibilities to calculate the excess carrier concentration from the PL yield are discussed in [96–98], which use an other principle.

Fig. C.1 and C.2 show the principal idea, how the excess carrier concentration can be reconstructed for a measured PL yield. As always in the PL simulations in this thesis, the detector is assumed to be on the right side of the absorber, so if the absorber is excited from the side of the detector, this is named excitation from the right or in reflection[1] and if the absorber is excited from the other side, this is named excitation from the left or in transmission[2].
These different excitation positions lead to nearly the same excess carrier concentration for the same surface recombination velocity on both absorber surfaces ($S_0 = S_d$), which are point wise symmetric regarding the center position of the absorber. The higher concentration is on the side of the excitation and the lower one on the other side, so that the excess carrier concentration at the surface on the side of the detector is different but the overall carrier concentration is the same (Fig. C.2 (left)). This results in the same PL yield for small photon energies and different photon fluxes for higher photon energies (Fig. C.2 (right)) as observed before (chapter 2.3.1.1). This different PL yields for the high photon energy wing of the PL in comparison to the same PL yield for the low photon energies provide access to the parameters of the excess carrier concentration with the algorithm which is illustrated in Fig. C.3:
For a given model for the excess carrier concentration (e. g. the one discussed in chapter 2.3.1 with S_0, S_d, D_c and τ) a set of parameters is guessed, the according excess carrier concentration is calculated and therefrom the emitted PL yield for both excitation positions is simulated. These results are compared to the given PL yields and the differences are calculated using the

[1] Excitation and detection on the same surface of the sample.
[2] Excitation and detection on different surfaces of the sample.

following deviations (named cost functions)

$$dev_1 = \frac{1}{E_1 - E_0} \int_{E_0}^{E_1} |\Gamma_{sim_l}(E) - \Gamma_{mess_l}(E)|\, dE \tag{C.1}$$

$$dev_2 = \frac{1}{E_1 - E_0} \int_{E_0}^{E_1} |\Gamma_{sim_r}(E) - \Gamma_{mess_r}(E)|\, dE \tag{C.2}$$

with the PL yield from the simulation for the excitation from left ($\Gamma_{sim_l E}$) and right ($\Gamma_{sim_l E}$) as well as the PL yield of the given PLs (e. g. from the experiment) for the excitation from the left ($\Gamma_{mess_l}(E)$) and right ($\Gamma_{mess_r}(E)$). All PL yields are given between the photon energies E_0 and E_1. The overall difference between the simulated and measured spectra is given by the addition of dev_1 and dev_2.
Depending on these deviations between the simulation and the given PL yields, the algorithm either stops the simulation or calculates a new set of parameters and starts with the calculation of the excess carrier concentration again.
The calculation of the new set of parameters for the excess carrier concentration depending on the sum of dev_1 and dev_2 is either done with a Nelder Mead algorithm (NMA) (see e. g. [94]) or a genetic algorithm (GA) for MatLab [95]. The differences between these two algorithms will not be discussed. The advantage of the GA is a much shorter calculation time than for the NMA, because it finishes for this kind of problem in less then a tenth of the time needed by the NMA.
In the following sections the uniqueness of the different parameters on both parameters dev_1 and dev_2 from eqs. (C.1) and (C.2) will be characterized. Afterwords results of the reconstruction of a simulated excess carrier concentration from the calculated PL yields will be presented to show the quality of the results from the algorithms and finally the estimation of the excess carrier concentration for a c-Si wafer and the according results will be discussed in detail.

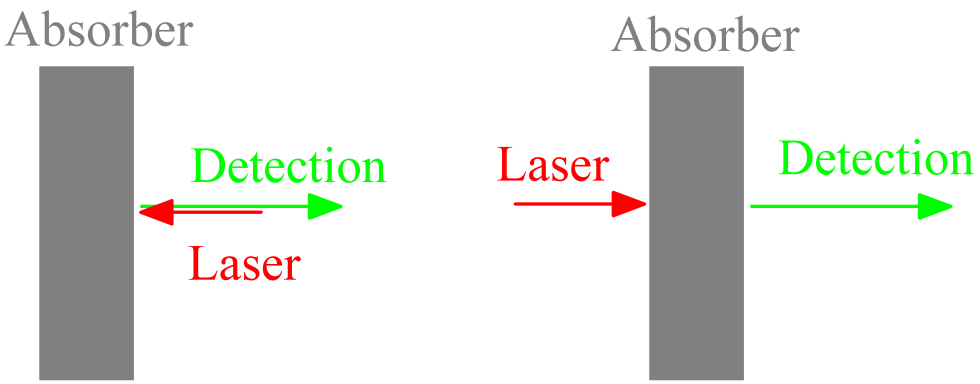

Figure C.1.: Idea for the calculation of the excess carrier concentration from the PL yield: Comparison of the emitted PL for the excitation from side of the detector (left) named excitation from right or in reflection and for the excitation from the other side of the absorber (right) named excitation from left or in transmission.

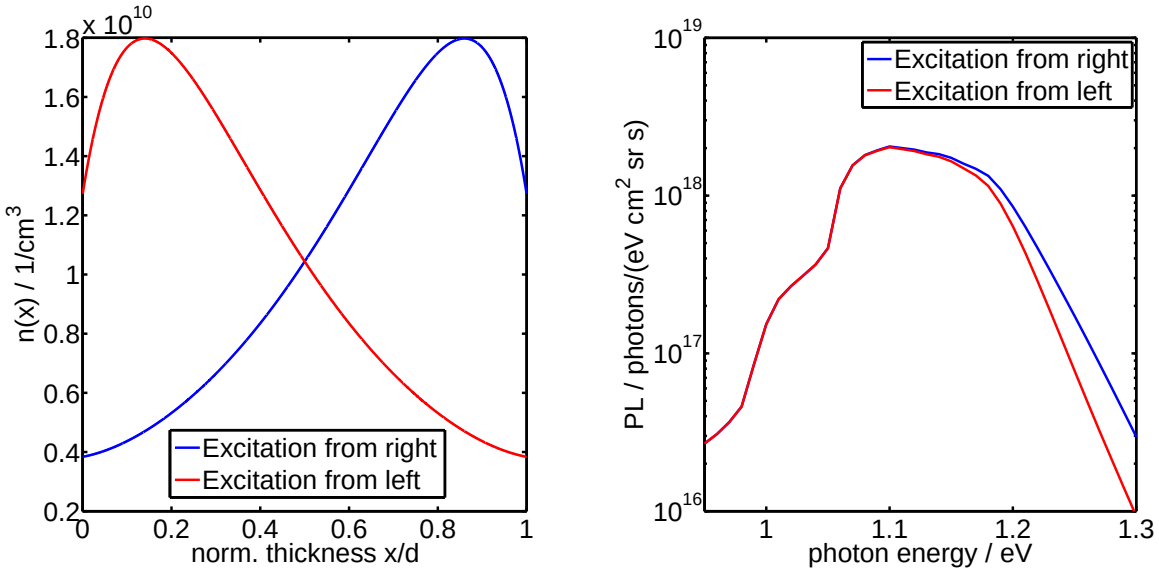

Figure C.2.: Excess carrier concentration for the excitation of an absorber from the left side and the right side (left) as well as the emitted PL yield for the PL emission on the side of the detector (right).

C.2. Uniqueness of the different parameters

In this case the word uniqueness means: Is the result of the minimization of dev_1 and dev_2 unique or are there different results of a parameter of the excess carrier concentration, which have the same or nearly the same global minima of dev_1 and dev_2?

To analyze if the parameters are unique, an excess carrier concentration with the parameters in Tab. C.1 and the resulting PL yields for an excited 250 µm thick c-Si wafer with dev_1 and dev_2 for different values of a single parameter S_0, S_d, τ and D are calculated to see how many times dev_1 and dev_2 are zero for each parameter. Hence one can see if the estimation of only one parameter has a unique result.

Exemplary results of this process for S_0 and D with the rest of the excess carrier parameters fixed are plotted in Fig. C.4. One can clearly see that the parameter S_0 is unique, because $dev_1 = 0$ and $dev_2 = 0$ is true only for the one value of S_0 which is the one in Tab. C.1. The variation of D shows two different values of D for which $dev_2 = 0$ is true and only on where $dev_1 = 0$ is true, so that the sum of both parameters dev_1 and dev_2 also leads to only one value of D, so that D is also unique. The same can be derived for the other two parameters of the excess carrier concentration.

There are some more informations, which can be deducted from this calculations. These are summarized in Tab. C.2: for all 4 parameters mentioned above and the excitation photon energy E_{in} the sign of dev_1 and dev_2 for a to high or to low value of each parameter is given, the deviation dev_1 and dev_2, which is higher is given and some more informations. E. g. the deviations dev_1 and dev_2 are higher if E_{in} is to high than as if E_{in} is to low.

These informations can be used to reconstruct one or even two values with a gradient descent,

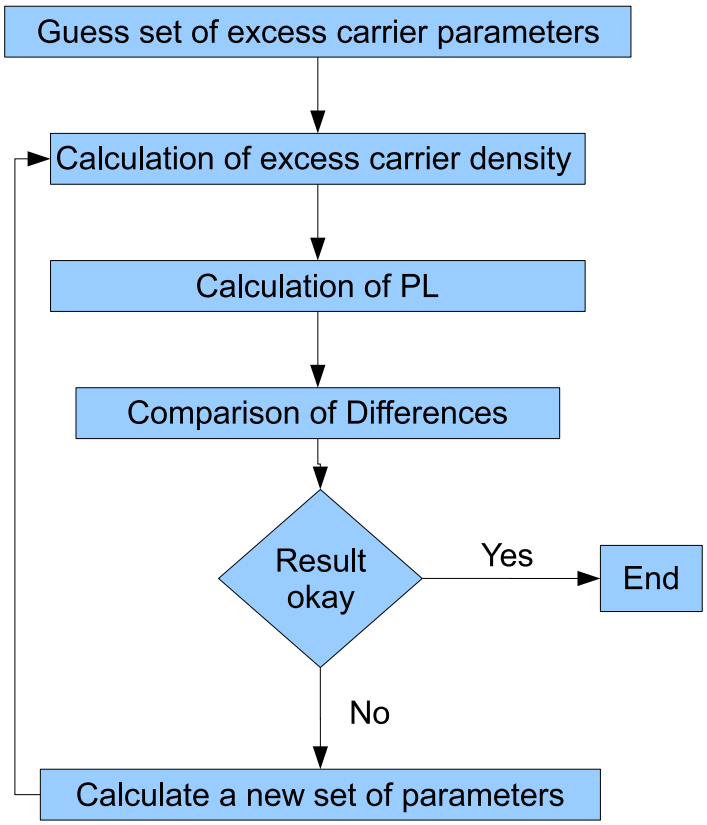

Figure C.3.: Idea for the algorithm, which calculates the excess carrier concentration from the PL: An excess carrier profile with a set of random parameters is calculated, the resulting PL yield is calculated and compared to the given PL yield and afterwords the set of parameters is varied till the calculated PL yield equals the given PL yield.

which is based on the comparison of dev_1 and dev_2, but unfortunately it is not possible to reconstruct more than two parameters at once with a gradient descent so to more "powerful" algorithms mentioned above (NMA and GA) are needed.

Table C.1.: Parameters of the excess carrier concentration used in the simulations.

Parameter	Value
S_0	1000 cm/s
S_d	1000 cm/s
τ	3.42 µs
D	3.388 cm^2/s

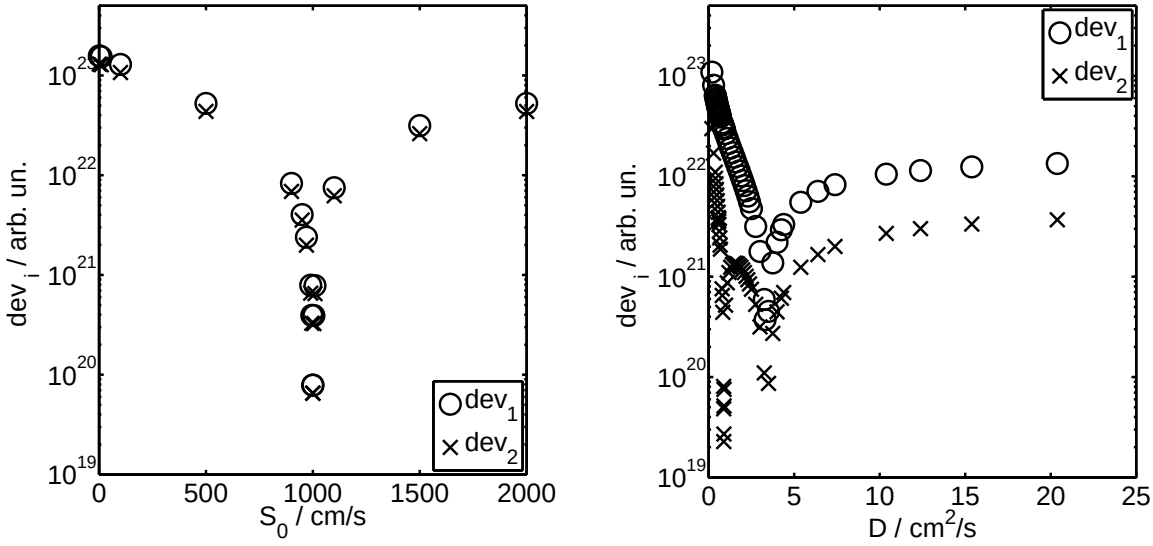

Figure C.4.: Deviations $dev_{1,2}$ for the variation of S_0 (left) and D (right) while the other parameters are fixed.

C.3. Application to simulated spectra

The first step is to reconstruct the parameters of the excess carrier concentration $n(x)$ from a simulated PL spectra. Fig. C.5 (left) shows the excess carrier concentration for an absorber of d=20 µm thickness, surface recombination velocity $S_0 = S_d = 1000$ cm/s, carrier lifetime $\tau = 3.42$ µs and diffusion coefficient $D_c = 3.388$ cm^2/s for the excitation from the right side as well as the resulting PL yield in Fig. C.5 (right) for a Nelder-Mead algorithm (NMA).
Both excess carrier concentrations and PL spectra are nearly identical beside some minor differences especial in the excess carrier concentration. But the results are rather promising, because the overall shape of the excess carrier concentration reconstructed from the PL yield agrees quite well with the excess carrier concentration used for the calculation of the PL yield.

Table C.2.: Overview over the influence of a too low or high parameter of the excess carrier concentration on $dev_{1,2}$ with sign (s($dev_{1,2}$)), which deviation is higher ($b(dev_i)$) and some additional informations. Here E_{in} donates the photon energy of the excitation.

	s(dev_1)	s(dev_2)	$b(dev_i)$	additional information
S_0 too low	-	-	1	dev_1 is always a little
S_0 too high	+	+	1	higher than dev_2
S_d too low	-	-	2	dev_2 is always a little
S_d too high	+	+	2	higher than dev_1
E_{in} too low	-	-	-	If E_{ein} is too high
E_{in} too high	+	+	1	$dev_{1,2}$ are lower
τ too low	+	+	1	If τ is too high
τ too high	-	-	-	$dev_{1,2}$ are lower
D too low	-	+/-	1	If D is too low
D too high	+	-	1	dev_2 has a second minimum

A comparison of the parameters of the excess carrier concentration used for the calculation of the PL yields and the parameters of the reconstructed excess carrier concentration is shown in Tab. C.3. These results are completed with the results of the reconstruction of the excess carrier concentrations with the genetic algorithm (GA). Both algorithms give quite good results for the surface recombination velocities S_0 and S_d and the excess carrier diffusion coefficient D, but the results for the reconstruction of the excess carrier lifetime are different from the initial value. The results of the different algorithms seem to agree roughly.
So it seems that this reconstruction of the excess carrier concentration parameters is sensitive for the surface recombination velocities and the diffusion coefficient but not sensitive for the reconstruction of the excess carrier lifetime with a low error.

Table C.3.: Parameter of the excess carrier concentration: Simulated, reconstructed Nelder Mead and reconstructed generic algorithm.

Parameter	Simulation	Reconstruction NMA	Reconstruction GA
S_0 / cm/s	1000	1045	906
S_d / cm/s	1000	1669	971
τ / µs	3.42	56	41.6
$D/\mathrm{cm}^2/\mathrm{s}$	3.388	4.6	3.60

C.4. Application to measured spectra

In this section results of the estimation of the excess carrier concentration from the PL yields from an excited c-Si wafer of 250 µm thickness with SiC_x passivation on both surfaces will be

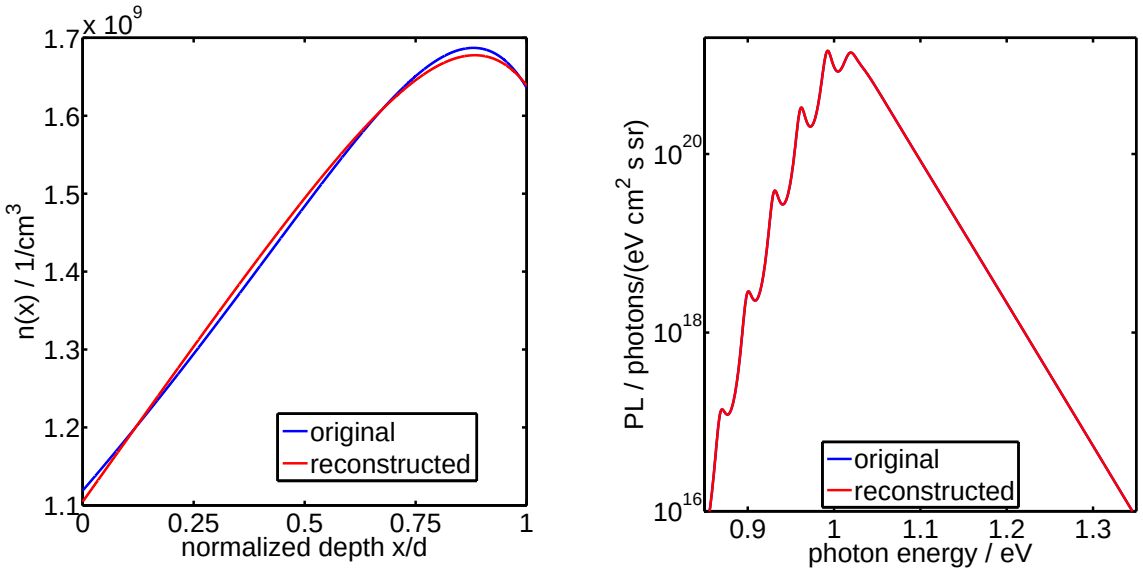

Figure C.5.: Simulated as well as reconstructed excess carrier concentration (left) and simulated as well as reconstructed PL yield (right).

explained. The PL yield is measured with a calibrated PL setup with an excitation with a 488 nm Ar-Ion laser with a photon flux of $1.5 \cdot 10^{18}$ photons/cm^{2}s on a spot of ca. 2.1 mm diameter. The PL is measured in reflection setup.

The differences between the PL yield in reflection and transmission are measured in the angular dependent PL setup from chapter 3.1 with the same excitation so that the absolute PL yield in reflection and transmission is available. The results of the calculation of the absolute PL yields of the measurements are in Fig. C.6 (left). There nearly no differences between the PL yield in reflection and transmission observable, so the excess carrier concentration should be nearly flat. Results of the excess carrier concentration (excitation from the left) are plotted in Fig. C.6 (right) and the parameters of the excess carrier concentration estimated from the PL yield can be found in Tab. C.4 for the NMA. The shape of the excess carrier concentration agrees well with the expectation of a rather flat profile and the surface recombination velocities are also low, which agrees quite well with the values ($S_i \leq 20$ cm/s) provided by ISE where the samples were made. The higher value of $S_0 = 57$ cm/s is also reasonable, because the surface passivation can be damaged by different reasons (e. g. by scratches on the wafer) and the sample is rather old and was used often.

The diffusion coefficient and excess carrier lifetime result in a carrier diffusion length of

$$L = \sqrt{\tau \cdot D} \approx 900 \text{ µm}, \tag{C.3}$$

which is quite high and the diffusion coefficient should be around 30 cm^2/s [99] depending on the doping concentrations, so that the results for τ and D are not even in the same order of magnitude as the expected parameters.

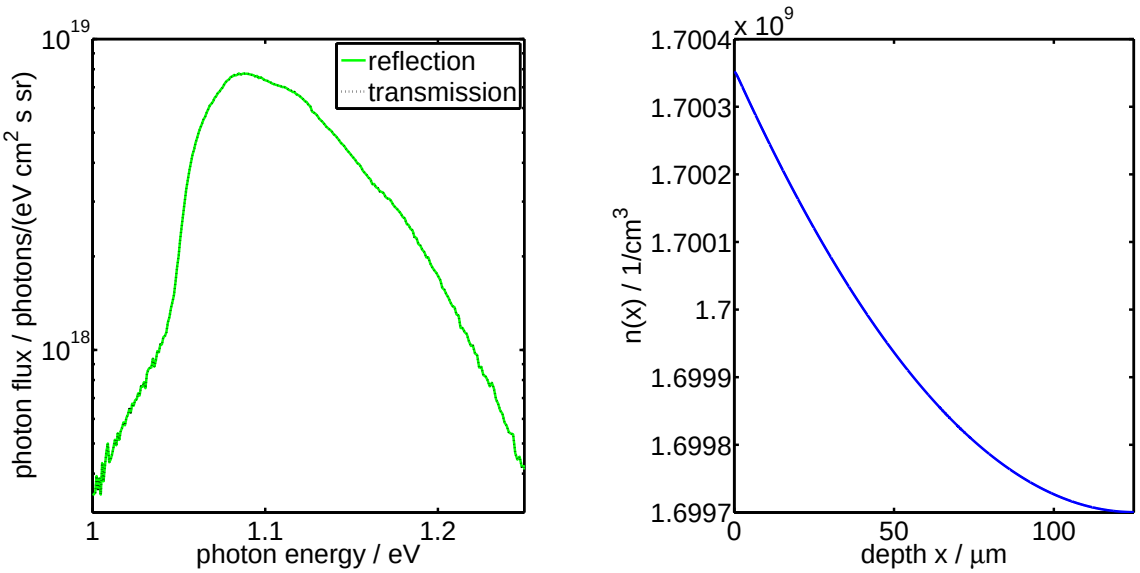

Figure C.6.: Experimental results of the emitted PL from an excited c-Si for the excitation and detection from one side and from different sides (left) and result of the estimation of the excess carrier concentration (right) with the Nelder Mead Algorithm.

Table C.4.: Results of the excess carrier concentration in excited c-Si from Nelder Mead algorithm and generic algorithm.

Parameter	result with NMA
S_0 / cm/s	57
S_d / cm/s	4.8
τ/µs	0.37
D/cm^2/s	$2.2 \cdot 10^6$

C.4.1. Different cost functions

One possible improvement is the application of an other function for the calculation of the differences between the measured and simulated spectra beside eqs. (C.1) and (C.2). One possibility is using the square of the absolute values

$$dev_1 = \frac{1}{E_1 - E_0} \int_{E_0}^{E_1} \left|\Gamma_{sim_l}(E) - \Gamma_{mess_l}(E)\right|^2 dE \tag{C.4}$$

to give a simulation result, which is farther away than an other one, a higher error or using

$$dev_1 = \frac{1}{E_1 - E_0} \int_{E_0}^{E_1} \left|\log(\Gamma_{sim_l}(E)) - \log\Gamma_{mess_l}(E)\right|^2 dE \tag{C.5}$$

to take into account that the differences for higher photon energies are especially important but the photon flux is much lower than the one at the maximum PL yield. A third possibility is to use the ratio between the simulation and the real spectra

$$dev_1 = \frac{1}{E_1 - E_0} \int_{E_0}^{E_1} \Gamma_{sim_l}(E)/\Gamma_{mess_l}(E) dE \tag{C.6}$$

which would have the advantage, that no calibration of the setup is needed. The first will be named linear, the second logarithmic and the third division. An other possibility is to change the idea and to use only one spectrum, so that not a spectrum in reflection and transmission is needed.

This time the experimental data used for the simulation are the results of PL measurements in reflection and transmission in the calibrated PL setup with an excitation photon flux of about $1.4 \cdot 10^{18}$ photons/cm^{2}s over the same number of mirrors on both surfaces of the sample for an other position of the c-Si wafer with SiC_x passiavation on both surfaces. The detection is always performed on the same surface of the sample. The results of the measurements are plotted in Fig. C.7. The excitation is so high (higher than AM1 equivalence) to enhance the signal-to-noise-ratio.

The results are for a different sample position, because it is not possible to mark the position of the measurement for a later repeat under other experimental conditions. Tab. C.5 shows the results of the excess carrier concentration estimated with the different cost functions discussed above with consideration of two spectra and only one spectrum (reflection) for calculation with the GA. The NMA yields similar results but needs a much longer calculation time.

These results are a little bit confusing, because different cost functions can yield at least sometimes different results for the parameters of the excess carrier concentration. E. g. the logarithmic and linear cost functions yield nearly the same values for S_0 but different values for S_d. But one result is, that the logarithmic cost function with consideration of both spectra yields the results, which are more plausible than the other results and the value of the carrier diffusion length L is in most cases plausible, because good c-Si shows a diffusion length of about 300 µm (from [98]).

C.4.2. Possible problems of the estimation of n from the PL yield

There many possible sources for the high errors of results persent, which are mainly connected to the quality of the PL spectra used for the estimation of the excess carrier concentration pa-

Table C.5.: Results of the excess carrier concentration in excited c-Si from the Generic algorithm for different cost functions.

Parameter	logarithmic	linear	division	1 spectrum log	1 spectrum lin
S_0 / cm/s	294 ± 34	311 ± 4	22 ± 15	613 ± 44	403 ± 36
S_d / cm/s	37 ± 35	728 ± 23	54 ± 24	550 ± 32	658 ± 33
τ /µs	25 ± 14	87 ± 36	850 ± 50	300 ± 210	153 ± 23
L / µm	275 ± 70	513 ± 96	1600 ± 46	298 ± 138	682 ± 54

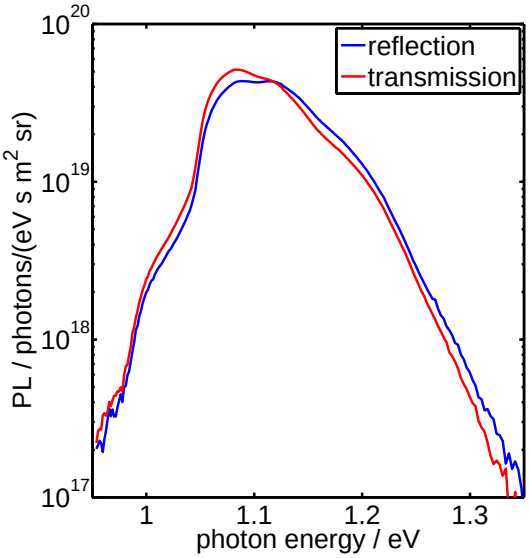

Figure C.7.: PL spectra for the emission of excited c-Si for measurements in reflection and transmission each.

rameters:
The influence of the shape of the excess carrier concentration can only be observed in the photon flux for high photon energies as illustrated in Fig. C.2 (right). But the PL yield for these photon energies is rather low, so that the signal-to-noise ratio is low, which leads to a complicated calculation of the differences between the measurements of the PL in transmission and reflection. Thus a detector system with a rather low noise level and a high excitation photon flux is needed to enhance the results.
The second problem is, that the measurement of the PL in transmission and reflection must be performed at the same position of the sample. This is also rather complicated, because e. g. a marking of the positions for the measurements can influence the surface passivation of the sample.
An other problem is the excitation under exactly the same conditions: To get the results of the PL in transmission and reflection under the same conditions, the excitation must be done under the same angle of incidence and the same photon flux. Therefor either a guiding of the laser radiation to both surfaces of the sample is needed[3] or the detector system must be moved, so that a detection from both surfaces is possible.
For the first possibility either a glass fiber to guide the radiation or mirrors are used. The first approach results in different excitation conditions because a movement of the fiber varies the guided photon flux due to changes in the polarization or a set of mirrors to guide the radiation. For the second approach is the same number of mirrors for both path ways of the excitation needed and the same angle of incidence on these mirrors, which is rather complicated to realize, because otherwise the radiation reflected by a mirror is different and thus the excitation on the sample in both cases is different.
The second possibility was tried as well. But here is the problem: Either the full detector system has to be moved, which is rather complicated or the radiation must be coupled into a glass fiber as in the setup in chapter 3.1. This setup also has the disadvantage of a movable glass fiber, but the PL radiation is not as coherent as the excitation radiation of the laser, so that the variation of the guided radiation is much lower than for the guiding of the excitation laser, because the effect of speckle due to interferences is much lower.
Additionally there is the possibility that the GA or NMA stops in a local minimum and does not find the global minimum.

Some words on the problem of the measurement of the PL yield for higher photon energies:
The differences between the PL yield in transmission and reflection is rather low due to the good passivation of the sample used in this chapter, thus the differences between both PL yields can be in the same order as the noise of the detector system. Fig. C.8 shows the PL yield in transmission and reflection of the same sample as before for an excitation of ca. $6.7 \cdot 10^{19}$ photons/(cm^{2}s). The PL spectrum is the average spectrum of three measurements and the error bars are the difference of the average spectrum to the maximum/minimum values. All measurements where performed under the same conditions without changing the sample position.

[3] and therefor a flipping of the sample to get the results for the setups illustrated in Fig. C.1.

One can observe that the differences between the PL spectra for high photon energies are low and for some photon energies lower than the error bars. The differences of the overall photon flux result from different excitation angles between transmission and reflection measurements due to the different laser beam paths used in reflection and transmission measurements, because the excitation is different and the detector is on the same side of the sample.

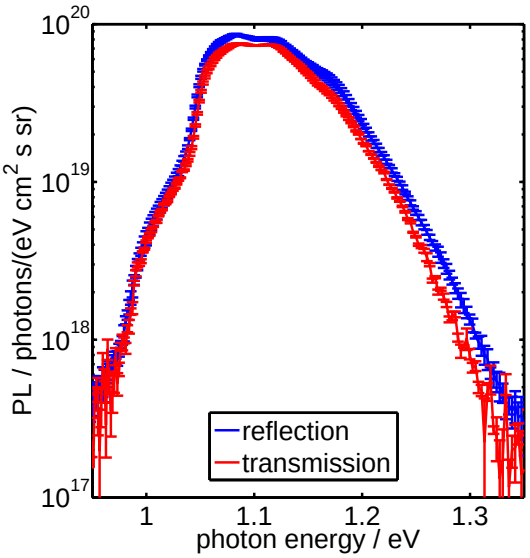

Figure C.8.: Results of PL measurements in transmission and reflection. The error bars result from the averaging of the measurements on the same spot of the sample and the same excitation.

C.5. Summary and conclusion

A new possibility to calculate the parameters of the excess carrier concentration from different PL yields was introduced (in transmission and reflection) and first results for the application on simulated and measured PL spectra for crystalline silicon were given. Different functions to calculate the differences between the initial and reconstructed spectra were used and different algorithms to optimize the set of excess carrier concentration parameters were tried.
The results show that an estimation of the parameters of the excess carrier concentration with this calculation is possible and that the results agree quite well with the parameters observed for crystalline silicon but the errors of the results are still too high. An variation of the cost function and the optimization algorithm as well as a better experimental setup which is optimized to measure the PL in reflection and transmission should be able to enhance the quality of the results.
Unfortunately this algorithm is not the aim of this thesis so no other semiconductor samples were used and the results were not compared with the other methods discussed in the literature and mentioned above. But this approach has the advantage of being able to handle other materials as crystalline silicon as well, because the PL simulation from the theory is able to calculate the

emitted PL for many different absorbers due to the consideration of so many different absorber parameters.

D. A detailed presentation of the edge emission of a fluco

In this section some results of the edge emission from a fluco with Lumogen F rot 305 in PMMA with a size of ca. $25 \cdot 25$ mm^2 and a thickness of 1 mm will be introduced which can be extracted from the results in Fig. 4.28 for the fluco with 0.3 g/l and 0.8 g/l dye concentration.
Fig. D.1 shows the normalized spectral dependent edge emission from both flucos (0.3 g/l left and 0.8 g/l right) for different excitation positions on top of the fluco with a specified distance between the edge of the fluco for an emission angle of 40°. One can observe that the normalized photon flux for small wavelengths is reduced with increasing distance between excitation and emission edge due to reabsorption. The normalized photon flux for larger wavelengths is nearly the same for all excitation positions on top of the fluco.
An other possibility to plot the results can be seen in Fig. D.2. Here the normalized edge emission is plotted for different emission angles for 3 excitation positions (left: Excitation near the emission edge, center: Excitation in the center of the sample and right: Excitation near the far edge) for the fluco with the higher dye concentration. Here one can observe that the emission for different emission angles on one excitation position shows only a small spectral influence and that the spectral differences between different angles are reduced if the excitation is farther away from the emission edge.
The calculation of the wavelengths for which the emission reaches 50% of the maximal emission for the results in Fig. D.1 are plotted in Fig. D.3. Here one can observe that the rabsorption is stronger for an excitation farther away from the emission.
These results could be used to calculated the reabsorption, because from the emission angle and the distance of excitation and the emission edge one can calculate the propagation length of the emitted radiation inside the fluco. Also an estimation of the bulk and surface scattering should be possible, because:
The radiation emitted under different emission angles for one excitation positions has different propagation lengths inside the fluco and different numbers of reflection on the surfaces of the fluco. Thus it should be possible to at least compare the influence of the surface and bulk scattering.
But unfortunately a detailed discussion of these calculations was not possible in the work for this thesis.

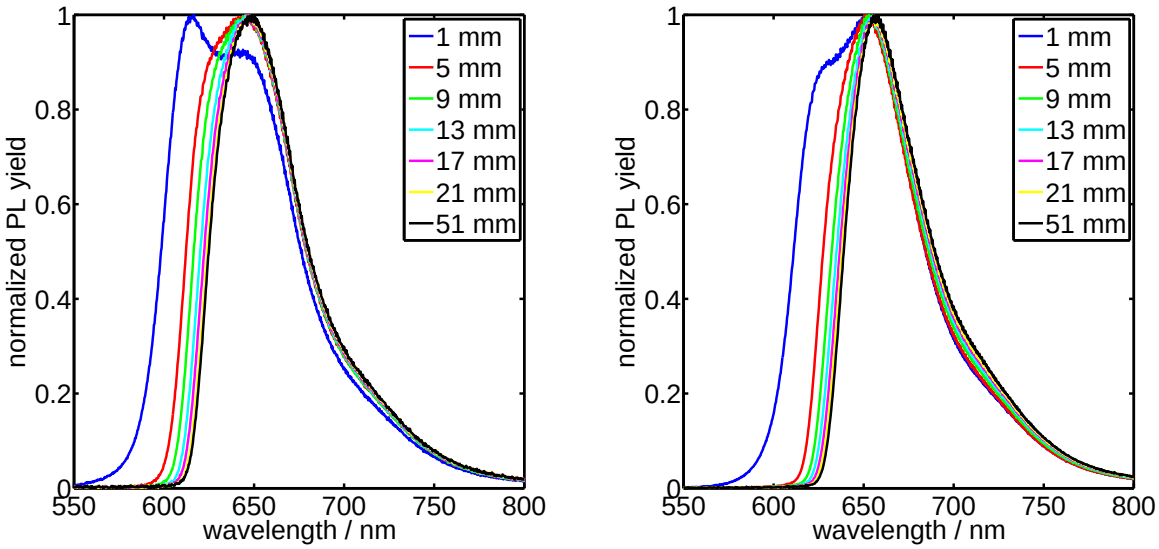

Figure D.1.: Spectral edge emission for an emission angle of 40° for different distances between excitation and emission edge for the fluco with 0.3 g/l (left) and 0.8 g/l (right) Lumogen F rot 305.

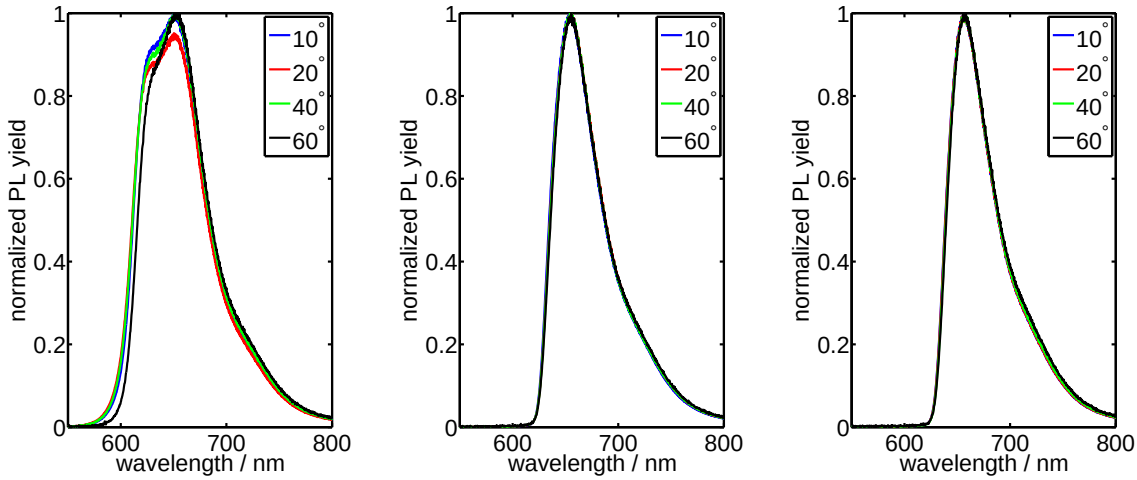

Figure D.2.: Spectral emission at the edge for different emission angles for excitation ca. 1 mm from the emission edge (left), in the center of the fluco (center) and ca. 24 mm from the emission edge (right).

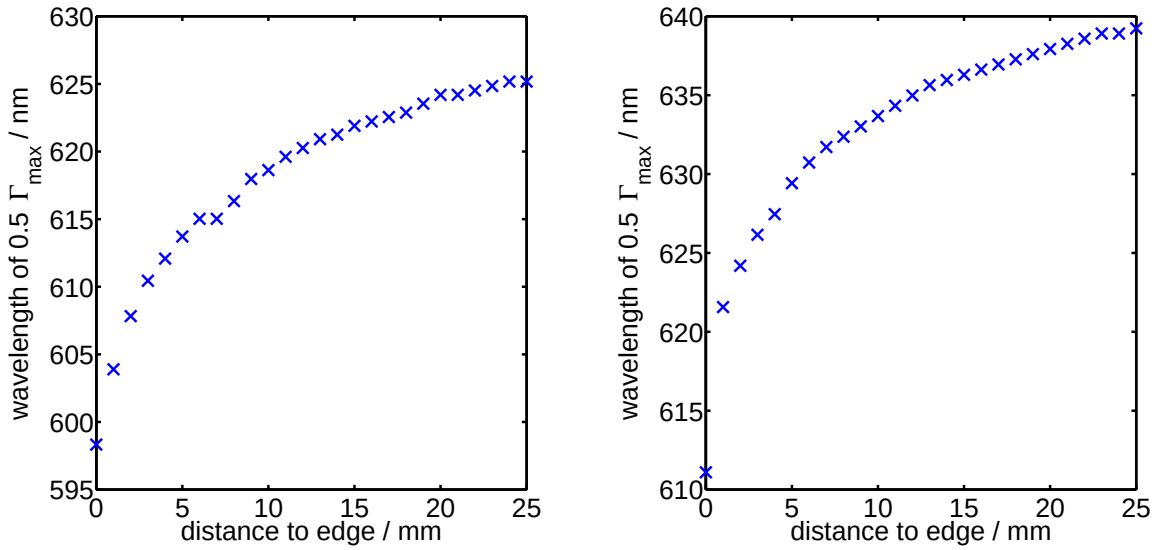

Figure D.3.: Wavelength at which the PL yield reaches 50% of the maximum PL yield ($0.5\Gamma_{max}$) vs. the distance between between excitation and emission edge for the fluco with 0.3 g/l (left) and 0.8 g/l (right) Lumogen F rot 305.

E. Filter and fluco edge emission - angular dependences

In the following section some results of the angular dependent and spectrally resolved edge emission of an excited fluco with 0.8 g/l Lumogen F rot 305 in PMMA for a homogeneous excitation with a 488 nm on the top and with different configurations will be discussed. The setup is the same as in chapter 4.4.2.2 for the fluco with Rhodamin 6 G and the angular dependent and spectrally resolved edge emission. But a detailed discussion of the results will not be given, because they are a little confusing and a detailed discussion is not contents of this thesis.
Fig. E.1 shows the ratio of the edge emission of the fluco with back reflector (cellulose based) and without back reflector. The emission for nearly all wavelengths and angles is enhanced between 0% and nearly 50%, which results from a backscattering of the radiation inside the escape cone into the fluco. This radiation would normaly be lost from the fluco. The enhancement is reduced for low emission angles, because here only the direct emission from the dye can reach the detector.
It would be interesting to use different back reflectors and measure the edge emission to analyse, what type of back reflector (mirror, scatterer, etc.) enhances the edge emission stronger and what for an influence on the angular emission they have.

Fig. E.2 shows the ratio of the angular dependent and spectrally resolved fluco edge emission with teflon spacer on top of the fluco and without teflon spacer (left without back reflector, right with back reflector). The spacer is a frame with a thickness of ca. 1 mm and the size of the fluco. Due to the spacer the edge emission is reduced for small emission wavelengths due to the influence on the excitation. The spacer covers the top of the fluco, thus the fluco is not excited near the emission edge and thus the emission with low wavelength is reduced as discussed in chapter D. It is preferable to use only very small spacers at each corner of the fluco and not along each edge. The back reflector only enhances the reduction of the edge emission for small wavelengths.

In Fig. E.2 is the ratio of the edge emission for the filter on top of the fluco (left) and for the filter on spacer on top of the fluco (right) through the emission without filter with a back reflector plotted. In comparison to the result for the ratio of the emission of the fluco with filter on top through the emission without filter without back reflector in Fig. F.6 one can observe a higher emission for higher emission angles which can result from the backscattering of radiation. If the filter is positioned on top of spacers on top of the fluco, the enhancement of the edge

emission for low emission angles can not be observed anymore.
So it is not clear, which element has exactly which influence on the angular dependent and spectrally resolved fluco edge emission and additional experiments and simulations have do be performed to understand the effects in more detail, but this work was not possible for this thesis.

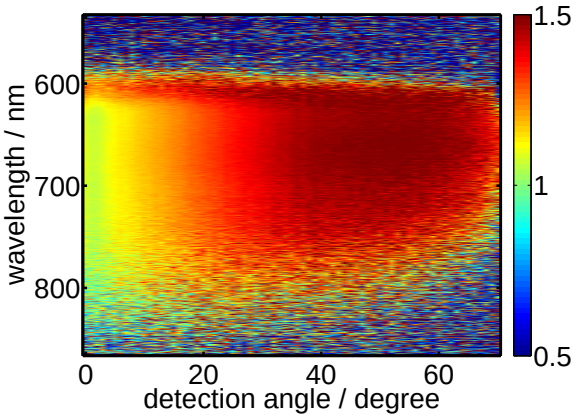

Figure E.1.: Ratio of the angular and spectrally resolved edge emission with back reflector and without back reflector for a fluco with 0.8 g/l Lumogen F rot.

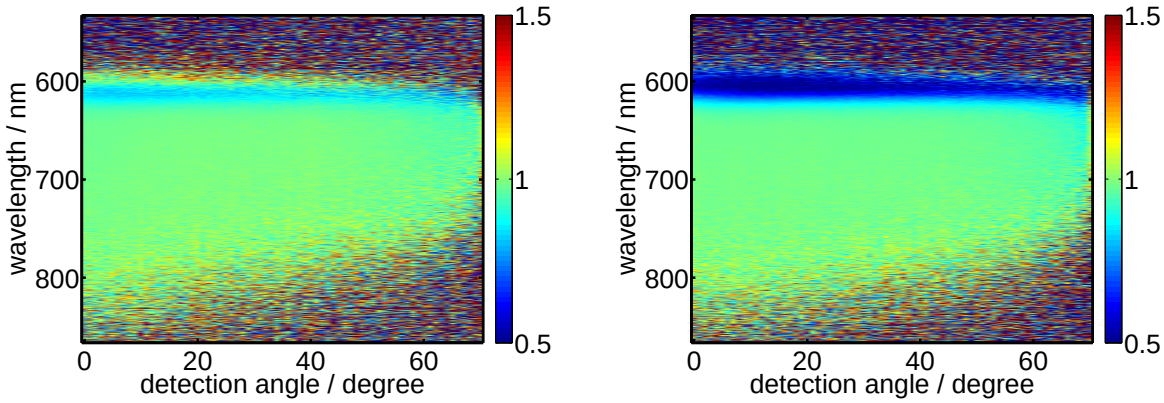

Figure E.2.: Ratio of the angular and spectrally resolved edge emission with spacer between fluco and filter and without them with back reflector (left) and without (right) for a fluco with 0.8 g/l Lumogen F rot.

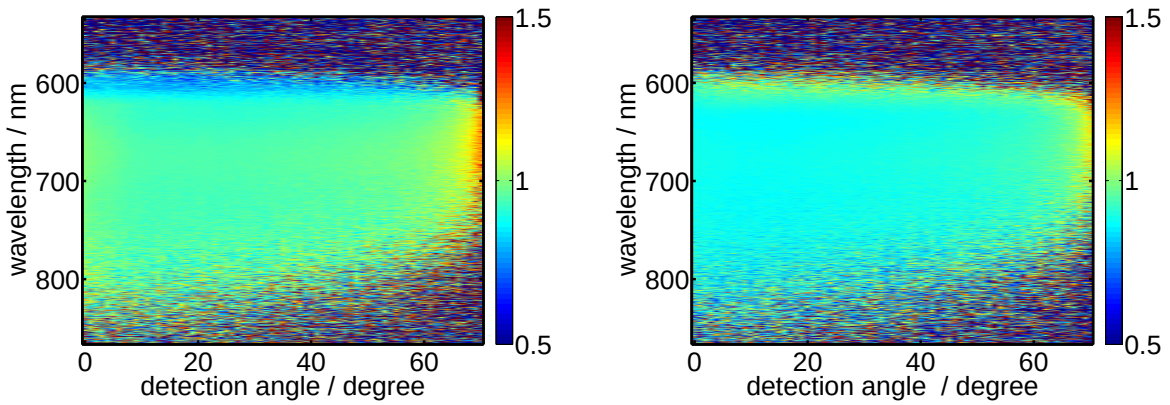

Figure E.3.: Ratio of the angular and spectrally resolved edge emission with filter and without filter with back reflector and the filter on top of the fluco (left) and with the filter on spacer on top of the fluco (right) for a fluco with 0.8 g/l Lumogen F rot.

F. Effect of a photonic structure on the edge emission of a fluco

In this chapter only the results for the influence of the Bragg-mirror with 550 nm edge in the transmission through the filter will be presented, because the opal is not as large as the fluco, so a study of the influence on edge emission with the opal on top of the fluco is not useful.
The influence of a photonic structure on top of the fluco on the edge emission is studied with the experimental setups in chapters 3.3 (fluco edge emission) and 3.1 (angular dependent PL). The first setup provides access to the absolute emitted photon flux on one edge of the fluco whereas the second one gives the angular and spectrally resolved edge emission.
The influence of a 550 nm low-pass filter on the absolute edge emission for different positions of the filter is illustrated in Fig. F.1. The filter is located either directly on top of the fluco (center) or on spacers on the fluco (right) for comparison with the edge emission without a filter (left). The influence of a back reflector of bleached cellulose which should also increase the edge emission will be discussed, too.
The reflective layer is located between two glass substrates with a thickness of about $d = 1$ mm each and has the lateral size of the fluco, but the active area of the filter is a little smaller than the glass, so that the filter is nearly transparent near the edges.
Results of the measurement of the edge emission are plotted in Fig. F.2. The impact of the filter with or without back reflector on the overall edge emission in comparison with the edge emission of the bare fluco for both flucos used in this work (Rhodamin 6 G and Lumogen F rot 305) with an indication of the transmission of the excitation (505 nm LED) through the filter is shown.
Due to a transmission of only $(73.3 \pm 0.1)\%$ for the excitation (see Fig. F.3) through the filter, the edge emission from the fluco with the filter on top and the filter on the fluco with spacers in between is reduced. When the filter is located directly on top of the fluco, the edge emission is reduced more strongly than can be expected by the filter transmission of 73.3%. The reason may result from the filter design: The glass substrate of the filter has a refractive index of approximatly $n = 1.5$ which equals that of the fluco, thus radiation from the fluco can easily propagate into the filter glass substrate and escape on the edge of the filter. Thus the glass substrate of the filter destroys the light trapping of the fluco which can be prevented by using reflective spacers (e. g. teflon) between the fluco and the filter.
The rest of the results show the influence of the back reflector on the edge emission of the fluco with and without filter. A back reflector influences various properties, because the excitation which is transmitted through the fluco is scattered back so that more radiation is absorbed and the emitted radiation inside the escape cone leaving the fluco is also scattered back into the fluco,

so more radiation is transported to the edge of the fluco. Fig. F.4 shows the spatial and diffuse reflection (left) and the scattered photon flux of a 632.8 nm laser (right). Most of the radiation is reflected or scattered back.
Thus the edge emission of the Rhodamin 6 G fluco is more enhanced by the back reflector, because this fluco has a lower absorption and thus more radiation hits the back reflector and is reflected back. So the absorption is more enhanced for this fluco.
Additionally the edge emission with a filter on top of a fluco is stronger with a back reflector than without, because the radiation emitted by the dye inside the escape cone is not only reflected back to leave the fluco on the opposite side but is trapped inside the fluco. Thus a filter on top of the fluco with a back reflector can enhance the edge emission even if the transmission for the fluco excitation is not 100%.

The influence of a low-pass filter on the angular dependent edge emission of a fluco is a little more confusing and the results, apart from those in Fig. F.6, will be presented in appendix E. Fig. F.6 shows the ratio of the photon flux emitted on the edge of the fluco with low-pass filter on top ($\Gamma_{\text{with}}(\alpha, \lambda)$) to the photon flux without filter ($\Gamma(\alpha, \lambda)$)

$$\chi(\alpha, \lambda) = \frac{\Gamma_{\text{with}}(\alpha, \lambda)}{\Gamma(\alpha, \lambda)} \tag{F.1}$$

for the fluco with Rhodamin 6 G in PMMA on glass. This angular dependent and spectrally resolved influence of the filter on the edge emission clearly shows a reduction of the emission for all angles when the filter is on top of the fluco (due to low transmission for the excitation and additional losses as described before), but it can be seen that the emission for small angles is reduced less strongly than for larger angles.
This behavior agrees well with the results from Goldschmidt [41] for the influence of a filter on the edge emission of a fluco for different excitation positions on top of the fluco, where the emission is enhanced more strongly when the fluco is excited further away from the edge, because a low angle corresponds to an excitation position far away from the edge of the fluco as described in the theory.

A ray-tracing simulation with TracePro [93] was performed to characterize the theoretical influence of a filter and different reflectors on the edge emission of a fluco. Fig. F.5 (left) shows an illustration of the contents of the simulation: A fluco with Rhodamin 6 G in PMMA on top of a glass substrate with 2.5 mm edge length and a thickness of $d = 1$ mm is illuminated with a homogeneous $\lambda = 500$ nm source from the top through an edge filter. Mirrors are positioned on three edges of the fluco and on its back to reflect the emitted radiation back. Between the fluco and the mirrors and filter a small distance is kept, so that the light trapping of the fluco is not influenced by the filter and the mirrors.
The influence of the mirror on the back (back), of mirrors on the other fluco edges (edge), of all mirrors (allm), of the filter on top of the fluco (filter), the filter on top of the fluco and a back reflector (bm+f) and all components together (all) are plotted in Fig. F.5 for a low (center) and a high dye concentration (right). These results confirm, that placing a photonic crystal on top

of a fluco is not simple, because there are many other parameters which must be considered.

The idea of placing a photonic crystal on top of a fluco is to reduce the reemission of the dyes through the escape cone and thus to enhance the edge emission. Thus the experimental results and the simulations from above where designed to characterize the influence of a low-pass filter with 550 nm edge wavelength on the edge emission.
But these results show an influence of the filter on the edge emission which is not sufficient to yield the influence on the efficiency of the fluco. This has several reasons:

- The transmission for the excitation wavelengths of the filter is too low, because the enhancement of the edge emission cannot compensate the reduction of the excitation. Here a better but more expensive filter should be used.
- An enhancement of the edge emission is dependent on the dye concentration: A high dye concentration reduces the photon flux of the excitation which hits a scatterer on the back of the fluco and also enhances the reabsorption. Thus the influence of a back reflector and also of a photonic structure on top of the fluco should be characterized using different dye concentrations.
- The design of the filter-fluco-reflector system should be discussed in more detail: Here spacers between fluco and filter yield the best enhancement of the edge emission, but a different design can maybe enhance the edge emission even more strongly.

But at least the results from above confirm, that an enhancement of the edge emission by placing a photonic crystal on top of the fluco is possible.

Figure F.1.: Position of the filter for the different setups: Emission of the fluco without filter (left), with a filter on top of the fluco (center) and with the filter on the fluco with spacers in between (right).

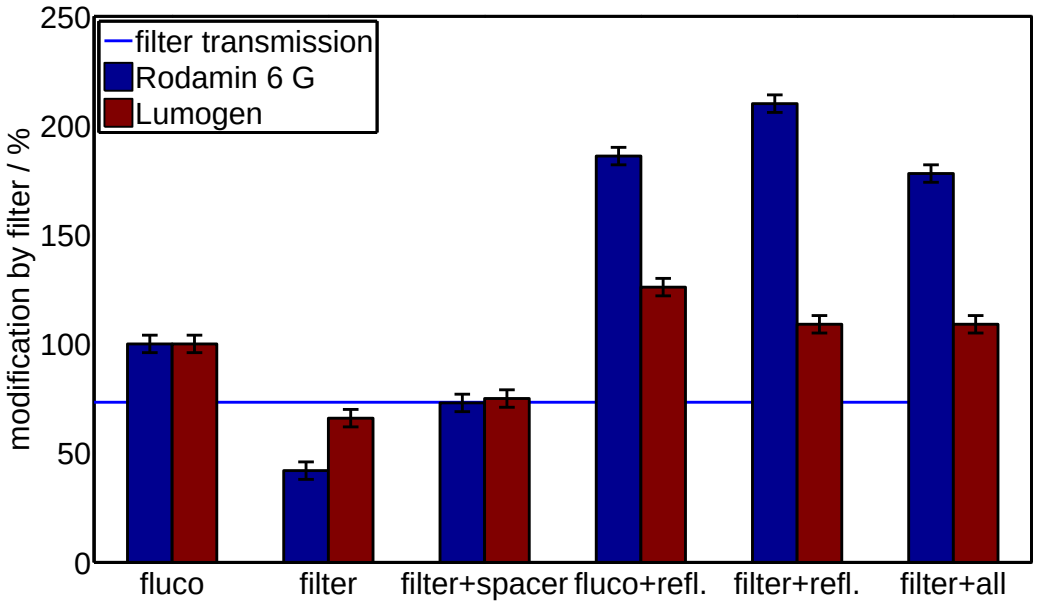

Figure F.2.: Influence of a back reflector and a filter on top of the fluco or on top of spacers on the edge emission for a fluco with Rhodamin 6 G on top of a glass substrate and Lumogen F rot 305 in PMMA.

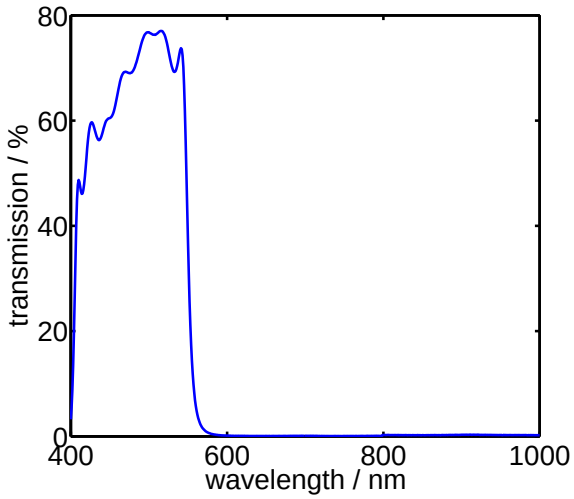

Figure F.3.: Transmission through the 550 nm low-pass filter.

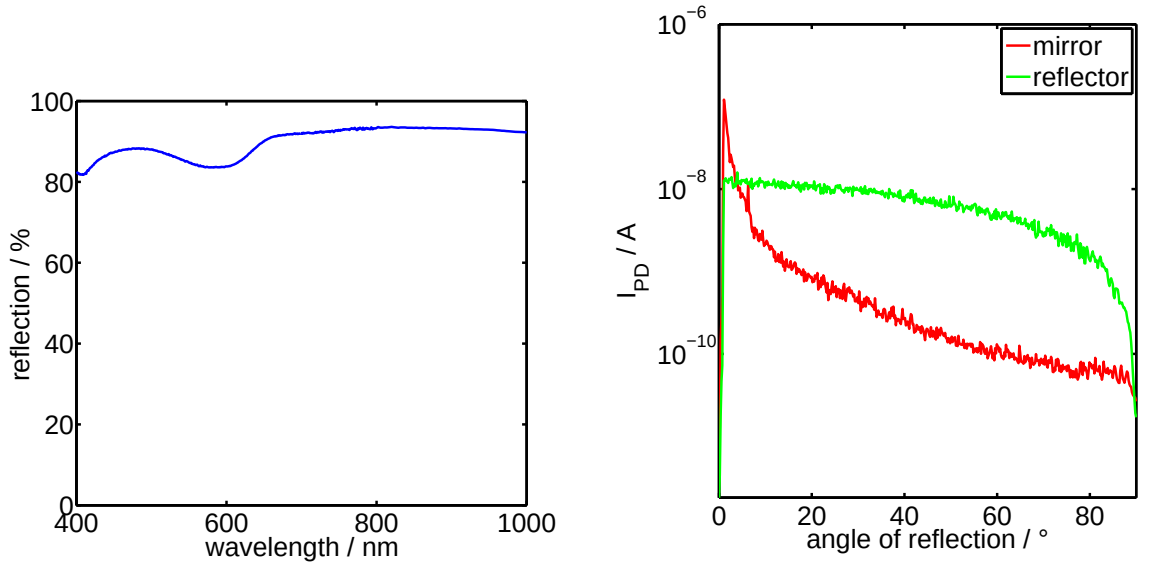

Figure F.4.: Diffuse reflection of the back reflector based on bleached cellulose (left) and angular dependent scattering of a 632.8 nm laser on the back reflector in comparison to the reflection on a mirror (right).

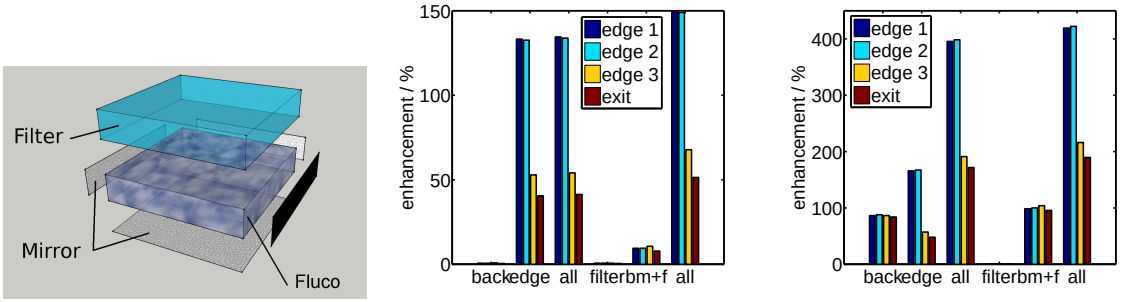

Figure F.5.: Simulation of the influence of a filter and mirrors on the edge emission of a fluco. Simulation model (left) with fluco, low-pass filter on top and mirrors on three sides of the fluco and on its back, impact on the edge emission for low (center) and high (right) dye concentration.

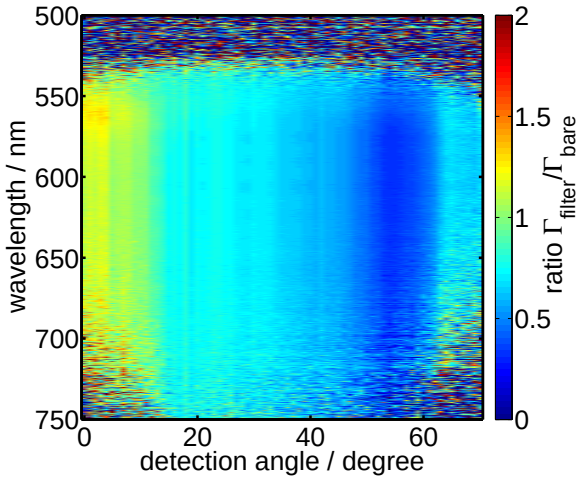

Figure F.6.: Influence of the 550 nm low-pass filter on the angular dependent edge emission for homogeneous excitation of the fluco with Rhodamin 6 G in PMMA on glass.

G. Acknowledgements

First of all, I would like to thank my supervisor Prof. Dr. G.H. Bauer, who often helped me with guiding and supporting discussions, new ideas and sometimes special solutions for problems. This work would not have been possible without his support.
I would like to thank Prof. Dr. T. Markvart (University of Southampton) for the introduction into fluorescence solar collectors. He gave me an overview over the thermodynamics and the theory of flucos and his group introduced me into the experimental characterisation of flucos.
I especially thank Peter Pargmann for his technical support. He often helped me to overcome problems in the short term.
I would also like to thank the other members and some former members of the group GRECO at the Carl von Ossietzky Universität Oldenburg, who helped me with experimental setups, technical problems or with the theoretical background. I especially thank Florian Heidemann, Hendrik Sträter, Levent Gütay, Max Meesen, Oliver Neumann, Rudi Brüggemann, Sebastian Wilken and Sven Burdorf.
I would like to thank Johannes Üpping (Martin-Luther-Universität Halle-Wittenberg), Lorenz Steidl (Johannes Gutenberg-Universität Mainz) and Nazila Soleimani (University of Southampton) for the preparation of the opal and fluco samples and their help with the understanding of their work.
Last but not least, I would like to express my deepest thanks to my parents and to Friederike for their unfailing support, encouragement and love and for giving me the opportunity for working on this thesis.

H. Curriculum vitae

Personal data:
Sebastian Knabe
Birth: 06.06.1983 in Oldenburg (Oldb)
Nationality: German

Alternative civilian service:
Since 6/2003 member of the auxiliary fire brigade Friedrichsfehn

Education:

1990-1994	Grundschule Bad Zwischenahn
1994-1996	Orientierungsstufe Bad Zwischenahn
1996-2003	Gymnasium Bad Zwischenahn-Edewecht
2003	Abitur
2003-2008	Carl von Ossietzky Universität Oldenburg:
	Subject: Physics/Diploma
	Diploma Thesis “Lumineszenz nach dem verallgemeinerten
	Planckschen Gesetz für neuartige Strahlungseinkopplung”
since 9/2008	Research assistant at Carl von Ossietzky University Oldenburg
	in the group of Prof. G. H. Bauer with the intention of graduation.

I. Erklärung

Hiermit versichere ich, dass ich diese Arbeit selbständig verfasst und keine anderen als die angegebenen Hilfsmittel benutzt habe.

Sebastian Knabe